# INNOVATIONS IN VASCULAR ULTRASOUND

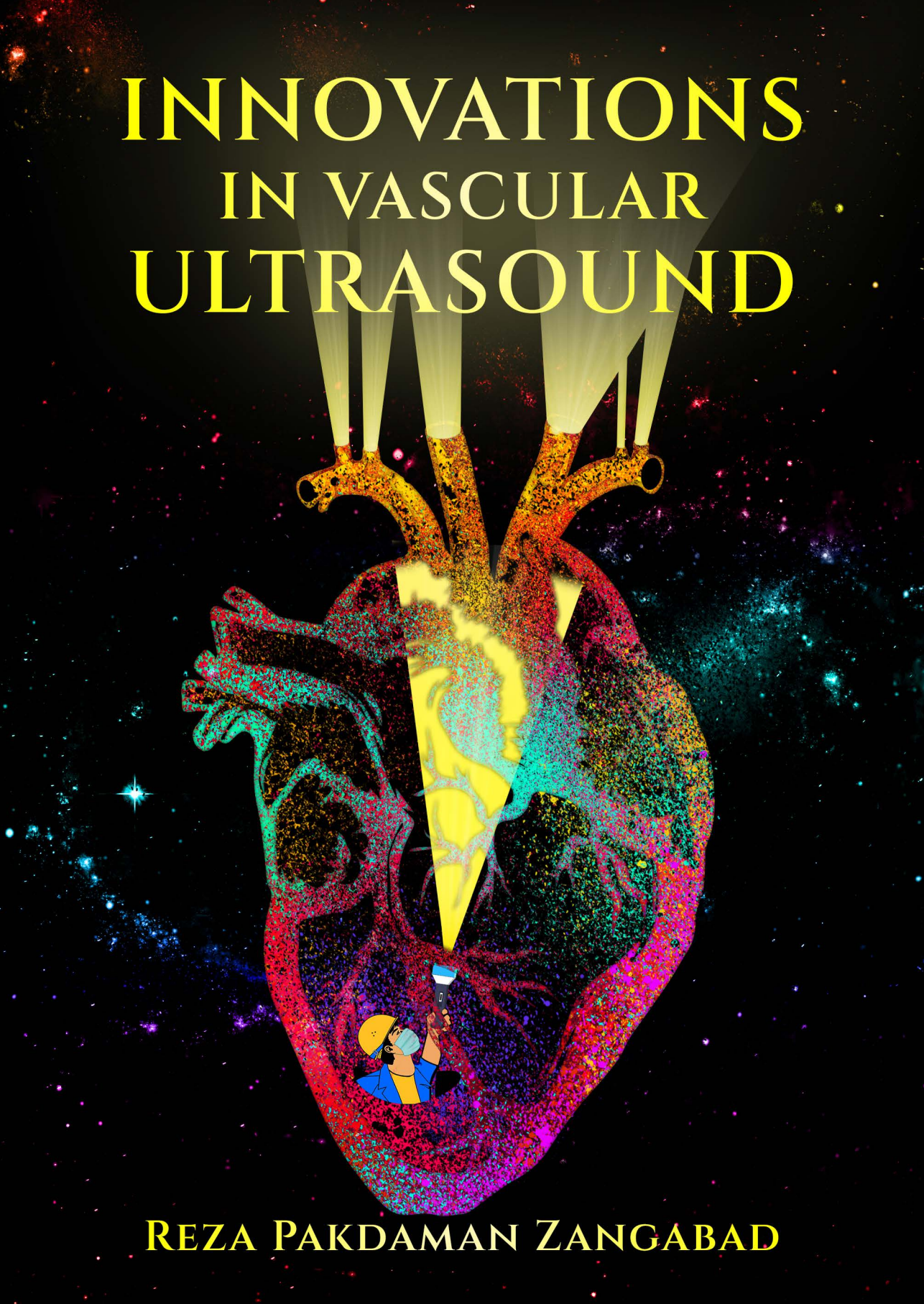

REZA PAKDAMAN ZANGABAD

# Innovations in Vascular Ultrasound

Innovaties in Vasculaire Echografie

**Reza Pakdaman Zangabad**

*ISBN/EAN:* 978-94-6421-458-1

*Printed by:* IPSKAMP Printing

*Front & Back:* Reza Pakdaman Zangabad



For a printed version please contact:

Secretary Biomedical Engineering (room Ee 2302)
Erasmus MC University Medical Center Rotterdam
P.O. Box 2040
3000 CA Rotterdam
the Netherlands

An electronic version of this dissertation is available at
https://thesis.eur.nl/

# Innovations in Vascular Ultrasound

Innovaties in Vasculaire Echografie

## Thesis

to obtain the degree of Doctor from the
Erasmus University Rotterdam
by command of the
rector magnificus

prof. dr. F. A. van der Duijn Schouten

and in accordance with the decision of the Doctorate Board.
The public defense shall be held on
Thursday 23rd September 2021 at 15:30

by

**Reza Pakdaman Zangabad**

born in Tabriz, Iran.

**Erasmus University Rotterdam**

| | |
|---|---|
| **Promotors:** | Prof. dr. ir. A.F.W. van der Steen<br>Prof. dr. G. van Soest |
| **Other members:** | Prof. dr. F. L. Değertekin<br>Dr. H. J. Vos<br>Dr. N. Bhattacharya |

Financial support by the Lumibird (new name of Quantel-Keopsys) for the publication of this thesis is gratefully acknowledged.

Financial support by the Dutch Heart Foundation for the publication of this thesis is gratefully acknowledged.

This work was performed in the framework of the Medical Delta program NIMIT. Medical Delta is gratefully acknowledged for financial support for the printing costs of this thesis.

Additional financial support for the printing of this thesis was kindly provided by Erasmus University Rotterdam.

*In memory of my Grandfather Mokhtar Pakdaman Zangabad,*
*who taught me the power of the mind is beyond everything,*
*and my Grandmother Shahr-e-Banu Zareian for her endless love and*
*support throughout my life.*

# Contents

# Summary

Pushing the ultrasound technology for better diagnosis, image resolution and cost reduction is the core of this work. In this thesis, we explored several innovative solutions for ultrasound imaging. We devised techniques and developed ultrasound systems to address the challenges that are associated with vascular ultrasound which can be subsumed into two main categories: **a.)** novel transducer architecture and **b.)** novel imaging techniques.

The first approach consists of ultrasound system engineering for the realization of the first multi-element Capacitive Micromachined Ultrasound Transducer (CMUT) phased array for side-looking Intravascular Ultrasound (IVUS) imaging. The second approach involves a system development for photoacoustic (PA) imaging in which a specific dual-frequency probe is designed and a novel quantitative ultrasound approach for photoacoustic flow velocimetry imaging is devised.

An introduction to IVUS, PA imaging, and probe designing is provided in chapter 1. The technology of ultrasound imaging is described and the clinical demands for improving the current technologies are provided.

In chapter 2 the cross-coupling of transducer elements through the medium and its effect on the frequency response of the CMUT array was discussed. Finite Element Analysis (FEA) was carried out using the radiation impedance method for analyzing this effect on the CMUT array which has wrapped around a catheter tip with a cylindrical configuration. The cross-talk between planar CMUT elements was linked with dips in the frequency spectrum from experimental data and was shown that the element cross-talks don't have detrimental effects on the array bandwidth.

In chapter 3 the first 96 elements CMUT phased array placed at the circumference of a catheter tip with 1.2 mm diameter for the side-looking IVUS imaging was described. A system for utilizing Coded Excitation (CE) to improve the penetration depth and image signal-to-noise ratio (SNR) was developed. First, the CMUT array was characterized showing that the -6dB device bandwidth at 30 V DC biasing is 25 MHz with 20 MHz center frequency and has transmitted sensitivity of 37 kPa/V at that frequency. A real-time system and software tools in MATLAB were developed for signal acquisitions and processing, beamforming, image optimization, and data analysis for B-mode IVUS.

A linear Frequency Modulation (FM) coded waveform was designed based on the CMUT array characteristics and a wire phantom and a human coronary artery plaque were imaged. By assessing the image quality of the reconstructed wire phantom image, 60 $\mu$m and 70 $\mu$m axial resolution were achieved using the short pulse and coded signal, respectively. Furthermore, an 8 dB gain in the SNR using the FM signal was achieved.

PA signals can have a very large bandwidth and large dynamic range. In chapter 4 a broadband PA receiver was introduced which was incorporated in chapter 5 ffor the realization of a dual-frequency probe for PA imaging of the human carotid arteries.

First, it was demonstrated that with an appropriate electrical impedance matching, off-resonance Polyvinylidene Difluoride (PVDF) transducers offer the bandwidth and sensitivity to fully capture the PA signals. Using the FEA in COMSOL and validating it with the experiment, it was shown that the elements crosstalk in a 28 $\mu$m thick, kerfless PVDF arrays, where the electrodes were patterned onto the piezoelectric material, were negligible. Second, by utilizing this approach in chapter 5, a dual-frequency probe was proposed using a dual-layer piezoelectric material consisting of lead zirconium titanate (PZT) for ultrasound stack and a kerfless PVDF array for PA signal reception, which was placed on top of the PZT stack.

It has been discussed that the loading effect of the PVDF array narrows the ultrasound bandwidth; however, the loading effect was minimized by considering the PVDF array as the second matching layer of the ultrasound stack. Using 3D FEA, a design with and without subdicing was modeled, and the results showed that the -3dB bandwidth of the ultrasound stacks were 87% and 75% relative to the center frequencies. A transmit sensitivity of 17 kPa/V and 21 kPa/V were found for those two realizations, respectively.

In chapter 6 a photoacoustic imaging system using a fast pulsed laser diode and a novel quantitative ultrasound method based on normalized first-order field autocorrelation function was developed to estimate flow velocities. It was demonstrated how the decorrelation time of signals acquired over frames are related to the flow speed and was shown that the PA flow analysis based on this approach is an angle independent flow velocity imaging method. We baptized this method vPA: Photoacoustic flow velocimetry imaging. Directional velocimetry imaging up to 20 mm/s in a phantom study was demonstrated, and vPA was applied to imaging flow speed in the microvasculature of the chorioallantoic membrane (CAM) of a 6-day old chicken embryo where pulsatile flow in the arterial layer of the CAM was shown. This chapter also showed that vPA has the potential to simultaneously image the blood flow speed and extract the functional information like oxygen saturation of the blood.

In chapter 7 the achievements were summarized and the limitations of our studies were discussed with some recommendations for future work.

# Samenvatting

Maximaal gebruik van ultrageluid technologie voor beter diagnose, beeld resolutie en kosten reductie is de kern van dit werk. In dit proefschrift zijn een aantal innovatieve oplossingen onderzocht voor ultrasone beeldvorming. Er zijn technieken bedacht en ultrageluid systemen ontwikkelt om de uitdagingen van vasculair ultrageluid aan te pakken. Deze kunnen worden ondergebracht in twee categorien: a.) nieuwe transducer architectuur en b.) nieuwe beeldvormende technieken.

De eerste categorie bestaat uit een ultrageluid systeemontwerp voor de eerste zijwaarts kijkende IVUS catheter die is opgebouwd uit een zogenaamde multi element “Capacitive Micromachined Ultrasound Transducer” (CMUT) in phased array configuratie. De tweede categorie bestaat uit de ontwikkeling van een foto-akoestisch (PA) systeem waarvoor een specifieke “dual frequency probe” is ontworpen en een nieuwe kwantitatieve ultrageluid benadering voor foto-akoestische stromingssnelheid beeldvorming is bedacht. Een introductie in IVUS, foto-akoestische beeldvorming en ultrageluid probe ontwerp wordt behandeld in hoofdstuk 1. De technieken achter ultrasone beeldvorming worden beschreven evenals de klinische eisen die aan deze vernieuwende technologie gesteld worden.

In hoofdstuk 2 wordt de koppeling van transducer elementen door het medium en het effect daarvan op de frequentie response van het CMUT array behandeld. Het CMUT array is cylindrisch om de cathetertip gewikkelt. Met behulp van eindige elementen analyse (FEA) is de koppeling bestudeerd en daarbij is gebruik gemaakt van de “Radiation Impedance” methode. De overspraak tussen vlakke CMUT elementen is daarbij gekoppelt aan de dips in het frequentie spectrum verkregen uit experimentele data. Hierbij werd aangetoond dat de overspraak geen nadelige gevolgen heeft op de bandbreedte van het array.

In hoofdstuk 3 wordt het eerste 96-elements CMUT phased array gemonteerd rond de omtrek van een 1,2mm diameter catheter voor een zijwaarts kijkende IVUS systeem beschreven. Voor deze toepassing werd een systeem ontwikkelt dat gebruik maakt van “Coded Excitation” (CE) om op die manier penetratie diepte en signaal/ruis verhouding (SNR) te verbeteren. Allereerst werd het CMUT array gekarakteriseerd en aangetoond dat de -6dB bandbreedte bij 30V DC bias spanning 25MHz bedraagt met een centerfrequentie van 20MHz en een zend gevoeligheid van 37kPa/V bij deze frequentie. Een real-time systeem met bijbehorende software applicatie in MATLAB is ontwikkelt voor de signaal aquisitie en verwerking, beamforming, beeld optimalisatie en data analyse van de B-mode IVUS.

Een liniair frequentie gemoduleerd (FM) coderings signaal werd ontworpen gebaseerd op de CMUT array eigenschappen en zowel een draad fantoom als een humane coronaire arterie plaque zijn hiermee bekeken. Door de beeldkwaliteit te beoordelen van het gereconstrueerde draad fantoom is een axiale resolutie gehaald

van 60 $\mu$m en 70 $\mu$m voor respectievelijk korte puls en gecodeerd signaal en een 8dB winst in de signaal/ruisverhuiding voor het FM signaal.

PA signalen kunnen een zeer grote bandbreedte en groot dynamisch bereik hebben. In hoofdstuk 4 wordt een breedbandige PA ontvanger geintroduceert die is opgenomen in hoofdstuk 5 voor de realisatie van een “dual frequency probe” voor PA beeldvorming van humane carotide arterien.

Allereerst is er aangetoont dat met de juiste impedantie aanpassing uit resonantie PolyVinylidene DiFluoride (PVDF) transducenten een bandbreedte en gevoeligheid bieden om het volledige PA signaal te kunnen invangen. Gebruik makend van de FEA in COMSOL en het valideren daarvan door middel van experimenten is aangetoond dat de element overspraak in een 28µm dik, kerfloos PVDF array met een elektroden patroon op het piezo materiaal, verwaarloosbaar is. Ten tweede, door gebruik te maken van deze benadering in hoofdstuk 5, is er een “dual frequency” probe voorgesteld bestaande uit piëzoelektrisch materiaal in twee lagen waarbij een laag bestaat uit lood zirkonium titanaat (PZT) voor de ultrageluid transducent met daar bovenop een laag met een kerfloze PVDF transducent voor het PA signaal ontvangst. Er is besproken welke belasting deze PVDF laag vormt voor de bandbreedte van de ultrageluid transducent; echter het effect hiervan kon gereduceerd worden door deze laag als tweede aanpassingslaag voor de transducent te gebruiken. Door middel van 3D FEA zijn zowel ondergedeelde als niet gedeelde transducenten gemodelleerd en de resultaten laten zien dat de relatieve -3dB bandbreedte van de ultrageluid transducer respectivelijk 87% en 75% van de centerfrequentie bedragen. De zendgevoeligheid van de twee configuraties waren respectievelijk 17 kPa/V en 21 kPa/V.

In hoofdstuk 6 is een fotoacoustisch beeldvormend systeem ontwikkelt dat gebruik maakt van een snelle gepulste laser diode en een nieuwe kwantitatieve ultrageluid methode die gebaseerd is op een eerste orde veld autocorrelatie funktie voor stromingssnelheidsbepaling.

Hierbij werd er gedemonstreerd hoe de decorrelatietijd van de verkregen signalen over de frames gerelateerd zijn aan de stromingssnelheid en werd aangetoond dat de PA stromingssnelheidanalyse gebaseerd op deze benadering hoek onafhankelijk is. We hebben deze methode vPA gedoopt: Fototakoestische stromingssnelheid beeldvorming (Photoacoustic flow velocimetry imaging).

Directionele snelheidsmeting-beeldvorming tot 20mm/s werd aangetoond in een fantoom studie en vPA werd toegepast in stromingssnelheid beeldvorming van de micro vascularisatie in het chorioallantoïsche membraan (CAM) van een 6-daagse kippenembryo waar de pulsatiele stroom van de arteriële laag van de CAM werd aangetoond.

Dit hoofdstuk laat tevens zien dat vPA de potentie heeft om gelijktijdig de bloedstromingssnelheid en functionele informatie zoals zuurstof saturatie zichtbaar te maken.

In hoofdstuk 7 zijn de resultaten samengevat en de beperkingen van onze studies bediscussiëerd met enige aanbevelingen voor de toekomst.

# 1

# Introduction

1

## 1.1. Motivation

Discovery of the piezoelectric effect by Pierre and Jacques Curie in 1880 paved the way for current ultrasound imaging [1]. The use of piezoelectric effect in cardiovascular imaging started from M-mode tracings [2–4] which then led to development of the first real-time 2D echocardiography by Bom in the 1971 at Rotterdam [5]. Conventional ultrasound probes use piezoelectric material to generate ultrasound waves. Applying a short electrical pulse to the piezoelectric electrodes induces vibrations and produces ultrasound waves. These waves propagate and reflect back from the heterogeneities of the medium which then are converted to electrical signals by the same probe. The spatial location of the heterogeneities can be determined by time-of-flight and their acoustic/mechanical properties, using these echo delays the received electrical signals are converted back to form an ultrasound image.

The quality of the image and resolution depends on the frequency of the ultrasound waves and the bandwidth of the transducer, which dictate the axial resolution. The beamforming methods and element pitch stipulate the lateral resolution. Depending on the properties of the medium, the ultrasound waves are attenuated. The higher the frequency is, the higher the attenuation becomes [6, 7]. Thus, ultrasound waves of certain frequency can penetrate to a certain depth. Consequently, for imaging different part of body designated probes are manufactured to address the requirement. In TransThoracic Echocardiography (TTE) imaging, ultrasound waves pass in between the ribs and the lungs to reach the heart. Thus, a probe with relatively low operating frequencies (1 - 5 MHz) is preferred. For carotid artery imaging, an ultrasound probe with higher frequency (7.5 -10 MHz) is preferred since the location of the carotid artery is relatively closer to the transducer and smaller details must be resolved in comparison with the TTE application. Further development to very high frequencies and miniaturization of transducer array led to introduction of catheter based ultrasound imaging [8, 9]. Piezoelectric materials are usually band limited with 60-80% fractional bandwidth. In order to increase the axial resolution, new transducer technologies with higher fractional bandwidth are required.

Photoacoustic (PA) imaging (PAI) is an emerging imaging modality that combines the optical illumination and ultrasound sensing[10, 11]. The PA effects is induced by nano-second laser pulses illuminating absorbing targets or tissues. Particles like red blood cells or hemoglobins absorb the light which causes local heating and thermoelastic expansion and vibrations. These vibrations generate pressure waves which can be detected by an ultrasound probe [12, 13]. Photoacoustic image reconstruction is based on propagation delays between the light pulse and pressure sensed by each elements of an ultrasound probe. To be able to induce the PA effect, the stress and thermal confinements need to be held. In stress confinement, the laser pulse duration needs to be smaller than the acoustic transit time across the absorbing volume and in thermal confinement, the laser pulse duration needs to be shorter than the thermal diffusivity of the volume [14, 15]. Light cannot penetrate into the deep tissues due to the scattering; thus, a pure optical imaging could only provide high resolution optical contrast images of biological tissues at a shallower distances while ultrasound pulses can image deeper structures in a tissue. PAI

combines these two features and provides high contrast high resolution images of tissues up to centimeters depths which has various clinical imaging application. Real-time monitoring and assessment of RF ablation lesion formation in left atrium [16, 17], real-time volumetric intravascular photoacoustic imaging of atherosclerotic plaques [18, 19], monitoring tumor angiogenesis and PAI of blood vasculature [20], functional mouse brain imaging and monitoring blood-oxygenation dynamics [21] and PA blood flow imaging are some of the PAI applications [22, 23]. In order to increase the sensitivity of PA images, it is crucial to acquire the generated ultra broadband PA signals by an ultra broadband ultrasound array.

The general goal of this thesis is to develop innovative techniques and low cost devices for vasculature imaging and help clinicians in diagnosing patients with cardiovascular diseases.

## 1.2. Novel Transducer Technologies and Design Approaches

Ultrasonic transducer technology is dominated by piezoelectric technology. Capacitive Micromachined Ultrasonic Transducer (CMUT) is a relatively new in the field of ultrasonic transducers [24, 25]. CMUTs are fabricated on silicon wafers using the well established micromachining techniques which has been developed and used in Integrated Circuit (IC) industries [26–30]. Generally CMUTs can be simplified as parallel plate capacitors. CMUTs have three main components: cavity, membrane, and electrodes. In a silicon substrate the cavity is formed and a thin layer suspended over the cavity acts as a membrane. An embedded metal layer in the membrane serves as top electrode and the silicon substrate acts as bottom electrode. Figure 1.1 depicts the schematic view of CMUT structure.

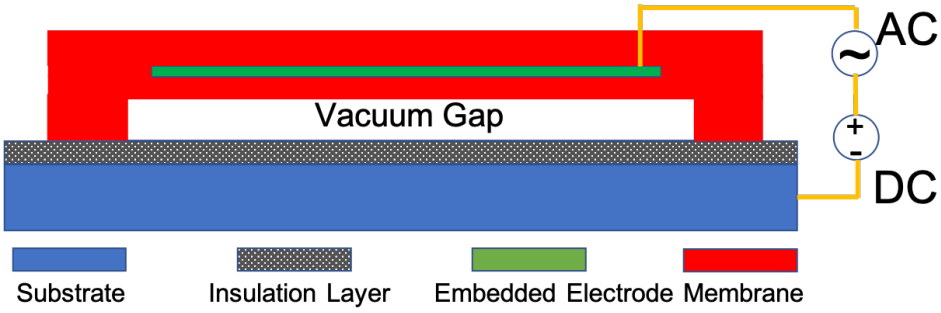


Figure 1.1: Schematic view of the CMUT structure

Applying a DC biasing voltage to the electrodes charges the CMUTs and generates an electrostatic force which pulls the top membrane toward the substrate. Driving the biased CMUTs with an AC signal introduces an oscillation in the electrostatic force, making the membrane to vibrate and generate ultrasound pressure waves which transmit to the surrounding medium. In the receive mode, the incident

ultrasound waves on the CMUTs modulate the gap with the same frequency of the incoming pressure waves. The induced modulation changes the capacitance which is converted to a voltage level.

The acoustic impedance of the CMUTs is very low in comparison with the acoustic impedance of the water or tissue. This makes CMUTs to be inherently matched with the medium and results in very high coupling efficiency of nearly 100 % over frequencies in transmitting and receiving the ultrasound waves. Consequently, CMUT offers more bandwidth [31]. Ease of fabrication, capability to directly build CMUTs on top of ICs, miniaturization for minimally invasive applications and a high yield with low end product cost are the other advantages of this novel transducer technology [32–34].

Depending on the amplitude of the DC voltage, CMUTs either work in the collapse mode or in the conventional mode (uncollapsed) with different acoustical behaviour. Collapse mode CMUTs provide higher transmit and receive sensitivity with higher bandwidth in comparison with conventional mode [35]. These features were exploited to make ultrasound images at low and high frequencies for having different penetration depth and resolution in intracardiac echocardiography imaging [36, 37].

Recently, a hand-held ultrasound probe based on monolithic integration of CMUT on chip has been introduced by the Butterfly Network capable of imaging (M-mode, B-mode, color doppler, power doppler ) all body with single probe (figure 1.2a) which is considered as a revolution in ultrasound imaging with less than 2000 $ end product cost.

Intravascular ultrasound (IVUS) imaging is another field where CMUTs have potential to be utilized [38, 39]. Advances in micromachining techniques allowed the fabrication of CMUTs on a flexible substrate where CMUTs array could be wrapped around a cylinder for intraluminal application [40].

Photoacoustic imaging (PAI) is an emerging imaging modality providing images with optical contrast at the acoustic penetration depth. PA and ultrasound imaging are complementary which can share the same hardware (Transducer, data acquisition) for multi-modal imaging. Piezoelectric based ultrasonic transducers are not transparent, thus, the laser path to the imaging target is different from the pulse-echo path. Transparent CMUT array is going to find its spot to address the requirement [41, 42]. Due to the high broad band nature of PA signals, CMUTs are good candidate to increase the PA image quality and resolution.

Lead zirconate titanate (PZT) based ultrasound arrays offer high transmit and receive efficiency; however, the limited bandwidth of these transducers provide low sensitivity over the broad band PA signals. In order to overcome the low bandwidth shortcoming of piezoelectrics in simultaneous imaging with different imaging modalities, multiple acoustical stacks using piezoelectric were implemented for contrast enhanced IVUS [43], transrectal acoustic angiography [44], and doppler imaging [45].

An off-resonance PolyVinylidene DiFluoride (PVDF) with integrated amplifier of-

(a) (b)

Figure 1.2: **(a)** Butterfly Network CMUTs on chip handheld probe for imaging whole body, **(b)** The CMUT array wrapped around a catheter tip. Image **(a)** has been reproduced from www.butterflynetwork.com , and image **(b)** is a courtesy of Philips research Eindhoven.

fers relatively greater receive efficiency than PZT which potentially could increase the sensitivity of the PA image [46].

## 1.3. Intravascular Ultrasound Imaging

The technology used in medical ultrasound is continuously evolving and currently contributing to important improvements in patient diagnosis and treatment. Diseases of the heart and circulatory system (cardiovascular disease or CVD) are the main causes of death in Europe, accounting for 1.8 million deaths and more than 11 million hospitalisations each year in the EU[47]. More than a third (36%) of all deaths are from CVD. With an ageing population, the prevalence of many cardiovascular diseases increases strongly. The resulting economic, as well as human costs are tremendous. Overall, CVD is estimated to cost the EU economy almost 210 billion euros a year, due to healthcare costs and lost productivity. Decreasing the associated health care cost and providing an affordable treatment to the patients with CVD is one of the main challenges and is strongly dependant on advancement in technology.

One of the main causes of CVD is called atherosclerosis. It occurs when fat, cholesterol and necrosis cells are built up inside the arteries' wall leading to the thickening and stiffening of the blood vessels so called plaques [48]. Atherosclerosis could restrict or completely block the blood flow to organs. Sudden interruption

of the blood flow to the heart muscles caused by intra-coronary thrombosis is called a heart attack. Percutaneous Coronary Intervention (PCI) is commonly performed treatment for these patients which involves either stent placement or using balloon to improve blood flow.

IVUS provides images of the vessel wall and atherosclerotic plaque from inside of the coronary vessels [49–51] using either a single rotating element or an array of PZT elements placed at the tip of a catheter with maximum diameter of 1.2 mm, with operating frequencies between 20 - 60 MHz. This technique helps cardiologists to assess the degree of stenosis and exact location of the plaques for deciding on the length of the stent and landing zone.

By today, the IVUS market is dominated by three players; Philips-Volcano who has developed Eagle Eye (phased array) and Revolution (rotating) and Boston Scientific with iCross and OptiCross (rotating). ACIST kodama catheter is relatively new in the market which operates at 60 MHz frequency range and offers better resolution ($\leq 40\mu m$). It has a dual frequency option working in 40 MHz or 60 MHz to balance between tissue penetration and high resolution requirement. Recently, Infraredx has released a dual-modality intravascular catheter that combines IVUS with near infrared spectroscopy (NIPRO OKAY and Makoto imaging system). All products are equipped with piezoelectric transducer elements and are built in a catheter with a typical size of 1 -1.2 mm in diameter. Since PZT is the core transducer component, the IVUS images resolution could be improved by utilizing the CMUTs.

## 1.4. Coded Excitation in Ultrasound Imaging

Current ultrasound imaging systems use a short pulse (high bandwidth) in order to exploit the transducer frequency response to attain the maximum achievable image resolution. However, due to the frequency dependant sound wave attenuation in tissues, the returned echos from deep tissues are weak and below the minimum detectable pressure of the system dictated by the Signal-to Noise Ratio (SNR) of the whole system. Increasing the pulse amplitude to provide more transmitted acoustic energy is hampered by the capability of electronics and also maximum biological exposure to acoustic intensity.

Coded Excitation (CE) is an alternative way to address the issue which was adopted from radar techniques [52]. CE allows the transmission of longer pulse which improves the SNR thus, increases the penetration depth of the ultrasound waves while retaining the imaging resolution [53–58]. Among the different coded signals, linear Frequency Modulation (FM) captured more attention in ultrasound imaging since it is more robust in the presence of noise requiring less filtering [59]. The improvement in SNR depends on the duration of coded signal (T) and the system bandwidth (BW). Since the ultrasound system bandwidth is qualified by the ultrasound transducers, increasing the excitation duration seems the only way to gain in SNR. However, for application like IVUS, transmitting long code is not favourable as it increases the deaf time; thus, the closer tissues toward the array will not be imaged. Utilizing a broad band transducer like CMUTs could potentially increase the SNR.

## 1.5. Photoacoustic Vascular flow imaging

Photoacoustic (or optoacoustic) imaging, is a hybrid imaging modality that combines optical illumination and ultrasound imaging. By illuminating the targets using a short laser pulse, the photons are absorbed and then are converted into heat, resulting in a transient local temperature rise which induces a thermo-elastic expansion. The local expansion generates pressure waves which propagate through the sample and can be recorded by an ultrasound transducer array. The generation of the PA pressure waves requires that the laser pulse width should be shorter than the acoustic transit time across the absorbing volume (stress confinement) and thermal diffusion time in that region (thermal confinement) [17, 60–63].

Different absorbers such as endogenous chromophores (e.g., oxygenated and deoxygenated hemoglobin), or exogenous contrast agents (e.g., nanoparticles) [64–66] have different light absorption efficiencies. Since each of these chromophores exhibits its own characteristic absorption spectra; consequently, the generated PA pressure waves provide valuable information on the optical properties of the sample. Moreover, the ultrasound waves scatter much less than light [67, 68], resulting in a longer pressure waves propagation with less attenuation.

Depending on the illumination and ultrasound recording methods, photoacoustic imaging are categorized in two main area of photoacoustic tomography (PAT) and photoacoustic microscopy (PAM). PAT systems use wide-field illumination and the generated pressure waves are recorded using either a single element or transducer array [69–72]. PAM systems provide high resolution imaging. If the illuminated laser beam width is narrower than the ultrasound/acoustic beam, the photoacoustic system is called optical resolution (OR-PAM) and if it is wider, the system is called acoustic resolution (AR-PAM) [73–75]. Utilizing the multi-wavelength spectroscopy and PAM allow the spectral imaging throughout the sample [76].

Blood flow imaging can be used in studying cancer and tumour since the increase in blood flow is associated with tumour growth. Photoacoustic Imaging can provide high resolution optical contrast images in tissues which can be utilized in monitoring the blood flow [13, 77]. In addition, all the developed methods in ultrasound flow imaging can be adapted in PA imaging. Doppler imaging [78–80] and quantitative methods like cross-correlation [77, 81] and differential phase analysis [82] are among the robust methods that measure the flow. Most of the PA systems are based on Q-switch lasers with relatively low Pulse Repetition Frequency (PRF). Imaging the high speed flow dynamics with these system are challenging. High PRF Pulsed Laser Diodes (PLDs) with relatively low power are evolved to address this requirement.

## 1.6. Thesis outline

Ultrasound and photoacoustic based vascular imaging are based on band limited transducer technologies which can be improved by utilizing a higher bandwidth transducers like CMUTs and PVDF. In this thesis we worked toward developing new low cost, broad band, and portable ultrasound and photoacoustic imaging devices and techniques for intravascular and vascular imaging which eventually will

provide higher image quality.

- **Chapter-2** investigates the CMUT array cross-coupling effect on a planar substrate using finite element method and experimentally is validated with the fabricated 1-D CMUT array. The analysis is extended to study the cross-talk in the rolled-up CMUT array.
- **Chapter-3** Investigates the first ever made, CMUT array for side-looking intravascular ultrasound imaging. Increasing the SNR using the coded excitation is demonstrated. A real time and pixel based beamforming is implemented for *ex vivo* imaging of human coronary artery specimen.
- **Chapter-4** studies the utilization of a kerfless, off-resonance PVDF array for photoacoustic imaging. Finite element analysis is performed to investigate the cross-talk between the elements and is benchmarked with experimental data. Discrete components are used to amplify the receiving signals which is proved that the proposed system is a broadband photoacoustic receiver.
- **Chapter-5** presents a design of a dual frequency carotid artery probe based on the outcomes of previous chapter. It shows using the off-resonance and kerfless PVDF array as a quarter matching layer could increase the bandwidth of the PZT stack used for ultrasound while attains high bandwidth for PA receive.
- **Chapter-6** explores a quantitative technique borrowed from quantum optics for photoacoustic flow velocity imaging. A fast PLD is used to image a flow phantom and microvasculature of the chorioallantoic membrane of a chicken embryo.
- **Chapter-7** examines the developed imaging systems and methods followed by discussion of the future for the proposed systems and techniques.

# References


[1] J. Curie and P. Curie, *Développement par compression de l'électricité polaire dans les cristaux hémièdres à faces inclinées,* Bulletin de minéralogie **3**, 90 (1880).

[2] I. Edler and C. H. Hertz, *The use of ultrasonic reflectoscope for the continuous recording of the movements of heart walls.* Clinical physiology and functional imaging **24**, 118 (1954).

[3] I. Edler, *Ultrasound cardiography,* Ultrasonics **5**, 72 (1967).

[4] H. Feigenbaum, R. L. Popp, S. B. Wolfe, B. L. Troy, J. F. Pombo, C. L. Haine, and H. T. Dodge, *Ultrasound measurements of the left ventricle: a correlative study with angiocardiography,* Archives of internal medicine **129**, 461 (1972).

[5] N. Bom, C. T. Lancee, J. Honkoop, and P. Hugenholtz, *Ultrasonic viewer for cross-sectional analyses of moving cardiac structures.* Biomedical engineering **6**, 500 (1971).

[6] K. J. Parker, R. M. Lerner, and R. C. Waag, *Attenuation of ultrasound: magnitude and frequency dependence for tissue characterization.* Radiology **153**, 785 (1984).

[7] F. d'Astous and F. Foster, *Frequency dependence of ultrasound attenuation and backscatter in breast tissue,* Ultrasound in medicine & biology **12**, 795 (1986).

[8] N. Bom, C. T. Lancee, and F. van Egmond, *An ultrasonic intracardiac scanner,* Ultrasonics **10**, 72 (1972).

[9] M. O'donnell, M. Eberle, D. Stephens, J. Litzza, K. San Vicente, and B. Shapo, *Synthetic phased array imaging of coronary arteries with an intraluminal array,* in *1995 IEEE Ultrasonics Symposium. Proceedings. An International Symposium*, Vol. 2 (IEEE, 1995) pp. 1251–1254.

[10] M. Xu and L. V. Wang, *Photoacoustic imaging in biomedicine,* Review of scientific instruments **77**, 041101 (2006).

[11] V. Ntziachristos and D. Razansky, *Molecular imaging by means of multispectral optoacoustic tomography (msot),* Chemical reviews **110**, 2783 (2010).

[12] S. Manohar and D. Razansky, *Photoacoustics: a historical review,* Advances in optics and photonics **8**, 586 (2016).

[13] A. B. E. Attia, G. Balasundaram, M. Moothanchery, U. Dinish, R. Bi, V. Ntziachristos, and M. Olivo, *A review of clinical photoacoustic imaging: Current and future trends,* Photoacoustics , 100144 (2019).

[14] P. K. Upputuri and M. Pramanik, *Fast photoacoustic imaging systems using pulsed laser diodes: a review,* Biomedical Engineering Letters **8**, 167 (2018).

[15] S. Iskander-Rizk, A. F. W. van der Steen, and G. van Soest, *Photoacoustic imaging for guidance of interventions in cardiovascular medicine,* Physics in Medicine & Biology **64**, 16TR01 (2019).

[16] S. Iskander-Rizk, P. Kruizinga, R. Beurskens, G. Springeling, F. Mastik, N. M. de Groot, P. Knops, A. F. W. van der Steen, and G. van Soest, *Real-time photoacoustic assessment of radiofrequency ablation lesion formation in the left atrium,* Photoacoustics **16**, 100150 (2019).

[17] S. Iskander-Rizk, P. Kruizinga, A. F. W. van der Steen, and G. van Soest, *Spectroscopic photoacoustic imaging of radiofrequency ablation in the left atrium,* Biomedical optics express **9**, 1309 (2018).

[18] M. Wu, G. Springeling, M. Lovrak, F. Mastik, S. Iskander-Rizk, T. Wang, H. M. M. van Beusekom, A. F. W. van der Steen, and G. van Soest, *Real-time volumetric lipid imaging in vivo by intravascular photoacoustics at 20 frames per second,* Biomedical optics express **8**, 943 (2017).

[19] B. Wang, J. L. Su, J. Amirian, S. H. Litovsky, R. Smalling, and S. Emelianov, *Detection of lipid in atherosclerotic vessels using ultrasound-guided spectroscopic intravascular photoacoustic imaging,* Optics Express **18**, 4889 (2010).

[20] S. Hu and L. V. Wang, *Photoacoustic imaging and characterization of the microvasculature,* Journal of Biomedical Optics **15**, 011101 (2010).

[21] E. W. Stein, K. Maslov, and L. V. Wang, *Noninvasive, in vivo imaging of blood-oxygenation dynamics within the mouse brain using photoacoustic microscopy,* Journal of Biomedical Optics **14**, 020502 (2009).

[22] K. S. Valluru, B. K. Chinni, N. A. Rao, S. Bhatt, and V. S. Dogra, *Basics and clinical applications of photoacoustic imaging,* Ultrasound Clinics **4**, 403 (2009).

[23] J. L. Su, B. Wang, K. E. Wilson, C. L. Bayer, Y.-S. Chen, S. Kim, K. A. Homan, and S. Y. Emelianov, *Advances in clinical and biomedical applications of photoacoustic imaging,* Expert Opinion on Medical Diagnostics **4**, 497 (2010).

[24] M. I. Haller and B. T. Khuri-Yakub, *A surface micromachined electrostatic ultrasonic air transducer,* IEEE transactions on ultrasonics, ferroelectrics, and frequency control **43**, 1 (1996).

[25] H. Soh, I. Ladabaum, A. Atalar, C. Quate, and B. Khuri-Yakub, *Silicon micromachined ultrasonic immersion transducers,* Applied physics letters **69**, 3674 (1996).

[26] X. Jin, I. Ladabaum, and B. T. Khuri-Yakub, *The microfabrication of capacitive ultrasonic transducers,* Journal of Microelectromechanical Systems **7**, 295 (1998).

[27] X. Jin, I. Ladabaum, F. L. Degertekin, S. Calmes, and B. T. Khuri-Yakub, *Fabrication and characterization of surface micromachined capacitive ultrasonic immersion transducers,* Journal of Microelectromechanical systems **8**, 100 (1999).

[28] P.-C. Eccardt, K. Niederer, T. Scheiter, and C. Hierold, *Surface micromachined ultrasound transducers in cmos technology,* in *1996 IEEE Ultrasonics Symposium. Proceedings*, Vol. 2 (IEEE, 1996) pp. 959–962.

[29] E. Cianci, V. Foglietti, G. Caliano, and M. Pappalardo, *Micromachined capacitive ultrasonic transducers fabricated using silicon on insulator wafers,* Microelectronic engineering **61**, 1025 (2002).

[30] Y. Huang, A. S. Ergun, E. Haeggstrom, M. H. Badi, and B. T. Khuri-Yakub, *Fabricating capacitive micromachined ultrasonic transducers with wafer-bonding technology,* Journal of microelectromechanical systems **12**, 128 (2003).

[31] N. Apte, K. K. Park, A. Nikoozadeh, and B. T. Khuri-Yakub, *Bandwidth and sensitivity optimization in CMUTs for airborne applications,* in *2014 IEEE International Ultrasonics Symposium*, IEEE (IEEE, 2014) pp. 166–169.

[32] B. T. Khuri-Yakub and Ö. Oralkan, *Capacitive micromachined ultrasonic transducers for medical imaging and therapy,* Journal of micromechanics and microengineering **21**, 054004 (2011).

[33] G. Gurun, C. Tekes, J. Zahorian, T. Xu, S. Satir, M. Karaman, J. Hasler, and F. L. Degertekin, *Single-chip cmut-on-cmos front-end system for real-time volumetric ivus and ice imaging,* IEEE transactions on ultrasonics, ferroelectrics, and frequency control **61**, 239 (2014).

[34] J. Zahorian, M. Hochman, T. Xu, S. Satir, G. Gurun, M. Karaman, and F. L. Degertekin, *Monolithic cmut-on-cmos integration for intravascular ultrasound applications,* IEEE transactions on ultrasonics, ferroelectrics, and frequency control **58**, 2659 (2011).

[35] K. K. Park, Ö. Oralkan, and B. T. Khuri-Yakub, *A comparison between conventional and collapse-mode capacitive micromachined ultrasonic transducers in 10-mhz 1-d arrays,* IEEE transactions on ultrasonics, ferroelectrics, and frequency control **60**, 1245 (2013).

[36] M. Pekař, W. U. Dittmer, N. Mihajlović, G. van Soest, and N. de Jong, *Frequency tuning of collapse-mode capacitive micromachined ultrasonic transducer,* Ultrasonics **74**, 144 (2017).

[37] M. Pekař, A. F. Kolen, H. Belt, F. van Heesch, N. Mihajlović, I. E. Hoefer, T. Szili-Török, H. J. Vos, J. G. Bosch, G. van Soest, and A. F. W. van der Steen, *Preclinical testing of frequency-tunable capacitive micromachined ultrasonic transducer probe prototypes,* Ultrasound in medicine & biology **43**, 2079 (2017).

[38] F. Değertekin, M. Karaman, and R. O. Güldiken, *Forward-looking ivus imaging using an annular-ring cmut array,* (2005), 10.1109/ULTSYM.2005.1602813.

[39] F. L. Değertekin, R. O. Güldiken, and M. Karaman, *Annular-ring cmut arrays for forward-looking ivus: Transducer characterization and imaging,* IEEE transactions on ultrasonics, ferroelectrics, and frequency control **53**, 474 (2006).

[40] X. Zhuang, D.-S. Lin, Ö. Oralkan, and B. T. Khuri-Yakub, *Fabrication of flexible transducer arrays with through-wafer electrical interconnects based on trench refilling with pdms,* Journal of Microelectromechanical Systems **17**, 446 (2008).

[41] X. Zhang, X. Wu, O. J. Adelegan, F. Y. Yamaner, and O. Oralkan, *Backward-mode photoacoustic imaging using illumination through a cmut with improved transparency,* IEEE Transactions on Ultrasonics, Ferroelectrics, and Frequency Control **65**, 85 (2018).

[42] Z. Li, A. K. Ilkhechi, and R. Zemp, *Transparent capacitive micromachined ultrasonic transducers (cmuts) for photoacoustic applications,* Optics express **27**, 13204 (2019).

[43] Z. Wang, W. Huang, X. Jiang, K. H. Martin, and P. A. Dayton, *Dual-frequency ivus array for contrast enhanced intravascular ultrasound imaging,* in *2015 IEEE International Ultrasonics Symposium (IUS)* (IEEE, 2015) pp. 1–4.

[44] S. Li, J. Kim, Z. Wang, X. Jiang, S. Kasoji, B. Lindsey, and P. A. Dayton, *A 3 mhz/18 mhz dual-layer co-linear array for transrectal acoustic angiography,* in *2015 IEEE International Ultrasonics Symposium (IUS)* (IEEE, 2015) pp. 1–4.

[45] S. Saitoh, M. Izumi, and Y. Mine, *A dual frequency ultrasonic probe for medical applications,* IEEE transactions on ultrasonics, ferroelectrics, and frequency control **42**, 294 (1995).

[46] V. Daeichin, C. Chen, Q. Ding, M. Wu, R. Beurskens, G. Springeling, E. Noothout, M. D. Verweij, K. W. van Dongen, J. G. Bosch, *et al.*, *A broadband polyvinylidene difluoride-based hydrophone with integrated readout circuit for intravascular photoacoustic imaging,* Ultrasound in medicine & biology **42**, 1239 (2016).

[47] E. Wilkins, L. Wilson, K. Wickramasinghe, P. Bhatnagar, J. Leal, R. Luengo-Fernandez, R. Burns, M. Rayner, and N. Townsend, *European Cardiovascular Disease Statistics 2017* (European Heart Network, Belgium, 2017).

[48] R. Ross, *The pathogenesis of atherosclerosis: a perspective for the 1990s,* Nature **362**, 801 (1993).

[49] *Apparatus for ultrasonically examining a hollow organ,* (1972).

[50] A. F. W. van der Steen, R. A. Baldewsing, F. L. Değertekin, S. Emelianov, M. E. Frijlink, Y. Furukawa, D. Goertz, M. Karaman, P. T. Khuri-Yakub, K. Kim, *et al.*, *Ivus beyond the horizon.* EuroIntervention: journal of EuroPCR in collaboration

with the Working Group on Interventional Cardiology of the European Society of Cardiology **2**, 132 (2006).

[51] W. Li, *Image and signal processing in intravascular ultrasound*, Ph.D. thesis, Erasmus MC University Medical center Rotterdam (1997).

[52] Y. Takeuchi, *An investigation of a spread energy method for medical ultrasound systems: Part one: Theory and investigation,* Ultrasonics **17**, 175 (1979).

[53] M. O'Donnell, *Coded excitation system for improving the penetration of real-time phased-array imaging systems,* IEEE transactions on ultrasonics, ferroelectrics, and frequency control **39**, 341 (1992).

[54] P.-C. Li, E. Ebbini, and M. O'Donnell, *A new filter design technique for coded excitation systems,* IEEE transactions on ultrasonics, ferroelectrics, and frequency control **39**, 693 (1992).

[55] M. Pollakowski and H. Ermert, *Chirp signal matching and signal power optimization in pulse-echo mode ultrasonic nondestructive testing,* IEEE transactions on ultrasonics, ferroelectrics, and frequency control **41**, 655 (1994).

[56] N. Rao, *Investigation of a pulse compression technique for medical ultrasound: A simulation study,* Medical and Biological Engineering and Computing **32**, 181 (1994).

[57] J. Shen and E. S. Ebbini, *A new coded-excitation ultrasound imaging system. i. basic principles,* IEEE transactions on ultrasonics, ferroelectrics, and frequency control **43**, 131 (1996).

[58] R. Kažys, L. Svilainis, and L. Mažeika, *Application of orthogonal ultrasonic signals and binaural processing for imaging of the environment,* Ultrasonics **38**, 171 (2000).

[59] T. Misaridis and J. A. Jensen, *Use of modulated excitation signals in medical ultrasound. part i: Basic concepts and expected benefits,* IEEE transactions on ultrasonics, ferroelectrics, and frequency control **52**, 177 (2005).

[60] S. Iskander-Rizk, P. Kruizinga, G. Springeling, H. J. Vos, A. F. W. van der Steen, and G. van Soest, *Photoacoustic imaging of sub-diffraction objects with spectral contrast,* Optics letters **42**, 191 (2017).

[61] R. J. Zemp, *Quantitative photoacoustic tomography with multiple optical sources,* Applied optics **49**, 3566 (2010).

[62] J. Yao, J. Xia, and L. V. Wang, *Multiscale functional and molecular photoacoustic tomography,* Ultrasonic imaging **38**, 44 (2016).

[63] F. J. O. Landa, X. L. Deán-Ben, R. Sroka, and D. Razansky, *Volumetric optoacoustic temperature mapping in photothermal therapy,* Scientific reports **7**, 1 (2017).

1

[64] J. Xia, J. Yao, and L. V. Wang, *Photoacoustic tomography: principles and advances,* Electromagnetic waves (Cambridge, Mass.) **147**, 1 (2014).

[65] D. Wu, L. Huang, M. S. Jiang, and H. Jiang, *Contrast agents for photoacoustic and thermoacoustic imaging: a review,* International journal of molecular sciences **15**, 23616 (2014).

[66] M. Li, Y. Tang, and J. Yao, *Photoacoustic tomography of blood oxygenation: a mini review,* Photoacoustics **10**, 65 (2018).

[67] B. Lengenfelder, F. Mehari, M. Hohmann, M. Heinlein, E. Chelales, M. J. Waldner, F. Klämpfl, Z. Zalevsky, and M. Schmidt, *Remote photoacoustic sensing using speckle-analysis,* Scientific reports **9**, 1 (2019).

[68] L. V. Wang and S. Hu, *Photoacoustic tomography: in vivo imaging from organelles to organs,* science **335**, 1458 (2012).

[69] K. H. Song, G. Stoica, and L. V. Wang, *In vivo three-dimensional photoacoustic tomography of a whole mouse head,* Optics letters **31**, 2453 (2006).

[70] A. Dima, N. C. Burton, and V. Ntziachristos, *Multispectral optoacoustic tomography at 64, 128, and 256 channels,* Journal of biomedical optics **19**, 036021 (2014).

[71] L. Lin, P. Hu, J. Shi, C. M. Appleton, K. Maslov, L. Li, R. Zhang, and L. V. Wang, *Single-breath-hold photoacoustic computed tomography of the breast,* Nature communications **9**, 1 (2018).

[72] M. Heijblom, D. Piras, F. M. van den Engh, M. van der Schaaf, J. M. Klaase, W. Steenbergen, and S. Manohar, *The state of the art in breast imaging using the twente photoacoustic mammoscope: results from 31 measurements on malignancies,* European radiology **26**, 3874 (2016).

[73] L. V. Wang, *Multiscale photoacoustic microscopy and computed tomography,* Nature photonics **3**, 503 (2009).

[74] K. Maslov, H. F. Zhang, S. Hu, and L. V. Wang, *Optical-resolution photoacoustic microscopy for in vivo imaging of single capillaries,* Optics letters **33**, 929 (2008).

[75] W. Xing, L. Wang, K. Maslov, and L. V. Wang, *Integrated optical-and acoustic-resolution photoacoustic microscopy based on an optical fiber bundle,* Optics letters **38**, 52 (2013).

[76] S. Iskander-Rizk, M. Visscher, A. M. Moerman, S.-A. Korteland, K. Van der Heiden, A. F. W. van der Steen, and G. van Soest, *Micro spectroscopic photoacoustic ($\mu$spa) imaging of advanced carotid atherosclerosis,* Photoacoustics , 100261 (2021).

[77] J. Yao, K. I. Maslov, and L. V. Wang, *In vivo photoacoustic tomography of total blood flow and potential imaging of cancer angiogenesis and hypermetabolism,* Technology in cancer research & treatment **11**, 301 (2012).

[78] H. Fang, K. Maslov, and L. V. Wang, *Photoacoustic doppler effect from flowing small light-absorbing particles,* Physical Review Letters **99**, 184501 (2007).

[79] J. Brunker and P. Beard, *Pulsed photoacoustic doppler flowmetry using time-domain cross-correlation: accuracy, resolution and scalability,* The Journal of the Acoustical Society of America **132**, 1780 (2012).

[80] J. Brunker and P. Beard, *Acoustic resolution photoacoustic doppler velocimetry in blood-mimicking fluids,* Scientific Reports **6**, 20902 (2016).

[81] J. Yao, L. Wang, J.-M. Yang, K. I. Maslov, T. T. Wong, L. Li, C.-H. Huang, J. Zou, and L. V. Wang, *High-speed label-free functional photoacoustic microscopy of mouse brain in action,* Nature methods **12**, 407 (2015).

[82] S. Iskander-Rizk, R. Pakdaman Zangabad, P. Kruizinga, A. F. W. van der Steen, and G. van Soest, *Differential phase analysis for high frame rate photoacoustic vector flow imaging,* imaging **1**, 2 (2021).

# 2

# Mutual Radiation Impedance of Circular CMUTs on a Cylinder

**Reza Pakdaman Zangabad,** Ayhan Bozkurt,
Göksenin Yaralıoğlu, Johan G. Bosch
Gijs van Soest, Antonius F. W. van der Steen

This chapter has been published in proceeding of 2016 IEEE International Ultrasonics Symposium (IUS) [1].

*In ultrasound imaging, cross coupling of transducer elements through the medium has significant effect on the frequency response, thus affecting the quality of the ultrasound image. In Side-Looking Intravascular Ultrasound (SL-IVUS) imaging a radial image of the vessel wall is formed using a transducer array in a cylindrical configuration. Recent advances in Capacitive Micromachined Ultrasound Transducer (CMUT) fabrication and integration techniques led to realization of CMUT arrays that can be wrapped into a cylinder shape and mounted on a catheter tip. In this paper, we present the calculation of radiation impedance of un-collapse CMUT arrays on a planar rigid baffle and on a cylinder using Finite Element Method (FEM) simulation. We link the crosstalk between planar CMUT elements with dips in frequency spectrum from experimental data and conclude that decreasing the cylinder radius causes downshift of the dips in frequency response. In the case of our device, these changes are too small to have detrimental effects on the array bandwidth.*

## 2.1. Introduction



Intravascular ultrasound (IVUS) imaging is an established technique for imaging vessel walls and atherosclerotic plaques [2] that has been in use clinically since the early 90's. Commercial devices use piezoelectric (PZT) transducers, either mechanically rotating single elements or PZT phased arrays in a cylindrical configuration. Both techniques create side-looking IVUS (SL-IVUS) images providing a transversal cross section of the vessel wall. Limitations of single elements are the mechanical rotation, associated with frame rate limits and irregular rotation artifacts; the PZT phased arrays suffer from complex, costly construction and interconnection, and limited element bandwidth and sensitivity.

A promising alternative for the PZT array are the Capacitive Micromachined Ultrasound Transducers (CMUT). CMUTs [3] are micro-electromechanical devices that consist of a flexible membrane suspended over a substrate with spacing in submicrometer range. Two electrodes are placed in membrane and substrate acting as parallel-plate capacitor, and an electrostatic force deforms the membrane when a DC bias voltage is applied. Superimposing a high-frequency voltage will cause the membrane to vibrate in the ultrasound frequency range and act as an ultrasound transmitter. Similarly, mechanical vibration of the membrane will change the capacitance of the device, acting as an ultrasound receiver. Advantages of CMUT over PZT are the relatively large bandwidth with comparable sensitivity, the freedom of geometric design, ease of large-scale production, miniaturization and seamless integration with electronics. The acoustic properties can also be dynamically adjusted by changing the DC bias voltage. Depending on the applied DC voltage, a CMUT works in either conventional (un-collapse) or collapse mode, with considerably different acoustic behavior. All these properties offer great benefits for catheter-based SL-IVUS applications. Moreover, new techniques for fabrication of flexible CMUT arrays [4] enable wrapping of the array into a small-radius cylindrical configuration that can be placed in a catheter tip for SL-IVUS imaging.
A drawback of CMUT is the complexity of the devices and the great number of design parameters that influence the acoustic behavior. Also, many unwanted effects that are relatively well-controlled in PZT array fabrication, can play a large role in CMUT and need to be assessed, understood and controlled. One of the important phenomena which affects CMUT device performance is acoustic crosstalk: the vibration of a CMUT membrane creates acoustic waves that are coupled to adjacent elements and degrade the CMUT array performance. Such coupling can occur via the silicon substrate or via the fluid-substrate interfaces [5, 6]. For coupling via the substrate, several solutions have been proposed, such as the use of backing layers, thinning of the substrate or deep trench isolation of elements [6, 7].

The mutual coupling or crosstalk through the surrounding fluid medium is highly related to cell and element geometry. Usually CMUT membranes and elements are closely packed for achieving broad operational bandwidths; however, this could excite additional membrane modes due to the fluid coupling. It has been shown that such crosstalk is the main reason for ripples in the frequency response of the array [8–10] and how it degrades the bandwidth and image quality of ultrasound B-mode imaging [5, 11–13]. Since decreasing the pitch between CMUT cells and elements

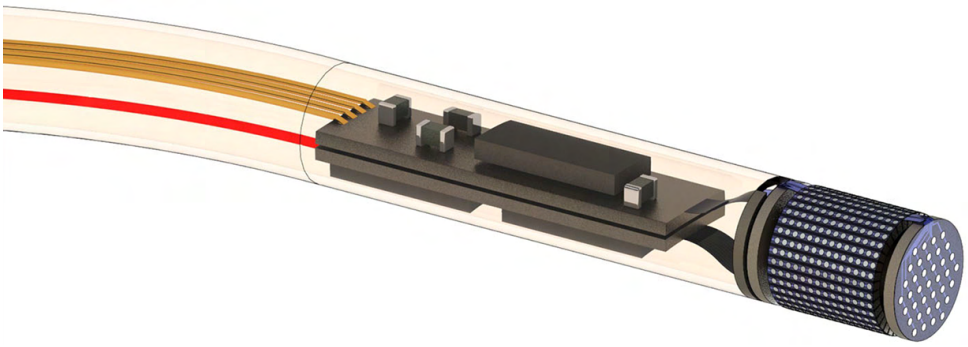

Figure 2.1: An artistic illustration of a catheter built on the INCITE microelectronics platform [17]

could increase bandwidth and introduce ripple at the same time, the cross-coupling between CMUT cells and elements should be scrutinized and element spacing should be optimized to reduce the coupling effect on the bandwidth of the transducer.
An interpretation of the main mechanism of coupling between the CMUT membranes based on the propagation of surface acoustic waves at the fluid-silicon interface is introduced in [9]. In this paper, we are following different interpretation given by Caronti et al. which is based on effect of acoustic loading of pressure waves propagating from a membrane to the surface of another membrane[14]. The mutual coupling or crosstalk through the surrounding fluid medium can thus be related to the radiation impedance of elements of an array. This has been studied before for CMUTs placed on a planar infinite rigid baffle operating in both collapse [15] and un-collapse regimes [16]. In this paper, we study the influence of the warping of the array on the crosstalk, via the radiation impedance. We perform FEM simulations of several array configurations, flat and warped, and compare to some measured frequency characteristics.

## 2.2. materials and methods

Within the context of the INCITE (Intelligent Catheters in Advanced Systems for Interventions) project, Erasmus MC and Philips are working on the realization of an Intravascular Ultrasound transducer in CMUT array technology. INCITE is a research project focusing on the development of a technology platform that will enable advanced imaging, sensing (pressure, force, biomarker) and steering functions to be integrated into (sub)millimeter size in-body catheters and surgical instruments for emerging complex minimally invasive cardio, neuro, and peripheral vascular interventions [17]. Figure 2.1 gives an artistic impression of the catheter which will be developed. The cylindrical array can be seen at the tip of the catheter and will be realized by wrapping a planar CMUT array on a cylinder with 0.6 mm radius. The influence of the wrapping on the crosstalk is unknown and will be investigated in

this paper by means of Finite Element Method (FEM) based simulation. The geometry that we are simulating is shown in Figure 2.2. The device sizes are similar to the array fabricated within the INCITE project. Circular CMUTs are arranged in columns forming 96 elements and a pair of elements forms an island. As specified in Figure 2.2, the pitch between CMUTs within elements (1), element pitch within an island (2), and element pitch between islands (3) are 38 µm, 33 µm, and 45 µm, respectively. A 48 elements CMUT planar linear array has been fabricated and characterized in water. For the characterization, CMUTs are biased with 10V DC and a pulse of 10ns, 30V is applied to all elements and the generated pressure waves are measured with calibrated hydrophone at focal point of the linear array. Then the measured signal is compensated for attenuation and diffractions. Figure 2.3 demonstrates the transmit transfer function of the array operating in conventional mode.

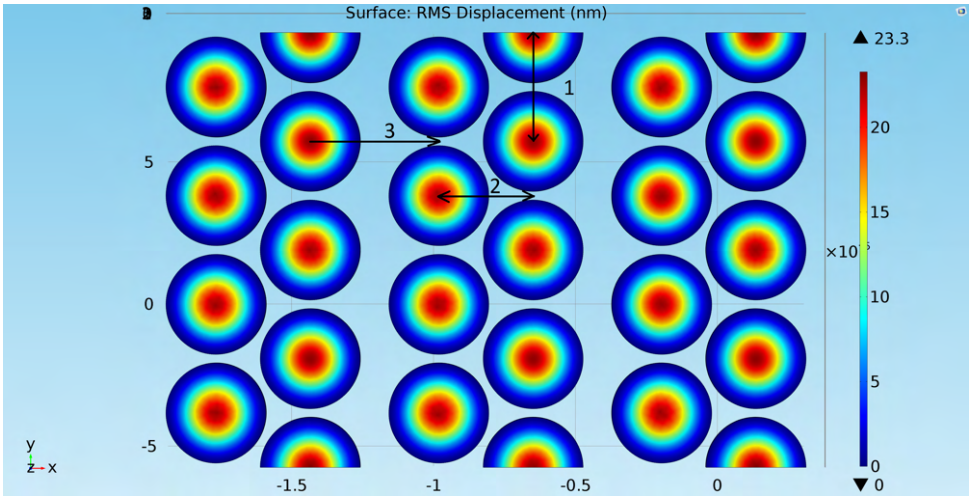


Figure 2.2: 1D CMUT linear array configuration showing 6 elements in 3 islands.

| Parameter | Description | Value |
|---|---|---|
| **a** | Membrane diameter | 35 µm |
| **ti** | Insulation Layer Thickness | 300 nm |
| **tg** | Gap Height | 35 nm |
| **tm** | Membrane thickness | 2 µm |
| **te** | Embedded Electrode Thickness | 100 nm |

Table 2.1: CMUT cell parameters used in simulation and are similar with fabricated device parameter

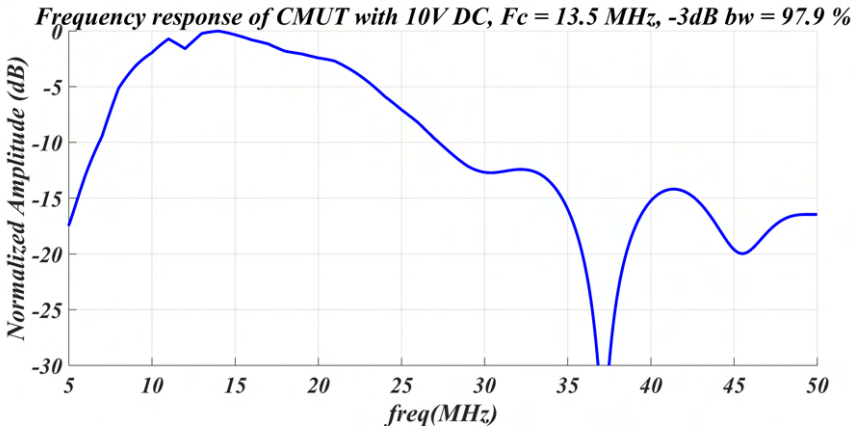


Figure 2.3: Hydrophone measurement of linear array CMUTs

### 2.2.1. FEM Modeling of Acoustic Coupling of CMUT membranes

3-D FEM analysis is carried out using COMSOL Multiphysics 5.0 for analyzing the velocity and pressure profile on the surface of immersed CMUTs with cell parameters specified in Table 2.1 that are similar to those used in device fabrication. Simulations are performed both for the planar device and cylinders with 0.6 and 0.5 mm radius. A Perfectly Matched Layer (PML) is used as an absorbing boundary which is located $2\lambda_0$ away of surface of the array at the lowest frequency and the model is simplified by simulating a portion of the array with appropriate symmetry boundaries and also periodic boundary condition along the y-axis (Figure 2.2). For simulating the crosstalk in cylindrical case, the same islands are placed on a cylinder with 0.6 mm and the model is simplified by simulating 1/24 of the array with appropriate symmetry boundaries and also periodic boundary condition along the y-axis (Figure 2.5). Also the domain mesh size is set to the minimum acceptable size of $\frac{\lambda_1}{10}$ at the highest operating frequency.
The radiation impedance of a CMUT cell is defined as the ratio of amount of total power, *P*, acting on the surface of the CMUT cell to the square of the absolute value of an arbitrary reference velocity, *V* [18]:

$$Z = \frac{P}{|V|^2} = \frac{\int_S p(r)v^*(r)dS}{|V|^2} \tag{2.1}$$

where *p(r)* and $v^*(r)$ are the pressure and complex conjugate of the particle velocity on the surface, S, of the cell at radial coordinate *r*. The equation of the spatial rms velocity, $V_{rms}$, which is a complex value could be explained as [19]:

$$V_{rms} = \sqrt{\frac{1}{S}\int_S Re[v(r)]^2 dS} + i\sqrt{\frac{1}{S}\int_S Im[v(r)]^2 dS} \tag{2.2}$$

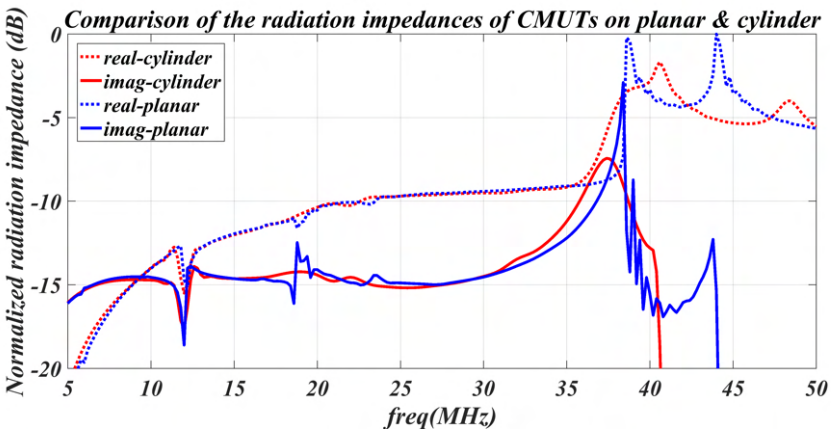


Figure 2.4: Normalized radiation impedance of 1D CMUT linear array and the same configuration wrapped around a cylinder with 600 μm radius

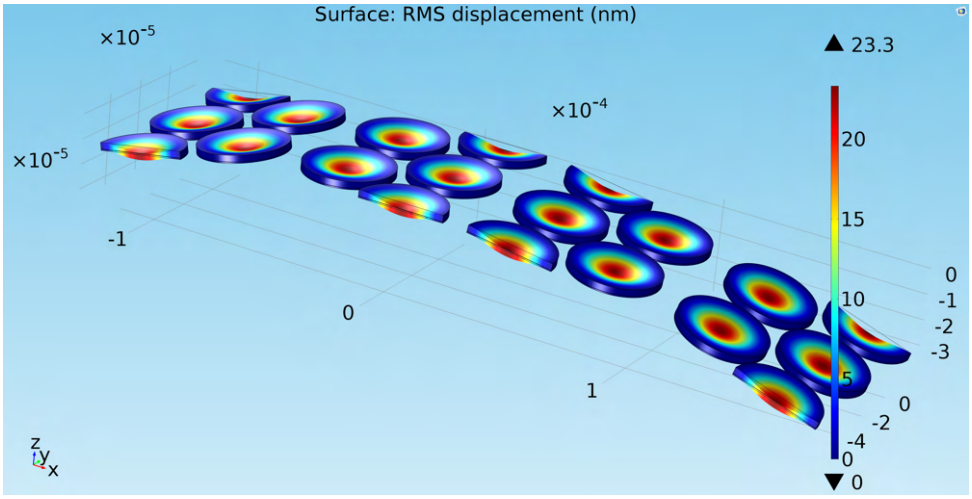


Figure 2.5: Configuration of CMUT array on 0.6mm cylinder

Note that average velocity has been used as reference velocity in most of the works regarding the calculation of radiation impedance; $V = V_{ave}$; however this paper uses the spatial RMS velocity in order to avoid the problem of higher mode CMUT velocity profile which at some pints $V_{ave}$ becomes zero eventuating in infinite radiation impedance. Figure 2.4 is showing the radiation impedance of CMUTs array on planar rigid baffle and also on cylinder with 600 μm radius. it is demonstrating that there are strong interactions at specific frequencies. As it has been reported [8–10], the peaks in the radiation reactance correspond to the dips in the frequency response curve. From comparison to Figure 2.3, we can conclude that our simulation correctly identifies the measured dips.

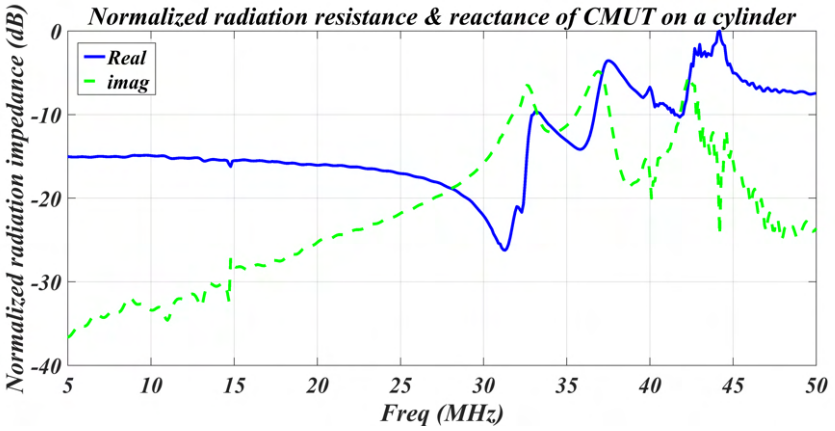


Figure 2.6: Normalized radiation resistance and reactance of CMUT on a cylinder with 600 μm radius

The main peak at 37.5 MHz of radiation reactance corresponds to a wavelength of 45μm which matches the pitch between islands (number 3 in Figure 2.2) [11]. The peaks at 44 MHz and 12 MHz correspond to wavelengths of 33 μm and 123 μm, which matches the distances between CMUT cells within the element and distance between first and the third island; respectively. Apparently the cross coupling effect between islands is the dominant effect.

In the cylindrical case, where we are using the same configuration as the planar case, the coupling effects have been detected for slightly lower frequencies with lower amplitudes. The lower amplitude is likely because the total power on surface of CMUTs generated from neighboring island/element is reduced by a factor of $\cos(\alpha)$ where $\alpha$ is the angle between surface normals of two islands. The lower frequency is supposed to be due to the slightly longer pathway through the fluid. The effects of the wrapping are too small to be detrimental for the bandwidth of our array.

Furthermore, we investigated the mutual coupling for arrays with slightly different geometry. We used a pitch between CMUTs within element, element pitch in an island, and pitch between islands as 40 μm, 35 μm, and 45 μm, respectively and used cylinders of 600 μm and 500 μm radius. Figure 2.6 and Figure 2.7 depict the coupling effects. We demonstrate that decreasing the radius of the cylinder for the same array will shift the coupling towards lower frequencies and could introduce additional crosstalk peaks between elements and islands.

In an equivalent circuit model of the CMUT array[20], the radiation impedance could be modeled with lump circuit elements and the real part of it could be associated with the thermal noise. This could be used to optimize the signal-to-noise ratio of the CMUT based ultrasound imaging system.

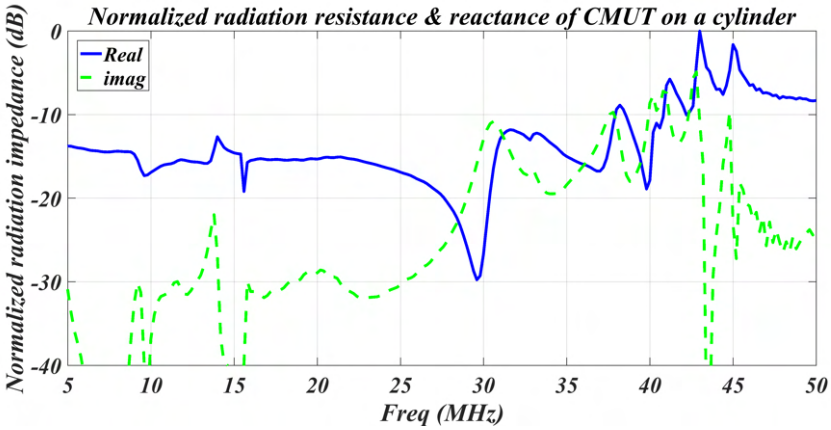


Figure 2.7: Normalized radiation resistance and reactance of CMUT on a cylinder with 500 µm radius

## 2.3. Conclusion

We have analyzed the coupling effect between CMUT elements, based on finite-element method and show that the resulting radiation reactance peaks correspond with dips in the experimentally measured frequency response. Moreover, we compared the radiation impedance between planar and cylindrical arrays and conclude that the cylindrical wrapping causes a slight downshift in frequency and it can introduce additional peaks. Also we investigated the crosstalk between elements on cylinders with 0.5 mm and 0.6 mm radius and conclude that decreasing the radius could shift crosstalk toward lower frequencies. The results show that radiation reactance or mutual coupling can be considerable at some frequencies eventuating in different acoustic loading on the CMUT cells and degrading the array performance. The wrapping is not expected to have a detrimental effect on bandwidth performance of the INCITE CMUT array.

## Acknowledgment

This work was done in the frame of the ENIAC “INCITE” project No.621278. INCITE is an ENIAC JU project and is co-funded by grants from the Netherlands, Finland, Hungary, France, Ireland, Sweden, Spain, and Poland.

# References


[1] R. Pakdaman Zangabad, A. Bozkurt, G. Yaralıoğlu, J. G. Bosch, G. van Soest, and A. F. W. van der Steen, *Mutual radiation impedance of circular cmuts on a cylinder,* in *Ultrasonics Symposium (IUS), 2016 IEEE International* (IEEE, 2016) pp. 1–4.

[2] M. O'Donnell, *Phased array beam forming from a circular array: applications to imaging of coronary arteries,* in *Ultrasonics Symposium, 1991. Proceedings., IEEE 1991* (1991) pp. 637–640 vol.1.

[3] B. Khuri-Yakub, F. Degertekin, X.-C. Jin, S. Calmes, I. Ladabaum, S. Hansen, and X. Zhang, *Silicon micromachined ultrasonic transducers,* in *Ultrasonics Symposium, 1998. Proceedings., 1998 IEEE*, Vol. 2 (1998) pp. 985–991 vol.2.

[4] X. Zhuang, D.-S. Lin, Ö. Oralkan, and B. T. Khuri-Yakub, *Fabrication of flexible transducer arrays with through-wafer electrical interconnects based on trench refilling with pdms,* Journal of Microelectromechanical Systems **17**, 446 (2008).

[5] B. Bayram, M. Kupnik, G. G. Yaralıoğlu, Ö. Oralkan, A. Ergun, S. Wong, and B. Khuri-Yakub, *Finite element modeling and experimental characterization of crosstalk in 1-d cmut arrays,* Ultrasonics, Ferroelectrics, and Frequency Control, IEEE Transactions on **54**, 418 (2007).

[6] I. Ladabaum, P. Wagner, C. Zanelli, J. Mould, P. Reynolds, and G. Wojcik, *Silicon substrate ringing in microfabricated ultrasonic transducers,* in *Ultrasonics Symposium, 2000 IEEE*, Vol. 1 (2000) pp. 943–946 vol.1.

[7] B. Khuri-Yakub, A. Ergun, and G. Yaralıoğlu, *Capacitive membrane ultrasonic transducers with reduced bulk wave generation and method,* (2005), uS Patent App. 11/098,863.

[8] A. Bozkurt, F. Degertekin, A. Atalar, and B. Khuri-Yakub, *Analytic modeling of loss and cross-coupling in capacitive micromachined ultrasonic transducers,* in *Ultrasonics Symposium, 1998. Proceedings., 1998 IEEE*, Vol. 2 (1998) pp. 1025–1028 vol.2.

[9] P. C. Eccardt and K. Niederer, *Micromachined ultrasound transducers with improved coupling factors from a CMOS compatible process,* Ultrasonics **38**, 774 (2000).

[10] M. Pappalardo, A. Caronti, C. Longo, A. Savoia, P. Gatta, and G. Caliano, *5f-2 analysis of acoustic interaction effects and crosstalk in cmut linear arrays for medical imaging,* in *2006 IEEE Ultrasonics Symposium* (2006) pp. 582–585.

[11] X. Jin, O. Oralkan, F. L. Degertekin, and B. T. Khuri-Yakub, *Characterization of one-dimensional capacitive micromachined ultrasonic immersion transducer arrays,* IEEE Transactions on Ultrasonics, Ferroelectrics, and Frequency Control **48**, 750=760 (2001).

[12] P. C. Eccardt, A. Lohfink, and H. G. v. Garssen, *Analysis of crosstalk between fluid coupled cmut membranes,* in *IEEE Ultrasonics Symposium, 2005.*, Vol. 1 (2005) pp. 593–596.

[13] J. Dias, *An experimental investigation of the cross-coupling between elements of an acoustic imaging array transducer,* Ultrasonic Imaging **4**, 44 (1982).

[14] A. Caronti, A. Savoia, G. Caliano, and M. Pappalardo, *Acoustic coupling in capacitive microfabricated ultrasonic transducers: modeling and experiments,* IEEE Transactions on Ultrasonics, Ferroelectrics, and Frequency Control **52**, 2220 (2005).

[15] M. Senlik, S. Olcum, H. Koymen, and A. Atalar, *Radiation impedance of an array of circular capacitive micromachined ultrasonic transducers,* Ultrasonics, Ferroelectrics, and Frequency Control, IEEE Transactions on **57**, 969 (2010).

[16] A. Ozgurluk, A. Atalar, H. Koymen, and S. Olcum, *Radiation impedance of collapsed capacitive micromachined ultrasonic transducers,* IEEE Transactions on Ultrasonics, Ferroelectrics, and Frequency Control **59**, 1301 (2012).

[17] ENIAC, *INCITE,* `http://www.incite-project.eu/` (2016).

[18] C. H. Sherman, *Analysis of acoustic interactions in transducer arrays,* IEEE Transactions on Sonics and Ultrasonics **13**, 9 (1966).

[19] C. E. Wallace, *Radiation resistance of a baffled beam,* The Journal of the Acoustical Society of America **51**, 936 (1972).

[20] R. Pakdaman Zangabad, A. Bozkurt, and G. Yaralıoğlu, *Signal to noise ratio optimization for a cmut based medical ultrasound imaging system,* in *Ultrasonics Symposium (IUS), 2015 IEEE International* (2015) pp. 1–4.

# 3

# Real-Time Coded Excitation Imaging Using a CMUT-based Side Looking Array for Intravascular Ultrasound

**Reza Pakdaman Zangabad,** Johan G. Bosch, Frits Mastik, Robert H.S.H. Beurskens, Vincent A. Henneken, Johannes W. Weekamp, Antonius F. W. van der Steen, Gijs van Soest

This chapter has been published in IEEE Transactions on Ultrasonics, Ferroelectrics, and Frequency Control (TUFFC) [1].

*Intravascular ultrasound (IVUS) is a well-established diagnostic method that provides images of the vessel wall and atherosclerotic plaques. We investigate the potential for phased-array IVUS utilizing Coded Excitation (CE) for improving the penetration depth and image signal-to-noise ratio (SNR). It is realized on a new experimental broadband Capacitive Micromachined Ultrasound Transducer (CMUT) array with 96 elements placed at the circumference of a catheter tip with 1.2 mm diameter. We characterized the array performance for CE imaging and showed that the -6dB device bandwidth at 30 V DC biasing is 25 MHz with 20 MHz center frequency and has transmit sensitivity of 37 kPa/V at that frequency.*

*We designed a linear Frequency Modulation (FM) signal to improve penetration depth by compensating high-frequency attenuation while preserving resolution by a mismatched filter reconstruction. We imaged a wire phantom and a human coronary artery plaque. By assessing the image quality of the reconstructed wire phantom image, we achieved 60 μm and 70 μm axial resolution using the short pulse and coded signal, respectively and gained 8 dB in SNR. Our developed system shows 20 frame per second, pixel-based beam-formed, real-time IVUS images.*

## 3.1. Introduction

Diseases of the heart and circulatory system (cardiovascular disease or CVD) are the main causes of death in Europe, accounting for 1.8 million deaths and more than 11 million hospitalizations each year in the EU [2]. More than a third (36%) of all deaths are from CVD. With an ageing population, the prevalence of many cardiovascular diseases increases strongly. The resulting economic, as well as human costs are tremendous. Overall, CVD is estimated to cost the EU economy almost 210 billion euros a year, due to healthcare costs and lost productivity.



Atherosclerosis, which is a chronic disease and asymptomatic at early stages, is characterized by the thickening of the arterial vessel wall due to the buildup of plaque in the inner side of arteries [3]. In the coronary circulation, it is treated commonly by percutaneous coronary intervention (PCI): catheter-based balloon dilation and implantation of a stent. Intravascular Ultrasound (IVUS) is an established technique that images the vessel wall and atherosclerotic plaque [4] using a catheter-mounted transducer. It may be used to guide PCI and has significant outcomes benefits, including a 50% reduction in CV death after PCI [5, 6].

Commercial devices - either mechanically rotating single element or electronically scanned in a phased array configuration - use high frequency (20MHz-60MHz) piezoelectric transducers at the tip of a coronary catheter in order to assess the morphological properties of plaques and implanted stents. After two decades of relatively slow progress, innovations in IVUS imaging technology are now being introduced into the clinical arena. Improved resolution, dynamic range and image contrast may be valuable for identifying plaque components like calcification, lipid-rich necrotic core, and measuring the thickness of thin fibrous cap. Such parameters can inform an IVUS-guided PCI strategy.

In ultrasound imaging, signal-to-noise ratio (SNR) is a crucial factor for image quality. The high attenuation of the ultrasonic signals in the tissue results in echoes from large depths buried in noise. This attenuation depends on the ultrasound frequency, and is a significant limiting factor at the high frequencies used for IVUS imaging. Moreover, the image resolution requirements stipulate the transmission of short pulses, eventuating in transmitting relatively low signal energy. Increasing the transmitted power is limited by the maximum biological exposure to acoustic intensity, and by the capability of electronics (instruments and transducer material) to handle such a high voltages.

Sophisticated signal transmission schemes have been developed in radar and mobile telecommunication systems [7], which are currently utilized in ultrasound imaging. Transmission of modulated signals, and decoding the received signal with an appropriate filter, can improve the SNR without degrading imaging resolution[8]. There are different kinds of coded signals designed to use in medical ultrasound. To date, most authors used chirp, linear frequency modulation (FM), or pseudo-chirp excitation [9–11], and others have considered binary codes [12, 13].

Phase-based binary codes like Golay and Barker codes have limited utility in ultrasound imaging, as the abrupt change in the phase of the coded signals produces high harmonics. Since any ultrasound transducer acts as a band-pass filter; thus, frequencies above the upper limit of the transducer frequency response are

poorly transmitted, leading to imperfect encoding. On the other hand, it has been shown that linear FM signals have the best and most robust features for ultrasound imaging[14]. It is demonstrated that echos from linear FM signals can be processed without any depth-dependent filter compensation to retain the quality of the decoded signals. Consequently, it makes the processing less complicated.

The signal modulation and pulse compression can be described by a single measure of a signal: the time-bandwidth product (TB). The improvement in SNR due to the using of coded signal is equal to the TB product of the transmitted signal [15]. In ultrasound imaging, the system bandwidth is determined by the ultrasound transducer; thus, increasing the duration of the transmitted signal is the only way to increase the TB product. However, longer codes increase the deaf time: time duration which transducer and/or driving electronics is not in receiving mode, which is undesirable.

Coded excitation has previously been used for IVUS imaging. Maresca et al. [16] used chirp signal to investigate the vasa vasorum. Qiu et al. [17] introduced a coded excitation based IVUS system whose operation frequency was more than 50 MHz. He showed that utilizing the modulated signal within that frequency range will improve the SNR and thus penetration depth and makes his IVUS system comparable with the costly optical imaging systems. However, the deaf time in his system was 2.5 μs or 4 mm. This needs to be improved in order to make the system pragmatically utilizable in clinical application.

To date, IVUS transducer technology is predominantly based on piezoelectric materials. The major limitation of piezoelectrics is the inherent trade-off between bandwidth and sensitivity, which eventually limits image quality, and as argued above, is of key importance for the implementation of coded excitation schemes. Capacitive Micromachined Ultrasound Transducer (CMUT) is a promising alternative to piezoelectric transducers [18]. Advantages of CMUT over piezoelectric technology are the relatively large bandwidth with comparable sensitivity [19, 20], the freedom of geometric design [21], being lead free, ease of large-scale production (in semiconductor planar processing) and miniaturization which will lower the end product cost [22–24]. CMUTs are made of thin membranes which are essentially parallel plate capacitors with a gap between the plates. The acoustic properties can be dynamically adjusted by changing the DC bias voltage [25, 26]. Depending on the applied DC voltage, a CMUT works in either conventional or collapse mode, with considerably different acoustic and received noise behavior [27, 28]. All these properties offer great benefits for catheter-based forward looking and Side Looking-IVUS (SL-IVUS) applications [29–32].

In this work, we use a custom-designed CMUT IVUS sensor to investigate phased-array IVUS imaging using modulated signals. According to the work published by Misaridis et al. [14], we chose the appropriate coded waveforms and compression filters and designed a FM based coded signal suitable for IVUS imaging. The reconstructed signal and imaging characteristics are compared to a Gaussian pulse excitation, evaluated on a wire phantom target and on an *ex vivo* coronary artery specimen.

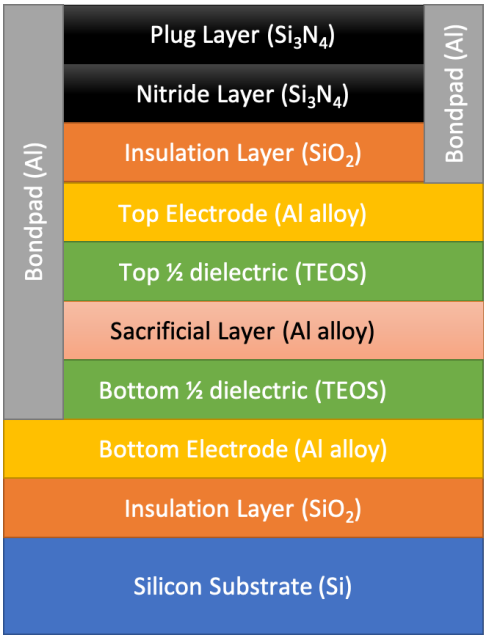


Figure 3.1: Schematic view of the fabricated CMUT layers



## 3.2. Materials and Methods

### 3.2.1. CMUT fabrication

The CMUT arrays were fabricated in a professional cleanroom facility on a 6-inch silicon wafer utilizing the standard sacrificial release process, in which the cavity underneath the membrane is created by deposition and subsequent selective etching of a sacrificial metal layer [33]. Common processing steps were used to fabricate the transducer stack: metal sputtering, primer deposition, spinning of a photoresistive layer, patterning by means of light exposure over a photolithographic mask, photoresistive layer development, wet and dry etching, photoresistive layer stripping with acetone or oxygen plasma and plasma enhanced chemical vapor deposition of the insulating layer. The final transducer stack consists of a silicon wafer covered with silicon dioxide for passivation, a bottom electrode insulated with tetraethoxysilane (TEOS), vacuum cavity created using the sacrificial release process, a TEOS insulated top metal electrode covered with silicon oxide and a nitride plug layer on the top. Apart from the plates, aluminum bond pads providing contact to the top or bottom electrodes are created on the side of the array to allow for wire bonding. More information on the patented fabrication of the CMUT can be found in [25, 34]. The complete layer stack including the layer materials is shown in Figure 3.1. The problem of charging in CMUTs are associated with charge carriers leaving from one electrode to the other. Based on this fabrication method, the isolation layers act as barriers for preventing or reducing the flow of charge carrier between the electrodes with the objective to fabricate charging-free CMUTs.

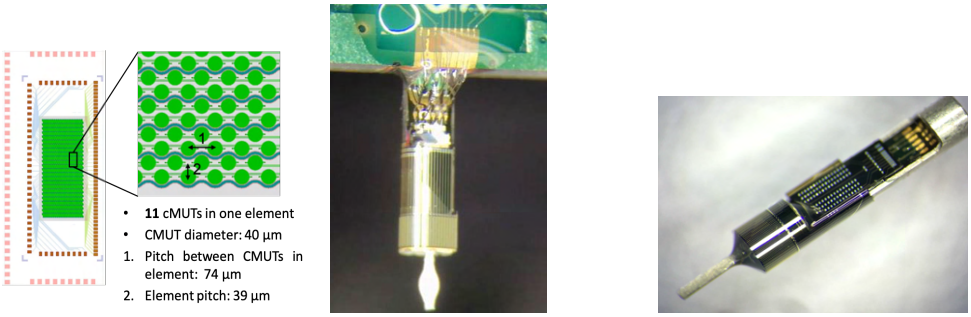


Figure 3.2: **(a)** Layout of 48-element flat CMUT array and element geometry, **(b)** The rolled up 96-element CMUT array mounted on the PCB, as used for imaging, **(c)**, The rolled-up array integrated in a catheter tip.

### 3.2.2. CMUT sensor design and assembly

A custom-designed CMUT array with 40 µm membrane diameter and 39 µm element pitch was manufactured by Philips Research. We characterized both a flat version of the 1-D CMUT array with 48 elements, and a 96-element array rolled up to catheter tip form factor. Figure 3.2a shows the schematic view of the linear CMUT array and the element geometry, consisting of 11 membranes. The same CMUT cells in a 96-element layout were wrapped around a catheter tip with 1.2 mm diameter, shown in Fig. 3.2c. The so-called Flex-to-Rigid (F2R) process allows the array to be rolled up into a cylinder shape. This enables the fabrication of arbitrary shaped silicon islands with co-integrated flexible connections including embedded flexible metal interconnects [35]. The cylindrical CMUT array was mounted on the side of a PCB for experiments.

The image sequence follows a sequential “transmit all, receive three” scheme, where the receive triplet is stepped across the array until all elements have been read out; acquisition of a full image requires 32 transmission/receive sequences. An application specific integrated circuit (ASIC) with low noise amplifier (LNA) was designed to address the elements in transmit and receive mode. In transmit mode, the ASIC allows the external AC signals to be applied to all transducer elements simultaneously. This design avoids the use of high-voltage ASIC technology and allows a more compact realization of the chip. In receive mode, the ASIC senses the echo signals of three selected transducer elements, and subsequently amplifies and buffers these signals to match the low impedance of the coax cables. The imaging fashion of excite all/receive three was stipulated by the ASIC. The LNA specifications are listed in Table 3.1. The selection of the echo signals happens by means of a shift register that serves as a state machine.

The fabricated CMUT devices and the ASIC were glued and wire-bonded to the printed circuit board (PCB) and each other. The sample was coated with a thin layer of a silicone-like material for electrical insulation of the bond pads and passivation of the CMUT cells.

A custom made electronic unit, labelled “interface box” in Fig. 3.3 (Philips Innovation Services, Eindhoven, Netherlands), was used to pass the externally generated control signals to the ASIC. These controlled switching between transmit/receive mode and selected the next triplet of CMUT elements to receive the echo signal. The interface box also provided AC and DC amplification, externally controlled Time Gain Compensation (TGC) functionality, and protective circuitry to prevent high-voltage transmission to the ASIC while in receive mode. It provides 46 to 30 dB of RF amplification (8 MHz - 40 MHz) where the frequency response of the RF amplifier was compensated for in the excitation signals. The TGC has 12 to 81 dB amplification depending on its input level (0 V - 1.1 V) over the mentioned frequencies. The interface box provides 45.9 dB DC amplification.



### 3.2.3. Characterization of the CMUT sample

The transmit impulse response of the CMUT array was measured in a water tank set-up. The PCB with the flat 48-element CMUT array was mounted on a three-axis manual translation stage, immersed in water and positioned at a distance of 3 mm from the tip of the calibrated 0.2 mm needle hydrophone (Precision Acoustics, Ltd, Dorset, UK). The CMUT array was biased at different voltages using a DC source (ADCMT; 6241A, ADC Corporation, Saitama, Japan) and was driven by a unipolar Gaussian pulse with an amplitude of 10 V and duration of 50 ns, generated by a PCI arbitrary wave generator (DA4300, Chase Scientific Co., Langley, WA, USA), input to the custom RF amplifier. The voltage signal received on the hydrophone was digitized with PCI digitizer (Razor CSE1442; GaGe, Lockport, IL, USA). The block diagram of the system is shown in Figure 3.3.

The CMUT array transmit response was measured as a function of bias voltage. The bias voltage was increased from 0 V to 30 V with step of 2.5 V. The CMUT array transitioned into collapse mode when a bias voltage of approximately 17.5 V was applied. The snap-back voltage was measured in a similar way, except with the bias voltage being reversed, The array snap-back voltage was 15 V.

The voltage signal received on the hydrophone was converted into output pressure using the hydrophone calibration data (up to 40 MHz), and corrected for the

Table 3.1: LNA Specifications

| Specification | Value | Explanation |
|---|---|---|
| Signal bandwidth | 30 MHz | AC transfer function, -3dB roll off of receive chain |
| Gain | 50 dB | LNA gain at 20 MHz with Zload = 75 Ω |
| Noise Factor | 4 dB | Noise factor at 20 MHz |
| Dynamic Range | 75 dB | Over entire bandwidth |
| Channel Cross talk | - 65 dB | Cross-talk of an unselected channel on the signal of a selected channel |

RF amplifier frequency response, as well as the sound attenuation in water. Non-linear propagation effects are neglected. The spectra of the received signals were analyzed and plotted as the frequency response of the CMUT array at different bias voltages. The center frequency, fractional bandwidth and transmit sensitivity were calculated as a function of the bias voltage.

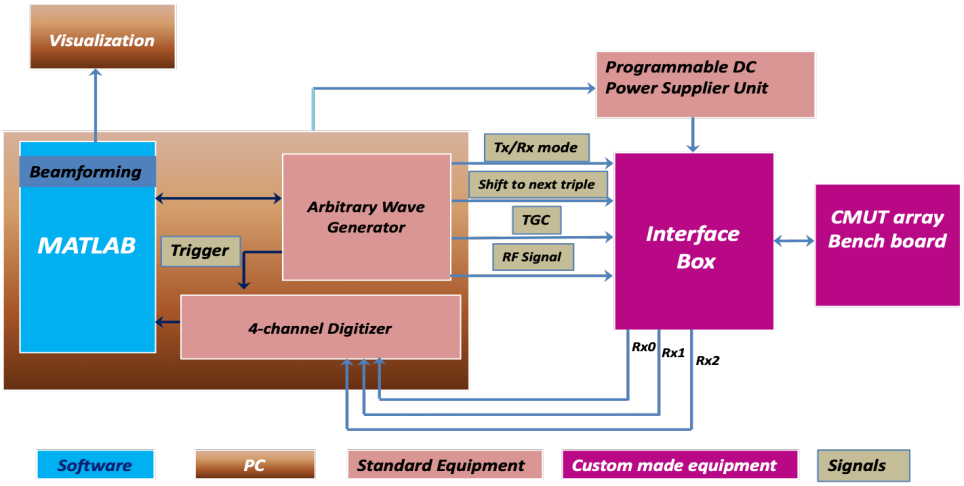


Figure 3.3: IVUS system level description. Schematic block diagram of IVUS architecture, including main interactions.

### 3.2.4. Coded Excitation

The basic principle of coded excitation and pulse compression is to convert a long frequency-modulated transmitted signal into a correlation signal with shorter time duration and a greater contrast to noise ratio. This happens by applying a matched filter, which is equal to the input waveform with reversed time axis. Therefore, if the input signal to the filter is the same as the excitation signal, the matched filter response would be mathematically equivalent to the auto-correlation of the transmitted signal. Any change, such as applying an apodization window to the match filter impulse response, makes the filter "mismatched" with the input waveform.

In the presence of frequency dependent attenuation, linear frequency modulated (LFM) or chirp signals have the most robust performance in terms of SNR improvement [14]. The chirp signal may be formulated as:

$$s(t) = A\cos\left(2\pi\left(f_c.t + \frac{B}{2T}t^2\right) + \Phi_c\right), \tag{3.1}$$

where $0 < t < T$, $f_c$ is the starting frequency, $B$ is the chirp bandwidth and $\Phi_c$ is the starting phase. Based on the theory of the code compression, the expected gain in SNR is equal to the time-bandwidth product.

$$GSNR = T \times B \tag{3.2}$$

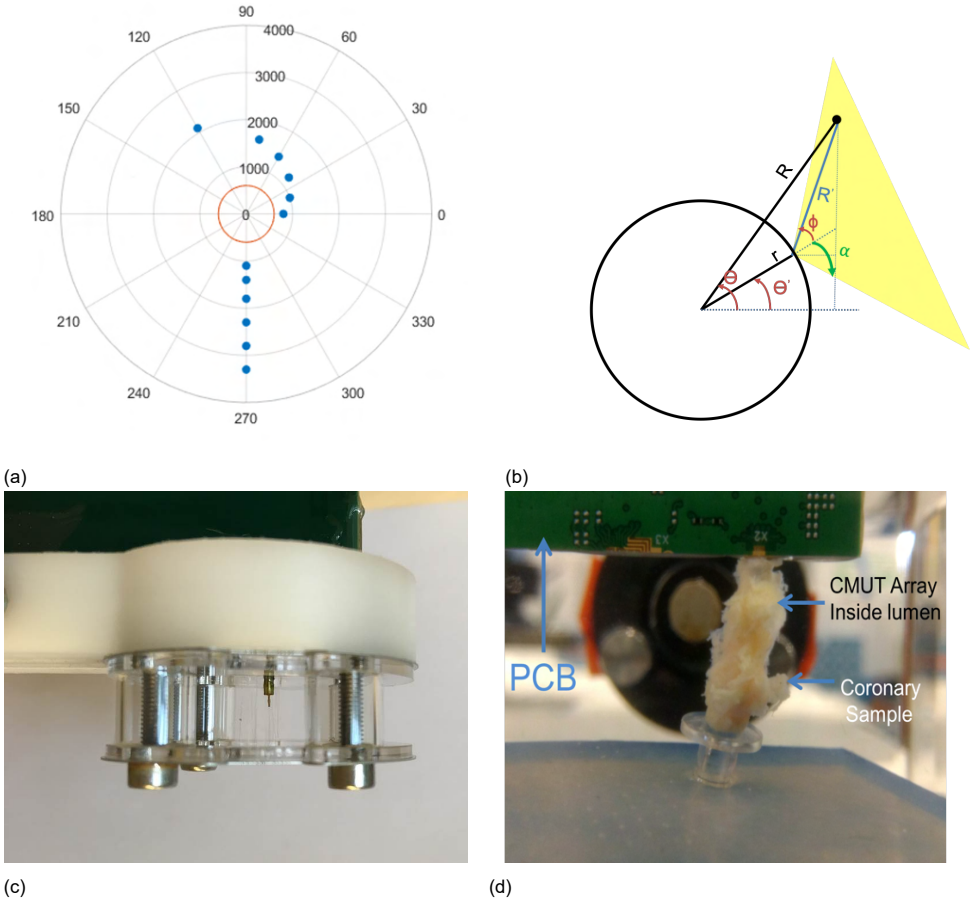


Figure 3.4: **(a)** Schematic top view of the wire positions inside the phantom, **(b)** angular response from an individual array elements, **(c)** Rolled-up imaging core inside custom developed wire phantom. **(d)** Rolled-up imaging core inside an autopsy human coronary artery specimen

### 3.2.5. Wire phantom imaging

A wire phantom was designed to quantitatively evaluate the imaging resolution and depth of the rolled-up array. Figure 3.4a shows a top view of the wire positions inside the phantom. The tungsten wire diameter was 15 µm. The wire-phantom was mounted on the side of the PCB, such that the catheter tip is centered in the phantom. The complete assembly was immersed in water (Figure 3.4c). We beam-formed all RF-lines acquired from the 96 elements in the GPU. Imaging performance was quantified in terms of the SNR and resolution, comparing images formed by a Gaussian short-pulse excitation and the compressed chirp.

### 3.2.6. IVUS Beamforming

In conventional dynamic focusing, the image is created line-by-line using a fixed transmit focus and a dynamic delay-and-sum receive focus which is then scan-converted to create virtual lines, to be interpolated in between the actual lines. In the approach we adopt here, a pixel based beam-forming scheme improves spatial resolution by lowering the interpolation artifacts. In this method, we assumed a virtual source behind the elements, at the center of the catheter, producing cylindrical waves. This is plausible since all elements fire simultaneously.



For SL-IVUS imaging, a dense circular array of 96 elements was modeled for beam-forming. The elements were equally spaced around the circumference of the catheter at an element pitch of about half wavelength at the fundamental operation frequency of 20 MHz.

It is important to characterize the overall receiving aperture based on the contribution of the echo signal coming from a single fixed scatterer. Figure 3.4b depicts the parameters that affect the receive aperture. Knowing the angular response of the elements, we can attribute all the pixels within the region in which the echo signals are received (highlighted area) by each element.

$$R' = \sqrt{\left(R\cos(\theta) - r\cos(\theta')\right)^2 + \left(R\sin(\theta) - r\sin(\theta')\right)^2} \tag{3.3}$$

$$\varphi = \arctan\left[\frac{R\sin(\theta) - r\sin(\theta')}{R\cos(\theta) - r\cos(\theta')}\right] - \theta' \tag{3.4}$$

In (3.3), $R$ is the radial position of the reconstructed pixel (scatterer), $R'$ is the distance between the pixel and the element, $r$ is the position of the element, $\theta$ is the angle of the pixel from the horizontal and $\theta'$ is the angular position of the element. $\varphi$ in (3.4) is the angle with respect to the normal at an individual element.

Using these distances, we calculated the propagation delay from the virtual source in the center of the catheter, to the scattering position $(i,j)$ and back to the receiving element. We furthermore defined a mask $A$ which rejects pixels outside the opening angle $\alpha = 50°$ (relative to the element normal). The resulting image amplitude $S(i,j)$ was then computed by a straightforward delay-and-sum approach:

$$\begin{aligned} t_n(i,j) &= \frac{R(i,j) + R_n'(i,j)}{c} \\ A_n(i,j) &= \begin{cases} 1; \left|\varphi_n(i,j)\right| \leqslant \alpha \\ 0; \left|\varphi_n(i,j)\right| > \alpha \end{cases} \\ S(i,j) &= \sum_{n=1}^{96} S_n\left(t_n(i,j)\right) \times A_n(i,j) \end{aligned} \tag{3.5}$$

In (3.5), $t_n(i,j)$ is the calculated propagation time from each pixel to the element $n$; $S_n$ are the received element waveforms. In coded excitation imaging, $S_n$ are the traces after filter compression. Based on these equations, we implemented

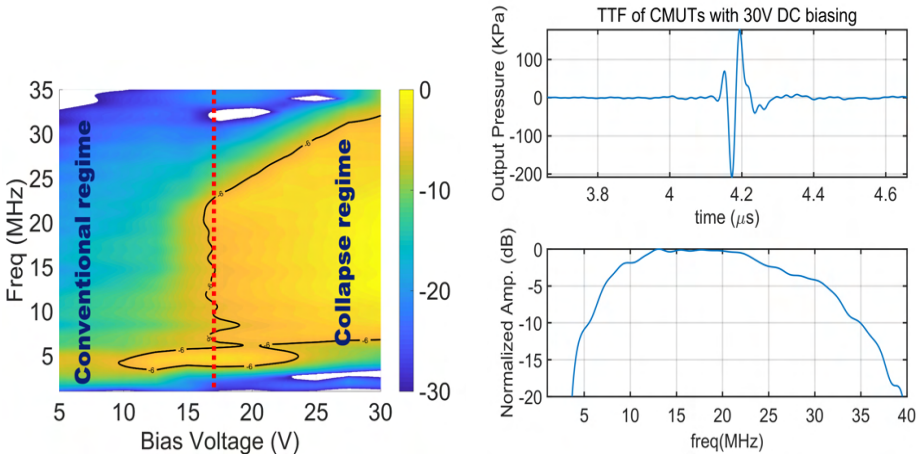


(a) (b)

Figure 3.5: **(a)** Transmit Transfer Function of 48 elements CMUT array as a function of biasing voltage, **(b)** Transmit transfer function and Sensitivity of CMUT array at 30 V DC biasing.

pixel-based beam-forming scheme with a grid spacing of 5μm over a 2D space of $1\text{cm} \times 1\text{cm}$.

### 3.2.7. Autopsy tissue experiments

A coronary artery was harvested during autopsy at the Dept. of Pathology of the Erasmus MC, under a protocol sanctioned by the local ethics board. A short section of artery was mounted in the water tank and imaged using the rolled-up IVUS device. The coronary artery was immersed in Phosphate-buffered saline PBS(1X) for imaging (Figure 3.4d). The diameter of the artery was approximately 2 mm.

After IVUS experiments, the tissue was fixed for 24 hours in formalin and subsequently processed. A series of 5 sections, each 5 μm thick, were taken at locations every 250 μm to gain insight into the tissue appearance in the vicinity of the imaging plane. At each location, one slide underwent routine hematoxylin/eosin (HE) and Oil Red O (ORO) staining.

## 3.3. Results

### 3.3.1. Characterization of the CMUT sample

Figure 3.5a shows the Transmit Transfer Function (TTF) of the 48-element CMUT array at varying bias voltage. The spectra of the received signals are Fourier transformed to obtain the frequency response and normalized to the maximum value among all measurements. The maximum transmit sensitivity is observed at an applied bias voltage of 30 V, at which the CMUT resonates at center frequency of 19.5 MHz. The -6dB contour plot at Figure 3.5a illustrates that the array is wide-band

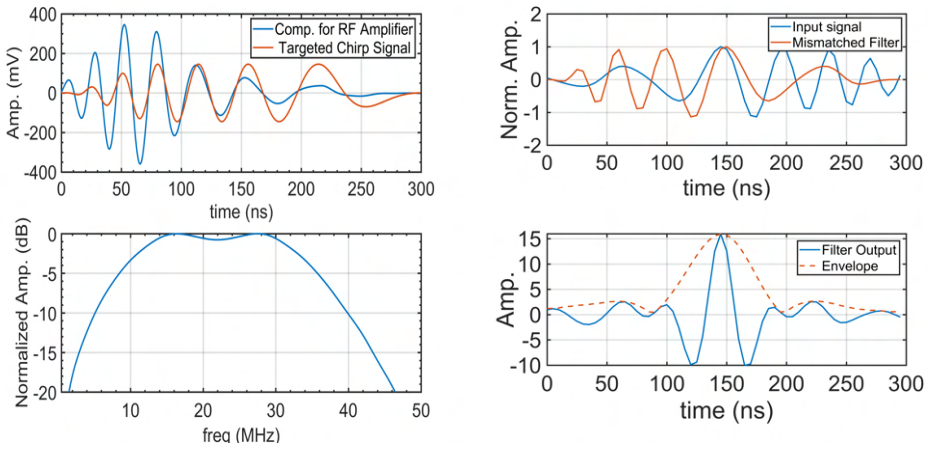


(a) (b)

Figure 3.6: **(a)** Designed chirp signal and its compensation for the frequency dependant RF amplifier, **(b)** received signal and its mismatch filter response.

after collapsing which happens at 17.5 V DC biasing.

The center frequency, fractional bandwidth and transmit sensitivity are calculated at each bias voltage. Figure 3.5b shows that the array provides approximately 400 kPa output pressure when it is biased at 30 V DC. This translates to a transmit sensitivity of 36.8 kPa/v with 130% fractional bandwidth at a center frequency of 19.5 MHz. For all subsequent imaging experiments, we adopted a bias voltage of 30 V.

Applying a bias voltage of 30 V, we quantified the transmitted pressure from the rolled-up array, which emits a cylindrical wave instead of a plane one. We found a transmit sensitivity of 7.8 kPa/V, recorded at the same delay of 4.2 μs.

### 3.3.2. Coded Excitation

Based on the characterization result of the CMUT sample, we designed a LFM signal with center frequency, $f_c = 22.4$ MHz, and 100% fractional bandwidth ($B = 22.4$ MHz). The LFM signal had a duration of $T = 300$ ns to meet the requirement of $< 0.5$ mm deaf-time for IVUS application. A Tukey tapered cosine window of 50% was applied to the LFM. The waveform amplitude was modulated to compensate for the frequency response of the RF amplifier (the blue line in Fig. 3.6a). The amplified chirp signal had the desired shape and frequency response, as depicted in Fig. 3.6a. Once the chirp is applied to the CMUT array, the impulse response of the CMUT again changes the waveform.

The received echo signal was considered as the input signal to the mismatched filter. Figure 3.6b illustrates the received signal from the wire and its complex conjugate, which was used as the mismatched filter response characteristic. The bottom part of Fig. 3.6b shows the output of the mismatched filter and its envelope. The

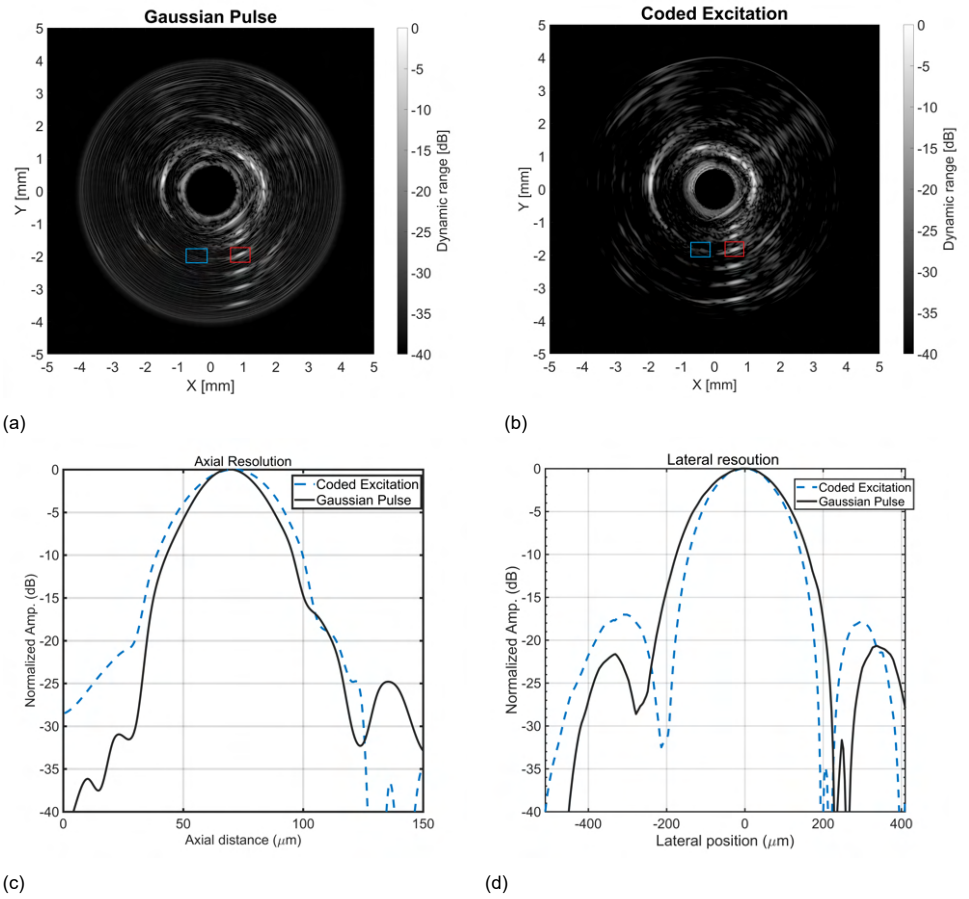


Figure 3.7: Wire phantom image reconstruction using the short pulse **(a)** and the chirp signal **(b)** for the rolled-up CMUT array, **(c,d)** 60 μm Axial resolution and 270 μm lateral resolution achieved using the short pulse (solid line) are compared with 70 μm axial and 245 μm lateral resolution achieved using the chirp signal.

width of the peak of the decoded signal envelope determines the resolution. The time-bandwidth product of the designed chirp signal was $T \times B = 6.7$ and based on the theory, we expect to gain 8.3 dB in SNR.

### 3.3.3. Imaging the wire phantom

The designed chirp signal was applied for imaging the wire phantom, compared to the short pulse for reference. Figure 3.7a and Figure 3.7b correspond to the beamformed wire phantom image reconstruction of the Gaussian pulse and coded signal, respectively. The visual appearance of the pulsed and the coded images is similar. Quantitative evaluation of the image resolution was performed by making measurements in two perpendicular cross-sections through the reconstructed

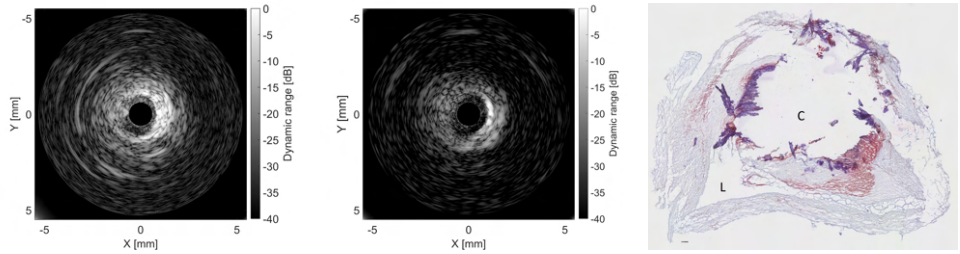


(a) (b) (c)

Figure 3.8: Ex-vivo human coronary artery image reconstruction using the short pulse **(a)** and the chirp signal **(b)** by the rolled-up CMUT array. **(c)** is the histology image of the coronary sample. The scale bar is 100 μm

wire reflections, shown in Figure 3.7c and Figure 3.7d. The -6 dB axial and lateral resolutions of the short pulse and the coded excitation were found to be 60 μm, 70 μm and 270 μm, 245 μm respectively, measured at a distance of 1.55 mm from the center of the catheter.

For the SNR calculation, we computed the ratio between the signal amplitude of a bright wire reflection (the red boxes in Figure 3.7a and Figure 3.7b) and the average amplitude in an area with only noise (blue boxes). We found an SNR of 32 dB for the short pulse image and 40 dB for the coded excitation image, confirming the 8 dB gain in SNR.

Pixel-based beamforming of the data was implemented in Matlab, achieving real-time acquisition and image formation at a maximum frame rate of 20 frames per second.

### 3.3.4. Ex-vivo imaging of the human coronary artery

We used the water tank set-up for real-time ex-vivo imaging the human coronary artery. We inserted the rolled-up array inside the lumen which was immersed in PBS. The designed chirp signal and the short pulse were used for imaging. Figure 3.8a shows a frame from the real-time IVUS images obtained using the short pulse with dynamic range of 40 dB and Figure 3.8b are corresponding to the IVUS images obtained by the chirp signal with dynamic range of 40 dB. Figure 3.8c shows the ORO histology image of the coronary sample where a big calcified region has been found.

## 3.4. Discussion and conclusion

This work focuses on the utilization of excitation codes for CMUT based IVUS imaging. A state of the art CMUT array with 96 elements was fabricated and deployed for imaging.

We designed a linear frequency modulation (chirp) signal to improve signal to noise ratio while preserving resolution by a mismatched filter reconstruction. This method maximizes the combined use of the available bandwidth and transmission

power. It can potentially improve the SNR and thus, the penetration depth of high-resolution IVUS. The device has a -6dB device bandwidth at 30 V DC biasing of 25 MHz with 20 MHz center frequency and a transmit sensitivity of 27 kPa/V at that frequency.The chirp signal has 300 ns excitation time to meet the deaf-time requirement (less than 0.5 mm) for IVUS imaging. We imaged a wire phantom and a human coronary artery. By assessing the image quality of the reconstructed wire phantom image, we achieve 60 μm and 70 μm axial resolution using the short pulse and coded signal, respectively. We showed that coded excitation improves SNR by 8 dB, at a cost of a slightly degraded axial resolution. This is due to the windowing/apodization which is used to lower the side-lobes associated with decoding the signal, reducing the effective bandwidth. However, it is sufficient for IVUS application. The imaging scheme that transmits on all elements and detects on consecutive triplets is potentially suboptimal. Selective excitation of transmission elements could potentially improve the lateral resolution in the images, but was not supported by the electronics.



We developed and demonstrated a system that provides 20 frame per second, real-time and pixel-based beamformed phased-array IVUS images and demonstrated the feasibility of intravascular ultrasound chirp imaging of human coronary atherosclerosis using the CMUT array. Features like a large calcification could be identified in both short-pulse and compressed-chirp imaging. Exact colocation of the imaged sections was challenging, which complicates a direct comparison of the two methods in imaging this very heterogeneous tissue.

We presented a novel concept for IVUS based on broadband CMUT. We characterized the array performance for coded excitation imaging which may be useful for achieving greater penetration depth in IVUS while maintaining image resolution. CMUTs are manufactured using micromachining techniques which are evolved from the well-established integrated circuit fabrication process and possess unique potential in high yield mass production of CMUT-based IVUS catheters. Consequently, this technique offers an opportunity to lower the production costs. Future realizations may feature a higher frequency, compact and versatile transmit/receive electronics and dedicated image processing software for further improvements to image quality.

## Acknowledgment

This work was done in the frame of the ENIAC INCITE project No. 621278. INCITE is an ENIAC JU project and is co-funded by grants from the Netherlands, Finland, Hungary, France, Ireland, Sweden, Spain, and Poland. The authors thank Dr. Deep Bera for his support in beam-forming and Matthijs Stam BSc for preparing histology.

# References

[1] R. Pakdaman Zangabad, J. G. Bosch, F. Mastik, R. H.S.H. Beurskens, V. A. Henneken, J. W. Weekamp, A. F. W. van der Steen, and G. van Soest, *Real-time coded excitation imaging using a cmut-based side looking array for intravascular ultrasound,* IEEE Transactions on Ultrasonics, Ferroelectrics, and Frequency Control (2021), 10.1109/TUFFC.2021.3054971.

[2] E. Wilkins, L. Wilson, K. Wickramasinghe, P. Bhatnagar, J. Leal, R. Luengo-Fernandez, R. Burns, M. Rayner, and N. Townsend, *European Cardiovascular Disease Statistics 2017* (European Heart Network, Belgium, 2017).

[3] R. Ross, *The pathogenesis of atherosclerosis: a perspective for the 1990s,* Nature **362**, 801 (1993).

[4] A. F. W. van der Steen, R. A. Baldewsing, F. L. Değertekin, S. Emelianov, M. E. Frijlink, Y. Furukawa, D. Goertz, M. Karaman, P. T. Khuri-Yakub, K. Kim, *et al.*, *Ivus beyond the horizon.* EuroIntervention: journal of EuroPCR in collaboration with the Working Group on Interventional Cardiology of the European Society of Cardiology **2**, 132 (2006).

[5] S.-J. Hong, B.-K. Kim, D.-H. Shin, C.-M. Nam, J.-S. Kim, Y.-G. Ko, D. Choi, T.-S. Kang, W.-C. Kang, A.-Y. Her, Y. H. Kim, S.-H. Hur, B.-K. Hong, H. Kwon, Y. Jang, M.-K. Hong, and for the IVUS-XPL Investigators, *Effect of Intravascular Ultrasound–Guided vs Angiography-Guided Everolimus-Eluting Stent Implantation: The IVUS-XPL Randomized Clinical TrialIntravascular Ultrasound–Guided Drug-Eluting Stent ImplantationIntravascular Ultrasound–Guided Drug-Eluting Stent Implantation,* JAMA **314**, 2155 (2015).

[6] C. di Mario, K. C. Koskinas, and L. Räber, *Clinical benefit of ivus guidance for coronary stenting,* Journal of the American College of Cardiology **72**, 3138 (2018), http://www.onlinejacc.org/content/72/24/3138.full.pdf .

[7] Y. Takeuchi, *An investigation of a spread energy method for medical ultrasound systems: Part one: Theory and investigation,* Ultrasonics **17**, 175 (1979).

[8] M. O'Donnell, *Coded excitation system for improving the penetration of real-time phased-array imaging systems,* IEEE transactions on ultrasonics, ferroelectrics, and frequency control **39**, 341 (1992).

[9] P.-C. Li, E. Ebbini, and M. O'Donnell, *A new filter design technique for coded excitation systems,* IEEE transactions on ultrasonics, ferroelectrics, and frequency control **39**, 693 (1992).

[10] M. Pollakowski and H. Ermert, *Chirp signal matching and signal power optimization in pulse-echo mode ultrasonic nondestructive testing,* IEEE transactions on ultrasonics, ferroelectrics, and frequency control **41**, 655 (1994).

[11] N. Rao, *Investigation of a pulse compression technique for medical ultrasound: A simulation study,* Medical and Biological Engineering and Computing **32**, 181 (1994).

[12] J. Shen and E. S. Ebbini, *A new coded-excitation ultrasound imaging system. i. basic principles,* IEEE transactions on ultrasonics, ferroelectrics, and frequency control **43**, 131 (1996).

[13] R. Kažys, L. Svilainis, and L. Mažeika, *Application of orthogonal ultrasonic signals and binaural processing for imaging of the environment,* Ultrasonics **38**, 171 (2000).

[14] T. Misaridis and J. A. Jensen, *Use of modulated excitation signals in medical ultrasound. part i: Basic concepts and expected benefits,* IEEE transactions on ultrasonics, ferroelectrics, and frequency control **52**, 177 (2005).

[15] T. Misaridis and J. A. Jensen, *Use of modulated excitation signals in medical ultrasound. part ii: design and performance for medical imaging applications,* IEEE Transactions on Ultrasonics, Ferroelectrics, and Frequency Control **52**, 192 (2005).

[16] D. Maresca, K. Jansen, G. Renaud, G. van Soest, X. Li, Q. Zhou, N. de Jong, K. K. Shung, and A. F. W. van der Steen, *Intravascular ultrasound chirp imaging,* Applied Physics Letters **100**, 043703 (2012).

[17] W. Qiu, X. Wang, Y. Chen, Q. Fu, M. Su, L. Zhang, J. Xia, J. Dai, Y. Zhang, and H. Zheng, *Modulated excitation imaging system for intravascular ultrasound,* IEEE Transactions on Biomedical Engineering **64**, 1935 (2017).

[18] B. T. Khuri-Yakub, F. Degertekin, X.-C. Jin, S. Calmes, I. Ladabaum, S. Hansen, and X. Zhang, *Silicon micromachined ultrasonic transducers,* in *1998 IEEE Ultrasonics Symposium. Proceedings (Cat. No. 98CH36102)*, Vol. 2 (IEEE, 1998) pp. 985–991.

[19] Ö. Oralkan, B. Bayram, G. G. Yaralıoğlu, A. S. Ergun, M. Kupnik, D. T. Yeh, I. O. Wygant, and B. T. Khuri-Yakub, *Experimental characterization of collapse-mode cmut operation,* ieee transactions on ultrasonics, ferroelectrics, and frequency control **53**, 1513 (2006).

[20] K. K. Park, Ö. Oralkan, and B. T. Khuri-Yakub, *A comparison between conventional and collapse-mode capacitive micromachined ultrasonic transducers in 10-mhz 1-d arrays,* IEEE transactions on ultrasonics, ferroelectrics, and frequency control **60**, 1245 (2013).

[21] F. Y. Yamaner, S. Olcum, A. Bozkurt, H. Köymen, and A. Atalar, *Optimizing cmut geometry for high power,* in *2010 IEEE International Ultrasonics Symposium*, IEEE (IEEE, 2010) pp. 2247–2250.

[22] D. T. Yeh, Ö. Oralkan, I. O. Wygant, M. O'Donnell, and B. T. Khuri-Yakub, *3-d ultrasound imaging using a forward-looking cmut ring array for intravascular/intracardiac applications,* IEEE transactions on ultrasonics, ferroelectrics, and frequency control **53**, 1202 (2006).

[23] A. S. Savoia, G. Caliano, and M. Pappalardo, *A cmut probe for medical ultrasonography: From microfabrication to system integration,* IEEE transactions on ultrasonics, ferroelectrics, and frequency control **59**, 1127 (2012).

[24] A. Caronti, G. Caliano, R. Carotenuto, A. Savoia, M. Pappalardo, E. Cianci, and V. Foglietti, *Capacitive micromachined ultrasonic transducer (cmut) arrays for medical imaging,* Microelectronics Journal **37**, 770 (2006).

[25] M. Pekař, W. U. Dittmer, N. Mihajlović, G. van Soest, and N. de Jong, *Frequency tuning of collapse-mode capacitive micromachined ultrasonic transducer,* Ultrasonics **74**, 144 (2017).

[26] M. Pekař, A. F. Kolen, H. Belt, F. van Heesch, N. Mihajlović, I. E. Hoefer, T. Szili-Török, H. J. Vos, J. G. Bosch, G. van Soest, and A. F. W. van der Steen, *Preclinical testing of frequency-tunable capacitive micromachined ultrasonic transducer probe prototypes,* Ultrasound in medicine & biology **43**, 2079 (2017).

[27] S. Olcum, F. Y. Yamaner, A. Bozkurt, and A. Atalar, *Deep-collapse operation of capacitive micromachined ultrasonic transducers,* IEEE transactions on ultrasonics, ferroelectrics, and frequency control **58**, 2475 (2011).

[28] R. Pakdaman Zangabad, A. Bozkurt, and G. Yaralıoğlu, *Signal to noise ratio optimization for a cmut based medical ultrasound imaging system,* in *2015 IEEE International Ultrasonics Symposium (IUS)*, IEEE (IEEE, 2015) pp. 1–4.

[29] F. L. Değertekin, R. O. Güldiken, and M. Karaman, *Annular-ring cmut arrays for forward-looking ivus: Transducer characterization and imaging,* IEEE transactions on ultrasonics, ferroelectrics, and frequency control **53**, 474 (2006).

[30] J. Zahorian, M. Hochman, T. Xu, S. Satir, G. Gurun, M. Karaman, and F. L. Degertekin, *Monolithic cmut-on-cmos integration for intravascular ultrasound applications,* IEEE transactions on ultrasonics, ferroelectrics, and frequency control **58**, 2659 (2011).

[31] G. Gurun, C. Tekes, J. Zahorian, T. Xu, S. Satir, M. Karaman, J. Hasler, and F. L. Degertekin, *Single-chip cmut-on-cmos front-end system for real-time volumetric ivus and ice imaging,* IEEE transactions on ultrasonics, ferroelectrics, and frequency control **61**, 239 (2014).

[32] A. Şişman, J. Zahorian, G. Ö. Gürün, M. Karaman, M. Balantekin, F. L. Değertekin, and P. Hasler, *Evaluation of cmut annular arrays for side-looking ivus,* in *2009 IEEE International Ultrasonics Symposium* (IEEE, 2009) pp. 988–991.

[33] A. S. Ergun, G. G. Yaralıoğlu, and B. T. Khuri-Yakub, *Capacitive micromachined ultrasonic transducers: Theory and technology,* Journal of aerospace engineering **16**, 76 (2003).

[34] J. H. Klootwijk, P. Dirksen, M. Mulder, and E. M. Moonen, *Capacitive micromachine ultrasound transducer,* (2015), uS Patent 9,132,693.

[35] B. Mimoun, V. Henneken, A. van der Horst, and R. Dekker, *Flex-to-rigid (f2r): A generic platform for the fabrication and assembly of flexible sensors for minimally invasive instruments,* IEEE Sensors Journal **13**, 3873 (2013).

# 4

# A kerfless PVDF Array for Photoacoustic Imaging

**Reza Pakdaman Zangabad,** Geert Springeling
Emile Noothout, Robert H.S.H. Beurskens, Nico de Jong
Antonius F. W. van der Steen, Gijs van Soest, Verya Daeichin

This chapter has been published in proceeding of 2018 IEEE International Ultrasonics Symposium (IUS) [1].

*Photoacoustic signals can have very large bandwidth and large dynamic range. With appropriate electrical impedance matching, off-resonance PVDF transducers offer the bandwidth and sensitivity to fully capture these signals. Minimizing pitch and kerf in ultrasound transducer to improve lateral resolution is of great importance. Kerfless arrays, where the electrodes are patterned onto the piezoelectric material, fulfill such a demand and are simpler to manufacture. We have manufactured and characterized a kerfless off resonance PVDF array of 10 elements with dimensions of 1 mm × 1.5 mm × 28 µm (w×h×t) both numerically and experimentally for PA imaging. We matched the high impedance of the PVDF elements with low impedance of acquisition system through an appropriate LNA (26 dB amplification over 10 MHz BW). PA signals from a tungsten wire with a diameter of 35 µm were received with our device, and compared to those recorded with a 0.2 mm needle hydrophone. Based on simulation and measurement results, the phase change in the off-resonance PVDF is negligible. The crosstalk between adjacent elements is -30dB. We measured a sensitivity for our array of about 1.38 µV/Pa at 3 MHz. The RMS output noise level is 240 µV over the entire bandwidth (10Hz - 10 MHz).*

## 4.1. Introduction

Photoacoustic imaging (PAI) is an emerging, nonionizing imaging modality for preclinical and clinical applications. Photoacoustic signal can be generated using a short pulse laser that illuminates a tissue which absorbs the light energy and converts the light to heat. The energy absorption induces rapid adiabatic thermoelastic expansion which generates pressure waves. These pressure waves propagate through the surrounding medium and can be received by ultrasound transducers [2]. The PAI technique has been widely developed and has application in photoacoustic tomography where an ultrasound array enclosing the tissue and a relatively large laser beam irradiates the object [3], photoacoustic microscopy [4, 5] where a focused light source and focused ultrasound receiver array scans the object, and photoacoustic endoscopy [6].



Because of the broadband nature of the PA signal, transducers with high bandwidth can significantly improve the sensitivity of the PAI [7]. The Lead Zirconate Titanate (PZT) based ultrasound transducers offering high transmit/receive efficiency and provide capability for dual modal PA/US imaging. However, the $70-80\%$ transducer fractional bandwidth is a limiting factor in getting high resolution PA images with high sensitivity. Ultrasound transducers based on polyvinylidene diflouride (PVDF), and Capacitive Micromachined Ultrasound Transducer (CMUT) technologies have also been explored for PA imaging [8, 9]. CMUT devices provide more bandwidth than PZT, at similar receive efficiency, but the dielectric charging effect and thus, the reliability and life time are challenging issues [10]. PVDF based ultrasound transducer has the highest bandwidth and also provides more receive efficiency than PZT which makes it an ideal candidate to be used in this application, but its transmit efficiency is low in comparison with other transducer [11].

The elements in transducer arrays are created using dicing method in the bulk piezoelectric ceramics slab. Kerfs, which are the spaces between elements, provide isolation between adjacent elements that can prevent electrical and mechanical coupling, or crosstalk. It has been shown that the mutual coupling between elements is the main reason for degradation of the array bandwidth and consequently, the image quality of ultrasound B-mode imaging [12–14]. In order to obtain a good lateral resolution, the element pitch size should be smaller than the wavelength and the kerf between two adjacent elements has to be as small as possible. Unfortunately, the dicing procedure can be difficult and challenging in terms of cost, yield and limitations on fine-scale dimensions, especially for high frequency arrays [15]. This issue becomes more challenging for 3D imaging where 2D arrays with very high number of elements are required [16].

An alternative and simpler manufacturing approach is to make kerfless transducer where electrodes are patterned to define the transducer elements. This technique permits the development of high frequency transducers [17, 18] and helped researchers to develop dual layer transducer for high frame rate [19] and 3D imaging [20]. The major drawback in this technique is the increased crosstalk. Efforts to minimize the coupling have included the use of screen-printed PZT thick films, where the kerfless design does not necessarily lead to compromised array performance. The anisotropic nature of screen-printed PZT films introduces a large dif-

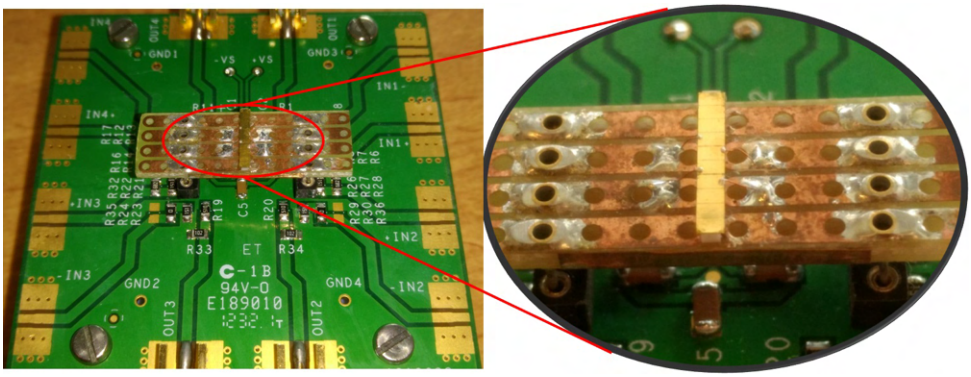


Figure 4.1: The read out circuit with 4 LNAs (left side) where the 28 µm-thick PVDF array (right side) is directly connected to it using a PCB board.

ference in the electromechanical coupling between thickness and lateral modes, which suppresses crosstalk [21].

In order to gain maximum transmit/receive efficiency in ultrasound transducers, the thickness of the PZT material is tuned such that the transducer element is at resonance for the frequency of interest. This choice maximizes the sensitivity of the transducer. A downside of this approach is the resulting complexity of the read-out circuits, since the transducer phase change at the resonance has to be taken in to account and accordingly compensated.

Since most of the PA signal energy of human plaque is below 10MHZ [7]; in this paper, we realized an off-resonance PVDF based transducer for PAI of human carotid plaque. Because the array will be used in receive-only mode, we chose the resonance frequency of the PVDF to be very high (45 MHz) and consequently, the phase change at lower frequency ranges ($\leq$ 10 MHz) would be negligible.

## 4.2. Materials and Methods

A 28 µm-thick uniaxial poled PVDF film with gold electrodes(Precision Acoustics, Ltd, Dorset, UK) was cut in a rectangular shape of $10\text{mm} \times 1.5\text{mm}$ using a laser micromachining workstation (FemtoLAB, Workshop of Photonics, Vilnius, Lithuania). This slab is glued on a 1mm thickness quartz substrate which is also acting as a backing layer and then the top electrode of the PVDF slab is laser cut to define a kerfless array of 10 elements with 1 mm element width.

A laser source (Innolas Spitlight EVO OPO, Krailling, Germany) of 800 nm wavelength, 4 mJ pulse energy, and 200Hz PRF illuminated a tungsten wire with a diameter of 35 µm for generating the PA signal. The sensitivity and receive transfer function of the prototype PVDF element, integrated with the LNA, have been evaluated in Galden liquid (HT135) in order to prevent electrical short circuit. The signals from our array were compared with a 0.2 mm needle hydrophone (Precision Acoustics, Ltd, Dorset, UK) which was immersed in water. Electrical impedance mea-

surements were performed using vector impedance meter (HP 4193A, USA) for all of the connected elements and good reproducibility was observed on capacitance distribution with a relative variation less than 4%.

In order to match the high impedance of the PVDF elements ($\leq 5pF/mm^2$) with low impedance of acquisition system, we used an appropriate Low noise amplifier (LNA) (ADA4807-4, Analog Device Inc., Norwood, MA, USA) with 200MHz gain bandwidth product and $3.1nV/\sqrt{Hz}$ noise density. Since most of the PA signal energy is in the range of less than 10 MHz; we tuned the LNAs to have 10MHz bandwidth and consequently, 26dB amplification ratio. A short wire ($\sim$ 3 mm) was glued to each element and connected to a PCB where the LNAs were placed (Figure 4.1).

We also analyzed the crosstalk in the kerfless array both experimentally and numerically. In finite element analysis (Comsol Multiphysics 5.3a), one element of the PVDF array is excited with one cycle sinusoidal waveform with frequency of 6 MHz providing 100% fractional bandwidth and recorded the generated voltage level at the adjacent elements. The same method was implemented experimentally where a pulse with frequency of 6 MHz and 400 V (5077PR, Panametric Ltd., square-wave Pulser/Receiver) is applied to one of the PVDF element and crosstalk at the neighboring elements are recorded.



## 4.3. Results

3-D Finite Element Analysis (FEA) was carried out using COMSOL Multiphysics 3.5a for characterizing the immersed kerfless PVDF array. A Perfectly Matched Layer (PML) is used as an absorbing boundary which is located $2\lambda_0$ away of surface of the array at the lowest frequency and the model is simplified by simulating a portion of the array with appropriate symmetry boundaries. Furthermore, the domain mesh size is set to the minimum acceptable size of $\lambda_1/10$ at the highest operating frequency.

The input impedance of the PVDF element was measured and compared with the FEM result. Figure 4.2 shows the high input impedance of the PVDF element and also indicates that the phase change in the element over the entire frequency is negligible confirming that the PVDF is in the off-resonance regime for the frequencies up to 10 MHz. The high impedance of the transducer elements are matched to the high input impedance of the Operational Amplifiers (OpAmps). Furthermore, for cable matching, the output impedance of the OpAmps are matched to $50\Omega$.

Figure 4.3 depicts the received PA signal in time and frequency domains using our array. Notice that the dip at 1.45 MHz is due to the suboptimal backing of the array. Considering the speed of sound in quartz ($\sim$ 5800 m/s) and the 1.45 MHz dip in the frequency response of the PVDF element, its related wavelength is 4 mm. The quartz layer's thickness (1 mm) would be corresponding to quarter wavelength in that frequency, leading to destructive interference from a round-trip reflected wave and narrowing the bandwidth.

The same PA source was used to detect the signal with the 0.2 mm hydrophone and the result is provided in the Figure 4.4. We calibrated the PVDF element response with the hydrophone and demonstrated that our device provides an output voltage with a sensitivity of about 1.38 $\mu V/Pa$ at 3 MHz. The RMS output noise level

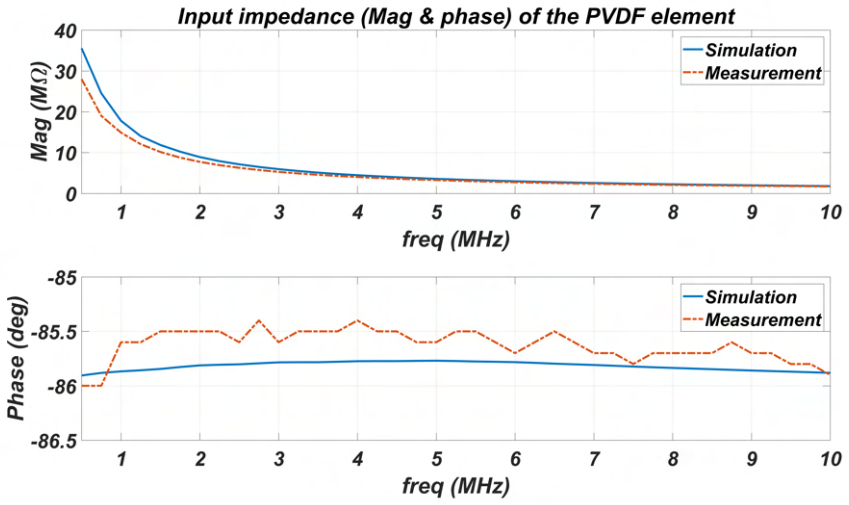


Figure 4.2: Input electrical impedance of the PVDF element in air as function of frequency.

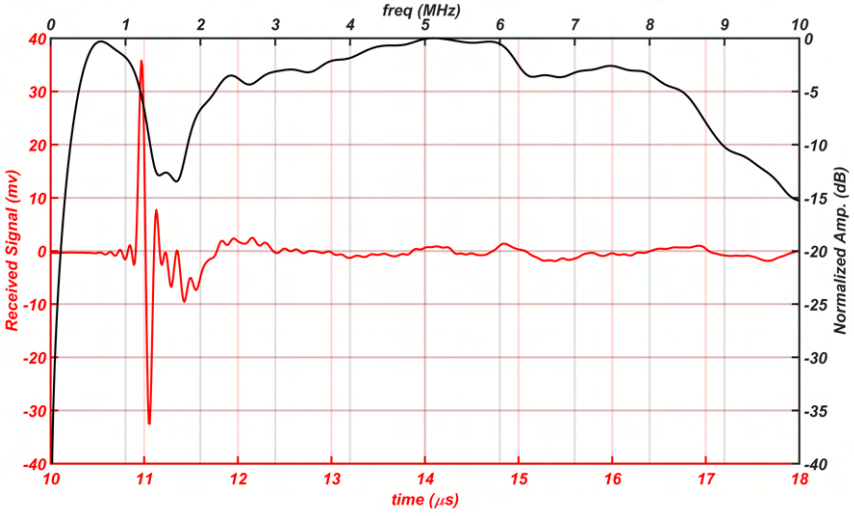


Figure 4.3: Photoacoustic signal received by the PVDF element and its frequency response.

is 240 μV over the entire bandwidth (10Hz - 10 MHz). This indicates that the minimum detectable pressure for our system is 170 Pa. This will be further improved if we use an LNA with more gain.

We also analyzed the crosstalk in the kerfless array both experimentally and numerically. Figure 4.5 shows that the crosstalk level at the adjacent element is at

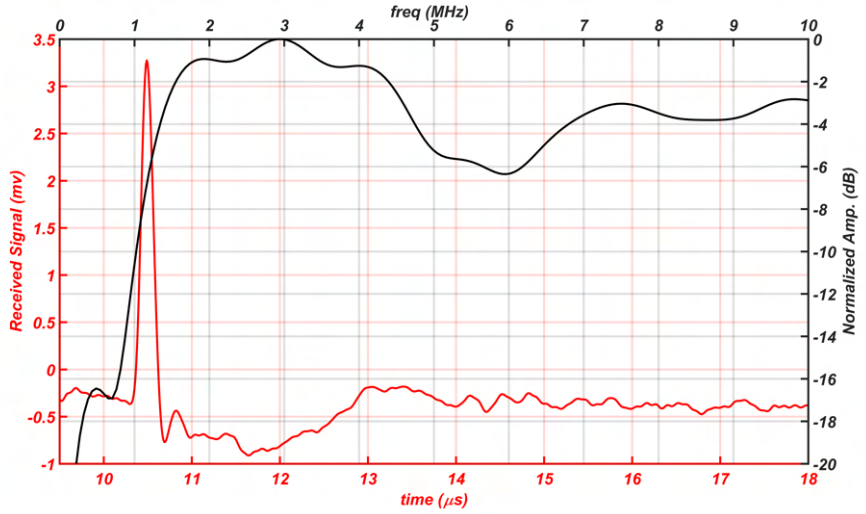


Figure 4.4: Photoacoustic signal received by the 0.2 mm needle hydrophone and its frequency response.

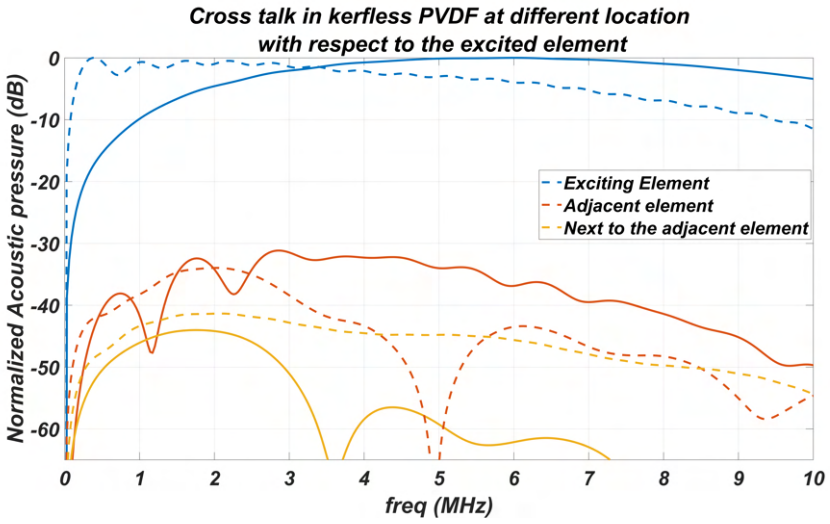


Figure 4.5: Simulated (solid line) and measured (dashed line) crosstalk in the PVDF array.

-30dB level. This implies that the lateral mechanical coupling in the PVDF kerfless array is low; thus, it wouldn't produce detrimental effect on array response.

## 4.4. Conclusion and Discussion

Based on FEA and measurement results, the phase change in the off-resonance PVDF is negligible. The analyzed crosstalk between the elements (Figure 4.5) is -30dB for the adjacent element indicating that it will not have detrimental effect on the beam profile of the array. We detect the received photoacoustic signal using our array and 0.2 mm hydrophone. We have designed and manufactured a broadband, kerfless, off resonance PVDF array for PA imaging of human plaque with low mechanical crosstalk (-30 dB) between the elements and high sensitivity in receive which can significantly improve the detection of PA signals.

# References


[1] R. Pakdaman Zangabad, G. Springeling, E. Noothout, R. Beurskens, N. de Jong, A. F. W. Van der Steen, G. van Soest, and V. Daeichin, *A kerfless pvdf array for photoacoustic imaging,* in *2018 IEEE International Ultrasonics Symposium (IUS)* (IEEE, 2018) pp. 1–4.

[2] C. L. Bayer, G. P. Luke, and S. Y. Emelianov, *Photoacoustic imaging for medical diagnostics,* Acoustics today **8**, 15 (2012).

[3] L. Li, L. Zhu, C. Ma, L. Lin, J. Yao, L. Wang, K. Maslov, R. Zhang, W. Chen, J. Shi, *et al.*, *Single-impulse panoramic photoacoustic computed tomography of small-animal whole-body dynamics at high spatiotemporal resolution,* Nature biomedical engineering **1**, 0071 (2017).

[4] K. Park, J. Y. Kim, C. Lee, S. Jeon, G. Lim, and C. Kim, *Handheld photoacoustic microscopy probe,* Scientific reports **7**, 13359 (2017).

[5] L. V. Wang, *Multiscale photoacoustic microscopy and computed tomography,* Nature photonics **3**, 503 (2009).

[6] K. Jansen, A. F. W. van Der Steen, H. M. M. van Beusekom, W. J. Oosterhuis, and G. van Soest, *Intravascular photoacoustic imaging of human coronary atherosclerosis,* Optics letters **36**, 597 (2011).

[7] V. Daeichin, M. Wu, N. De Jong, A. F. W. van der Steen, and G. van Soest, *Frequency analysis of the photoacoustic signal generated by coronary atherosclerotic plaque,* Ultrasound in medicine & biology **42**, 2017 (2016).

[8] S.-R. Kothapalli, T.-J. Ma, S. Vaithilingam, Ö. Oralkan, B. T. Khuri-Yakub, and S. S. Gambhir, *Deep tissue photoacoustic imaging using a miniaturized 2-d capacitive micromachined ultrasonic transducer array,* IEEE Transactions on Biomedical Engineering **59**, 1199 (2012).

[9] J. Zhang, S. H. Pun, Y. Yu, D. Gao, J. Wang, P. U. Mak, K. F. Lei, C.-H. Cheng, and Z. Yuan, *Development of a multi-band photoacoustic tomography imaging system based on a capacitive micromachined ultrasonic transducer array,* Applied optics **56**, 4012 (2017).

[10] O. Warshavski, C. Meynier, N. Sénégond, P. Chatain, J. Rebling, D. Razansky, N. Felix, and A. Nguyen-Dinh, *Experimental evaluation of cmut and pzt transducers in receive only mode for photoacoustic imaging,* in *Photons Plus Ultrasound: Imaging and Sensing 2016*, Vol. 9708 (International Society for Optics and Photonics, 2016) p. 970830.

[11] V. Daeichin, C. Chen, Q. Ding, M. Wu, R. Beurskens, G. Springeling, E. Noothout, M. D. Verweij, K. W. van Dongen, J. G. Bosch, *et al.*, *A broadband polyvinylidene difluoride-based hydrophone with integrated readout circuit for intravascular photoacoustic imaging,* Ultrasound in medicine & biology **42**, 1239 (2016).

[12] R. Pakdaman Zangabad, A. Bozkurt, G. Yaralıoğlu, J. G. Bosch, G. van Soest, and A. F. W. van der Steen, *Mutual radiation impedance of circular cmuts on a cylinder,* in *Ultrasonics Symposium (IUS), 2016 IEEE International* (IEEE, 2016) pp. 1–4.

[13] B. Bayram, M. Kupnik, G. G. Yaralıoğlu, Ö. Oralkan, A. S. Ergun, S. Wong, and B. Khuri-Yakub, *Finite element modeling and experimental characterization of crosstalk in 1-d cmut arrays,* IEEE transactions on ultrasonics, ferroelectrics, and frequency control **54** (2007), 10.1109/tuffc.2007.256.

[14] J. F. Dias, *An experimental investigation of the cross-coupling between elements of an acoustic imaging array transducer,* Ultrasonic Imaging **4**, 44 (1982).

[15] C. Morton and G. Lockwood, *Evaluation of kerfless linear arrays,* in *Ultrasonics Symposium, 2002. Proceedings. 2002 IEEE*, Vol. 2 (IEEE, 2002) pp. 1257–1260.

[16] V. Daeichin, D. Bera, S. Raghunathan, M. S. Motlagh, Z. Chen, C. Chen, E. Noothout, H. J. Vos, M. Pertijs, J. G. Bosch, *et al.*, *Acoustic characterization of a miniature matrix transducer for pediatric 3d transesophageal echocardiography,* Ultrasound in medicine & biology (2018), 10.1016/j.ultrasmedbio.2018.06.009.

[17] C. E. Démoré, J. A. Brown, and G. R. Lockwood, *Investigation of cross talk in kerfless annular arrays for high-frequency imaging,* IEEE transactions on ultrasonics, ferroelectrics, and frequency control **53**, 1046 (2006).

[18] D.-W. Wu, Q. Zhou, X. Geng, C.-G. Liu, F. Djuth, and K. K. Shung, *Very high frequency (beyond 100 mhz) pzt kerfless linear arrays,* IEEE transactions on ultrasonics, ferroelectrics, and frequency control **56** (2009), 10.1109/tuffc.2009.1311.

[19] Y. Chen and J. T. Yen, *A kerfless dual-layer transducer combined with beamforming by spatial matched filtering for high frame rate ultrasound imaging,* in *Ultrasonics Symposium (IUS), 2014 IEEE International* (IEEE, 2014) pp. 1001–1004.

[20] J. T. Yen, C. H. Seo, S. I. Awad, and J. S. Jeong, *A dual-layer transducer array for 3-d rectilinear imaging,* IEEE transactions on ultrasonics, ferroelectrics, and frequency control **56**, 204 (2009).

[21] T. Zawada, L. M. Bierregaard, E. Ringgaard, R. Xu, M. Guizzetti, F. Levassort, and D. Certon, *Characterization of kerfless linear arrays based on pzt thick film,* IEEE transactions on ultrasonics, ferroelectrics, and frequency control **64**, 1409 (2017).

# 5

# Design of a Dual Frequency Probe for Photoacoustic Imaging of the Carotid Artery

**Reza Pakdaman Zangabad,** Hendrik J. Vos, Nico de Jong, Antonius F. W. van der Steen, Gijs van Soest

This chapter has been published in proceeding of 2020 IEEE International Ultrasonics Symposium (IUS) [1].

*A dual frequency probe using a multi-layer piezoelectric material is proposed for simultaneous ultrasound and photoacoustic imaging of the carotid artery with a high resolution ultrasound and a high sensitivity photoacoustic image. The probe consists of lead zirconium titanate (PZT) for ultrasound stack and and polyvinylidene difluoride (PVDF) array for photoacoustic signal reception, which is placed on top of the PZT stack. We used 3D finite element analysis to evaluated a quarter of the full aperture of the dual frequency array, having 48 elements diced PZT-5H for ultrasound pulse-echo and 16 elements of 28 µm-thick, kerfless PVDF for photoacoustic receiving. We showed that considering the PVDF array as the second matching layer of the ultrasound stack minimized its loading effect at the cost of operating in a higher operation frequency of 9.9 MHz. We modeled a design with and without sub-dicing, where sub-dicing and subsequent suppression of lateral modes allows larger elements and thus larger aperture. The -3dB bandwidth of the ultrasound stack with and without sub-dicing are 87% and 75% relative to the center wavelengths. We found a transmit sensitivity of 17 kPa/V and 21 kPa/V for those two realizations respectively.*

## 5.1. Introduction

The carotid arteries (CA) supply the brain with oxygenated blood. Atherosclerotic plaques can cause a stenosis in CA, where lipid-rich, vulnerable plaques rupture lead to cerebral ischemic events such as stroke. Stroke is the largest single cause of death and disabilities worldwide. Examining the degree of stenosis in CA is done with ultrasound imaging and this is the main criterion for planning interventions such as surgical endarterectomy. However, this approach is unable to distinguish between the stable and unstable plaques, since stenosis grade does not discriminate well between those two categories [2, 3]. Plaque composition plays a very important role in this distinction.

Photoacoustic (PA) imaging is a relatively novel, non-invasive imaging modality that uses short optical pulses (usually delivered by a laser) to induce thermoelastic expansion at sites of optical absorption. This generates acoustic pressure waves in the absorbing regions of the tissue, allowing the creation of acoustic images of the optical absorption. PA imaging provides optical contrast of biological tissue which is promising for visualization of plaque composition [4, 5]. The advantage of PA is the use of multiple wavelengths to do spectroscopy study[6, 7]. Despite these advantages, the drawback of PA imaging is the limited penetration depth of the laser light. Some studies were focused on increasing the penetration depth by either introducing optical contrast agents [8] or by delivering the light locally [9].

The broadband nature of the PA signal of atherosclerotic plaques is dominated by low frequencies [10]. Lead zirconate titanate (PZT) based ultrasound imaging arrays with typical $60-80\%$ transducer fractional bandwidth provide high transmit and receive efficiency which is optimal for pulse-echo imaging. The limited bandwidth means that the sensitivity at PA frequencies may be low. PolyVinylidene difluoride (PVDF) offers relatively greater receive efficiency than PZT which potentially could increase the sensitivity of the PA image, especially when it is employed at frequencies off-resonance in combination with integrated amplification [11]. In our previous work, we demonstrated that an off-resonance, kerfless PVDF array is a suitable PA receiver with 10 MHz bandwidth for carotid artery imaging [12].

Recent studies on ultrasound probe development were focused on designing dual frequency acoustical stacks for different applications like contrast enhanced intravascular ultrasound [13], and transrectal acoustic angiography [14]. Merks *et al.* investigated a multilayer single element transducer transmitting at 2 MHz using PZT and receiving the non-linear acoustic waves with a PVDF film for acoustic bladder volume assessment[15]. Saitoh developed a dual frequency array for increasing the sensitivity in doppler imaging [16].

This paper presents the design of a dual frequency probe for PA imaging of the carotid artery using PZT and PVDF layers. Since PZT has a much larger acoustic impedance than soft tissue, the ultrasound coupling efficiency is impaired, which can be mitigated by the application of one or multiple matching layers. The design of this matching structure interacts with the bandwidth of the transducer response and offers the opportunity to tailor the matching layers to jointly optimize bandwidth and sensitivity [17]. We focus on the pulse-echo performance of the dual layer array with the ultrasound operation frequency of approximately 10 MHz. We use

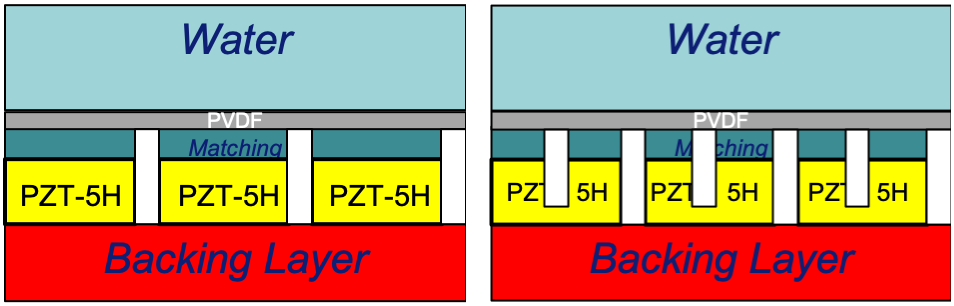


(a) (b)

Figure 5.1: Cross-section of the modeled transducer **(a)** without and **(b)** with subdicing of the elements.

two matching layers where the second matching layer is the PVDF receive layer, such as characterized in our previous work [12], and analyze the design using finite element simulations.

## 5.2. Materials and Methods

In the design of a 1D transducer array, the length of the element should be at least 30 times the wavelength at the central frequency, and the width-to-thickness ratio should be smaller than 0.7 to prevent the excitation of lateral modes [18]. The 3D simulation study is performed using the Finite Element Analysis (FEA) software package COMSOL Multiphysics. The proposed dual layer array for CA imaging has 192 elements for ultrasound pulse-echo and 64 elements of kerfless PVDF array for PA. In this study we analyzed a quarter of the full aperture. Figure 5.1 shows a schematic view of the dual layer transducer array used for the first study. We adopt the (previously characterized) PVDF layer, with a fixed thickness of 28 μm, as the PA receive layer. We did not study the acoustic response of this layer in the FEM simulations.

### 5.2.1. Matching layer analysis

Following the theory of acoustic matching presented in [17], the front half of the transducer were treated as a quarter-wave matching layer, in addition to the other quarter wave matching layers bonded to the transducer. The optimum input impedance of the acoustic load line at the resonance frequency can be formulated as:

$$Z_{IN} = \frac{Z_{piezo}^2}{Z_m + Z_b}, \tag{5.1}$$

where $Z_{piezo}$ is the acoustic impedance of the piezoelectric and $Z_m$ is the acoustic impedance of the medium.

The matching layer formulation for one quarter wave is:

| layer | material | material properties |
|---|---|---|
| PZT | Ceramic (PZT-5H) | $\rho$ = 7700 $kg/m^3$<br>$c_{11} = 127$; $c_{12} = 80$; $c_{13} = 84$;<br>$c_{33} = 117$; $c_{44} = 23$; $c_{66} = 24$<br>$e_{15} = 17$; $e_{31} = -6.6$; $e_{33} = 23$<br>Z = 30.76 MRayl |
| First Matching | Conductive epoxy | $\rho$ = 4880 $kg/m^3$<br>Y = 10.77 GPa; $\nu = 0.3$;<br>Z = 8.3 MRayl |
| Second Matching | PVDF | $\rho$ = 1780 $kg/m^3$ Y = 2.2 GPa;<br>$\nu = 0.29$; Z = 2.27 MRayl |
| Backing | Tungestan loaded epoxy | $\rho$ = 4880 $kg/m^3$<br>Y = 10.77 GPa; $\nu = 0.3$;<br>Z = 8.3 MRayl |

Table 5.1: Material properties used in the simulation.



$$Z_{layer} = Z_{piezo}^{1/3} \times Z_m^{2/3}$$
$$Z_{in} = Z_{piezo}^{4/3} \times Z_m^{1/3} \tag{5.2}$$

and the formulation for two quarter wave layers is:

$$Z_{layer1} = Z_{piezo}^{4/7} \times Z_m^{3/7}$$
$$Z_{layer2} = Z_{piezo}^{1/7} \times Z_m^{6/7} \tag{5.3}$$
$$Z_{in} = Z_{piezo}^{8/7} \times Z_m^{1/7}$$

Table 5.1 lists the material parameters used in the simulation: the impedance $Z_{piezo}$ of the PZT-5H layer is 30.7 MRayl, while $Z_m$ of the water coupling medium is 1.5 MRayl.

Using Equation 5.1, the input impedance will be 47.1 MRayl. Calculating the input impedance using Equation 5.2 and Equation 5.3 will yield input impedances of 108.6 MRayl and 52.4 MRayl for designs based on one and two matching layers, respectively. The value of $Z_{in}$ for two matching layers is slightly bigger than the optimum value of the $Z_{IN}$ accorindg to Equation 5.1. Thus, the choice of using two matching layers will broaden the transducer bandwidth.

### 5.2.2. Finite Element Analysis

3-D FEM transient analysis is carried out using COMSOL Multiphysics 5.3. We analyzed the pressure profile on the surface of the probe. A Perfectly Matched Layer (PML) was used as an absorbing boundary which is located $1\lambda$ away from the surface of the array at the lowest frequency. The model was simplified by simulating a quarter of the array, with appropriate symmetry boundary conditions in the lateral direction, along the y-axis (Figure 5.2). The domain mesh size was set to

the minimum acceptable size of $\frac{\lambda_1}{15}$ at the highest operating frequency. The lowest and highest operating frequencies are set to be 1 MHz and 20 MHz respectively. A single-cycle sine wave of 10 MHz with an amplitude of 20 $V_{pp}$ was applied to the PZT-5H. This will provide 100% fractional bandwidth to analyze the transmission response. In order to fully resolve the frequency response, the time step was set to $\frac{1}{20}$ of the of the sine wave period.

We analyzed three array designs in this study, which differ in their operating frequency

1. Current carotid artery imaging probes work at a center frequency near 7.5 MHz. We investigated the effect of adding a PVDF layer on the frequency response of such an array.

2. To minimize the loading effect of the PVDF layer, the US pulse-echo stack was redesigned by considering the PVDF as the second matching layer of the PZT elements, eventuating in a higher operation frequency of 9.5 MHz. We modeled the response of such an array.

3. Subdicing suppresses lateral modes, and thus allows larger elements and larger aperture. Design 2 was modified to examine the impact of this modification.

Based on the Equation 5.3, the first and second matching layers acoustic impedance for PZT-5H should be 8.42 MRayl and 2.31 MRayl respectively where the value of the second matching layer is very close to the PVDF acoustic impedance (Z=2.27 MRayl). Table 5.2 summarize the geometrical dimensions used in these three designs.

In the first design, the element width of the PZT-5H and PVDF are 200 μm and 600 μm, respectively. The kerf between the PZT elements in all designs is 20 μm dictated by the dicing saw thickness. This leads to a full aperture size of 2.3 cm where there are 192 PZT elements and 64 PVDF elements. In order to improve the frequency response of the transmitting part, we increased the operation frequency to 10 MHz, where the quarter wavelength second matching layer thickness at 10 MHz was approximately equal to the prescribed 28 μm thickness of the PVDF. In the lower frequency design, the element width was bigger in comparison with the higher frequency design (half lambda for both). Consequently, the higher frequency design had a smaller aperture for carotid imaging. There are two approaches for increasing the aperture length: increasing the number of elements, or to utilize subdicing. We aim to limit the total number of elements to 256 for practical reasons (connectivity and compatibility with commercial reseacrh ultrasound systems), 192 for pulse-echo and 64 for PA. Thus, we designed the probe with sub-dicing approach in the third geometry [19]. Janjic *et al.* showed that cutting to a depth of 70% of the total element thickness can significantly improve the transducer performances [20].

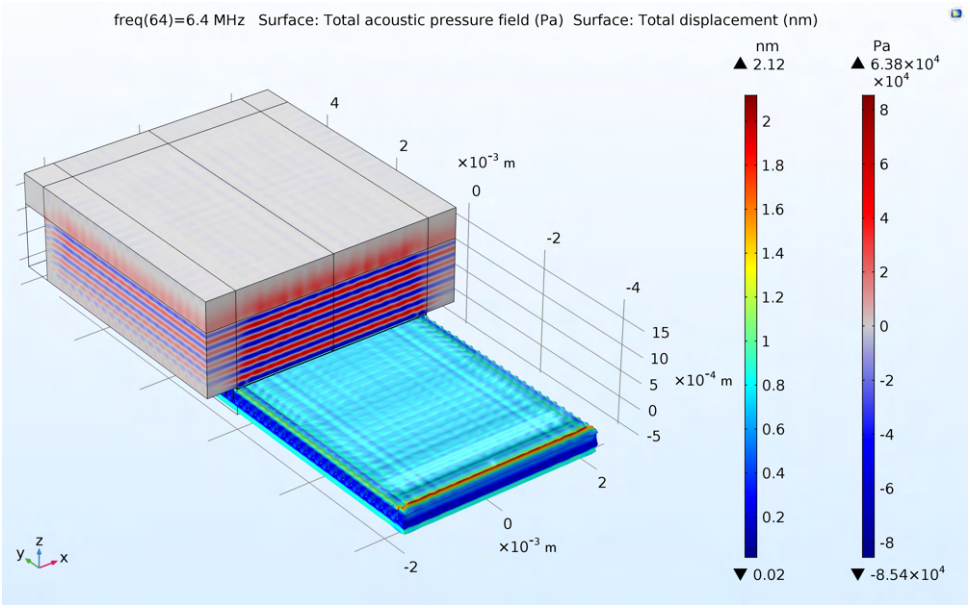


Figure 5.2: 3D representation of the simulated array for design 2.

## 5.3. Results

We analyzed three different results for photoacoustic and ultrasound imaging of the carotid artery. Figure 5.3a depicts the time and frequency response of the array based on the parameters for design 1. The time signal has a long tail which narrows the bandwidth, attributed to the loading of the PVDF layer on the PZT. The 28 μm-thick PVDF layer was not an optimal matching for the first design. The bandwidth of the ultrasound array measured at -3dB is 4.8 MHz with center frequency of 7.7 MHz; thus, making 62% fractional bandwidth. This relatively narrow band array is due to the suboptimal thickness of the PVDF as a second matching layer.

Figure 5.3b and Figure 5.3c show the array performance where the optimum response was achieved. The -3dB bandwidth of the non-subdiced and subdiced designs are 7.4 MHz and 8.7 MHz, respectively, centered at 9.9 MHz. The transmit sensitivity of the three designs are 19 $\mathrm{kPa/V}$, 21 $\mathrm{kPa/V}$, and 17 $\mathrm{kPa/V}$.

## 5.4. Conclusion and Discussion

We used the theory of two matching layers for designing the arrays for carotid artery imaging. Based on this theory, the acoustic impedance of the second matching layer needs to be 2.31 MRayl for the PZT-5H ultrasound stack. The acoustic impedance of the PVDF is very similar to this value, making the PVDF a good candidate to be used in the array. In our previous work, we experimentally characterized the received PA signal using the off-resonance kerfless PVDF array. It demonstrated

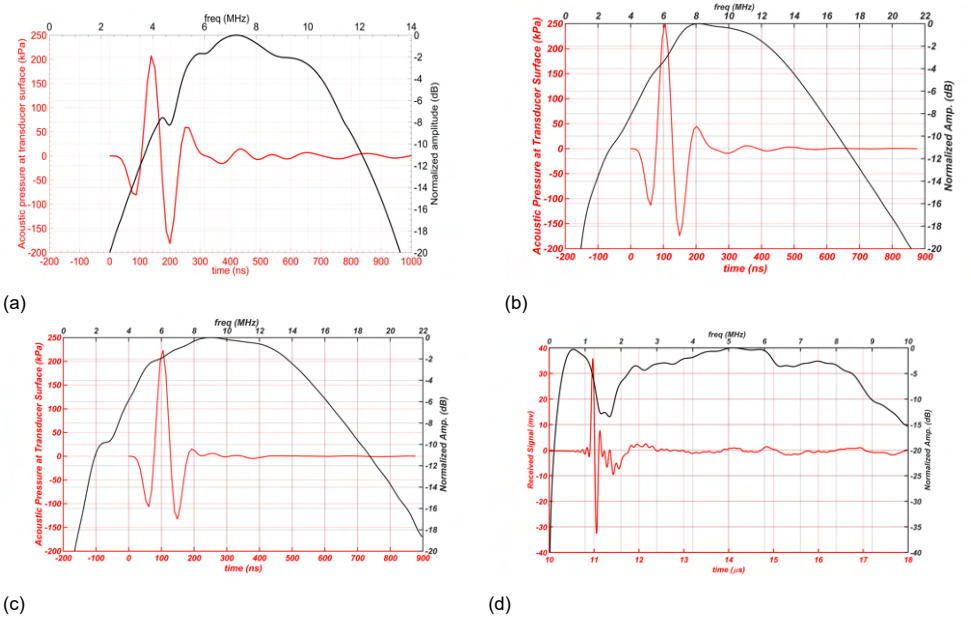


Figure 5.3: **(a)** Time and frequency response of the non optimum array design operating at 7.5 MHz (design 1), the response of the array based on design 2 **(b)** and design 3 **(c)** are shown. **(d)**, The photoacoustic signal received by the PVDF element and its frequency [12]. response.

| Layer | Design 1 (7.5 MHz) | Design 2 (10 MHz) | Design 3 (10 MHz, sub-dice) |
|---|---|---|---|
| PZT-5H (th × w) [μm] | 120 × 200 | 90 × 100 | 90 × 200 |
| First matching (th × w) [μm] | 53 × 200 | 40 × 100 | 40 × 200 |
| PVDF (th × w) [μm] | 28 × 600 | 28 × 300 | 28 × 600 |

Table 5.2: Geometrical dimensions used in the simulation

good performance as a PA receiver with high sensitivity. Figure 5.3d depicts the received PA signal in time and frequency domains using our array. The dip at 1.45 MHz is due to coupling to the quartz mounting structure in that experiment. The response is expected to change favorably when mounted on a lower impedance substrate like the first matching layer. The first matching layer may be made of conventional materials, such as conductive epoxy.

Based on FEA results, the time signal of the generated acoustic pressure is Gaussian shaped and the frequency response of the signals is broadband. The -3dB BW of the arrays with and without sub-dicing are 87% and 75% fractional respectively and both designs have a center frequency of 9.9 MHz. The transmit

sensitivity of the non-subdiced and subdiced arrays are 21 kPa/V and 17 kPa/V respectively. We designed a broadband, dual frequency array having two acoustical stacks for US and PA imaging of the carotid arteries. The PVDF layer was previously demonstrated to be a suitable receiver, while the overall stack was designed for optimal pulse-echo performance.

# References

[1] R. Pakdaman Zangabad, H. J. Vos, N. de Jong, A. F. W. van der Steen, and G. van Soest, *Design of a dual frequency probe for photoacoustic imaging of the carotid artery,* in *2020 IEEE International Ultrasonics Symposium (IUS)* (IEEE, 2020) pp. 1–4.

[2] S. Carr, A. Farb, W. H. Pearce, R. Virmani, and J. S. Yao, *Atherosclerotic plaque rupture in symptomatic carotid artery stenosis,* Journal of vascular surgery **23**, 755 (1996).

[3] N. Nighoghossian, L. Derex, and P. Douek, *The vulnerable carotid artery plaque: current imaging methods and new perspectives,* Stroke **36**, 2764 (2005).

[4] A. B. E. Attia, G. Balasundaram, M. Moothanchery, U. Dinish, R. Bi, V. Ntziachristos, and M. Olivo, *A review of clinical photoacoustic imaging: Current and future trends,* Photoacoustics , 100144 (2019).

[5] A. Dima and V. Ntziachristos, *Non-invasive carotid imaging using optoacoustic tomography,* Optics express **20**, 25044 (2012).

[6] K. Jansen, M. Wu, A. F. W. van der Steen, and G. van Soest, *Lipid detection in atherosclerotic human coronaries by spectroscopic intravascular photoacoustic imaging,* Optics express **21**, 21472 (2013).

[7] K. Jansen, A. F. W. van der Steen, M. Wu, H. M. M. van Beusekom, G. Springeling, X. Li, Q. Zhou, K. K. Shung, D. P. de Kleijn, and G. van Soest, *Spectroscopic intravascular photoacoustic imaging of lipids in atherosclerosis,* Journal of biomedical optics **19**, 026006 (2014).

[8] C. Kim, T. N. Erpelding, L. Jankovic, M. D. Pashley, and L. V. Wang, *Deeply penetrating in vivo photoacoustic imaging using a clinical ultrasound array system,* Biomedical optics express **1**, 278 (2010).

[9] P. Kruizinga, A. F. W. van der Steen, N. de Jong, G. Springeling, J. L. Robertus, A. van der Lugt, and G. van Soest, *Photoacoustic imaging of carotid artery atherosclerosis,* Journal of biomedical optics **19**, 110504 (2014).

[10] V. Daeichin, M. Wu, N. De Jong, A. F. W. van der Steen, and G. van Soest, *Frequency analysis of the photoacoustic signal generated by coronary atherosclerotic plaque,* Ultrasound in medicine & biology **42**, 2017 (2016).

[11] V. Daeichin, C. Chen, Q. Ding, M. Wu, R. Beurskens, G. Springeling, E. Noothout, M. D. Verweij, K. W. van Dongen, J. G. Bosch, *et al.*, *A broadband polyvinylidene difluoride-based hydrophone with integrated readout circuit for intravascular photoacoustic imaging,* Ultrasound in medicine & biology **42**, 1239 (2016).

[12] R. Pakdaman Zangabad, G. Springeling, E. Noothout, R. Beurskens, N. de Jong, A. F. W. Van der Steen, G. van Soest, and V. Daeichin, *A kerfless pvdf array for photoacoustic imaging,* in *2018 IEEE International Ultrasonics Symposium (IUS)* (IEEE, 2018) pp. 1–4.

[13] Z. Wang, W. Huang, X. Jiang, K. H. Martin, and P. A. Dayton, *Dual-frequency ivus array for contrast enhanced intravascular ultrasound imaging,* in *2015 IEEE International Ultrasonics Symposium (IUS)* (IEEE, 2015) pp. 1–4.

[14] S. Li, J. Kim, Z. Wang, X. Jiang, S. Kasoji, B. Lindsey, and P. A. Dayton, *A 3 mhz/18 mhz dual-layer co-linear array for transrectal acoustic angiography,* in *2015 IEEE International Ultrasonics Symposium (IUS)* (IEEE, 2015) pp. 1–4.

[15] E. J. Merks, A. Bouakaz, N. Bom, C. T. Lancee, A. F. W. van der Steen, and N. de Jong, *Design of a multilayer transducer for acoustic bladder volume assessment,* IEEE transactions on ultrasonics, ferroelectrics, and frequency control **53**, 1730 (2006).

[16] S. Saitoh, M. Izumi, and Y. Mine, *A dual frequency ultrasonic probe for medical applications,* IEEE transactions on ultrasonics, ferroelectrics, and frequency control **42**, 294 (1995).

[17] C. S. Desilets, J. D. Fraser, and G. S. Kino, *The design of efficient broadband piezoelectric transducers,* IEEE Transactions on sonics and ultrasonics **25**, 115 (1978).

[18] N. De Jong, N. Bom, J. Souquet, and G. Faber, *Vibration modes, matching layers and grating lobes,* Ultrasonics **23**, 176 (1985).

[19] M. Shabanimotlagh, J. Janjic, S. Raghunathan, M. A. Pertijs, N. de Jong, and M. Verweij, *The role of sub-dicing in the acoustical design of an ultrasound matrix transducer for carotid arteries imaging,* in *2016 IEEE International Ultrasonics Symposium (IUS)* (IEEE, 2016) pp. 1–4.

[20] J. Janjic, M. Shabanimotlagh, G. van Soest, A. F. W. van der Steen, N. de Jong, and M. D. Verweij, *Improving the performance of a 1-d ultrasound transducer array by subdicing,* IEEE transactions on ultrasonics, ferroelectrics, and frequency control **63**, 1161 (2016).

# 6

# Photoacoustic Flow Velocity Imaging Based On Complex Field Decorrelation

**Reza Pakdaman Zangabad,** Sophinese Iskander-Rizk, Pim van der Meulen, Kornelis A. B. Meijlink, Klazina Kooiman, Tianshi Wang, Antonius F. W. van der Steen, Gijs van Soest

This chapter has been published in the Photoacoustic Journal (2021) [1].

*Photoacoustic (PA) imaging can be used to monitor flowing blood inside the microvascular and capillary bed. Ultrasound speckle decorrelation based velocimetry imaging was previously shown to accurately estimate blood flow velocity in mouse brain (micro-)vasculature. Translating this method to photoacoustic imaging will allow simultaneous imaging of flow velocity and extracting functional parameters like blood oxygenation. In this study, we use a pulsed laser diode and a quantitative method based on normalized first order field autocorrelation function of PA field fluctuations to estimate flow velocities in an ink tube phantom and in the microvasculature of the chorioallantoic membrane of a chicken embryo. We demonstrate how the decorrelation time of signals acquired over frames are related to the flow speed and show that the PA flow analysis based on this approach is an angle independent flow velocity imaging method.*

## 6.1. Introduction

Flow imaging is an important method for extracting functional information about physiological response to stimuli or pathological changes in tissue. Established technologies like ultrasound and optical coherence tomography (OCT) offer flow imaging capabilities, often based on Doppler or variance analysis [2, 3]. Such flow imaging techniques have yielded valuable information in selected applications, for instance in diagnoses of retinal disorders using OCT angiography (OCTA) [4–6] and of cardiac valve insufficiency using Color Doppler echocardiography [7, 8]. Recent years have seen an intensive research effort directed at microvascular brain imaging using Power Doppler ultrasound, which allows non- or mildly invasive assessment of functional neurological response from rodents to humans [9–12].

Scattering-based imaging modalities such as ultrasound and OCT are widely deployed and can be powerful in selected applications but also have limitations, such as low contrast to (mammal) red blood cells (RBCs) in ultrasound, and imaging depth in OCT. Doppler methods are intrinsically angle-dependent, while variance-based flow techniques cannot quantify velocity. Photoacoustic flow imaging has intrinsic contrast to hemoglobin, and can assess oxygen saturation by multispectral imaging. It offers a useful trade-off between spatial resolution and imaging depth, making it a suitable platform for quantitative imaging of microvascular flow.

Recent studies on PA flow imaging are based on Doppler shift [13, 14], density tracking based on cross-correlation in the time [15, 16] or spatial domain [17, 18], transit time of single [19] or particle ensembles [20, 21], and amplitude encoding [22]. As laser technology evolves, more high pulse repetition frequency (PRF) lasers are utilized in PA flow imaging. Liu et al. [23] imaged the blood flow of a mouse ear utilizing a functional optical resolution photoacoustic microscopy system and analyzing based on changes in the Grüneisen relaxation effect [24, 25] caused by blood flow. All these methods share the requirement for many PA acquisitions to characterize flow. Among all these flow imaging approaches, quantitative imaging of vector flow (direction and magnitude) has remained elusive.

Ultrasound speckle decorrelation based velocimetry and imaging was recently shown to accurately estimate blood flow velocity in controlled flow phantoms, and in the mouse brain [26]. Similar analyses have been used in OCTA [27]. In this study, we translate this method to photoacoustic velocity imaging. It allows simultaneous imaging of flow velocities and blood oxygenation.

Randomly distributed absorbing particles within the irradiated region generate an initial positive pressure rise. The propagating acoustic wavelets interfere with each other, creating a random signal that fluctuates subject to the flow in the channel. By retaining the phase of the field and examining the decorrelation time due to motion in the two directions of the image plane, an ascending or descending velocity vector can be extracted.

To determine the blood flow speed using PA signals, we characterize the fluctuation of the beam-formed PA RF signal of the moving particles. We quantitatively analyzed the normalized first-order complex field auto-correlation function of flow-induced fluctuations in the beam-formed images for velocity imaging [26, 27]. In this study, we used a fast pulsed laser diode illuminator (PLDI) enabling kHz frame

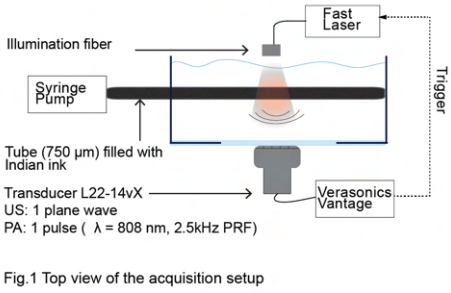


(a)

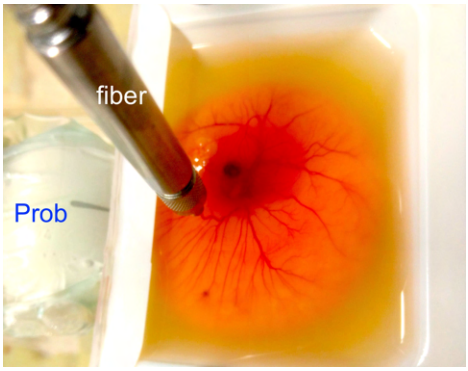


(b)

Figure 6.1: **(a)**Top view of the acquisition setup, **(b)** Chicken Embryo setup

rates to sample the rapid decorrelation. We validated the analysis in a phantom with known flow speeds. We also imaged microvascular flow *in vivo* and showed that the obtained results are in agreement with ultrasound velocimetry.

6

## 6.2. Materials and Methods

### 6.2.1. Theory of normalized first order temporal autocorrelation function

The complex two-dimensional point spread function (PSF) of a photoacoustic imaging system may be approximated by a Gaussian envelope modulating the complex exponential that describes the spatially varying phase of the PSF, denoted as $h$:

$$h\left(x-x_0, z-z_0\right)=e^{-\frac{(x-x_0)^2}{2\sigma_x^2}-\frac{(z-z_0)^2}{2\sigma_z^2}} e^{ik_0(z-z_0)} \tag{6.1}$$

where $(x_0, z_0)$ is the (lateral, axial) position of a pixel in the image, $\sigma_x, \sigma_z$ parametrize the width of the Gaussian profile in the two directions, $k_0$ is the wave number at the center frequency of the transducer, assuming a broadband signal from the PA source. This function describes the response of the beamformed radiofrequency (RF) data, by a one-dimensional array along the $x$ direction at $z = 0$. The phase term $e^{ik_0(z-z_0)}$ accounts for one-way acoustic propagation. The Gaussian approximation in (6.1) in $x$ assumes that the ultrasound detection array is large in the $x$ direction and its response is apodized according to a Gaussian function, for instance by the finite width angular response of the elements. The $z$ response is usually governed by the frequency response of the transducer, which can often be approximated by a Gaussian function. We further assume that that $z_0 >> \sigma_x, \sigma_z$.

The induced photoacoustic source pressure by a moving particle can be formulated as [24, 28]

$$\begin{aligned} P_0\left(x, z, t\right) &= \Gamma F \mu_a\left(x, z, t\right) \\ &= \Gamma F \mu_a \delta\left(x-x_s(t), z-z_s(t)\right) \end{aligned} \tag{6.2}$$

where $\Gamma$ is the Grüneisen parameter describing the conversion from absorbed optical energy to thermoelastic expansion, $F$ is the optical fluence, and $\mu_a$ is the optical absorption coefficient at the illumination wavelength, assumed to be identical for all particles. The particle is modeled as a point source, located at an instantaneous position $(x_s(t), z_s(t))$. $t$ is the slow time, between different PA frames in an acquisition. Note that we disregard spatial variations in $\Gamma$ and $F$.

The time varying PA signal detected from a measurement pixel $(x_0, z_0)$ at time $t$ is computed as the convolution of the source pressure, produced by $n$ randomly positioned point sources in the field of view, with the PSF:

$$\begin{aligned} S(x_0, z_0, t) &= \sum_{j=1}^{n} \int P_0\,(x, z, t) \times h\,(x - x_0, z - z_0)\,dx dz \\ &= \Gamma F \mu_a \sum_{j=1}^{n} h\left(x_{s,j}(t) - x_0, z_{s,j}(t) - z_0\right) \end{aligned} \tag{6.3}$$

Adopting the shorthand $P_s = \Gamma F \mu_a$, and assuming the particles are moving with a vector velocity $(v_x, v_z)$, the PA signal at time lag $\tau$ would become:

$$\begin{aligned} S(x_0, z_0, t + \tau) = P_s \sum_{j=1}^{n} & e^{-\frac{(x_{s,j}(t) + v_x \tau - x_0)^2}{2\sigma_x^2} - \frac{(z_{s,j}(t) + v_z \tau - z_0)^2}{2\sigma_z^2}} \\ & \times e^{ik_0 (z_{s,j}(t) + v_z \tau - z_0)} \end{aligned} \tag{6.4}$$

In images containing many unresolved PA sources, such as RBCs in a blood vessel, limited sampling of the extensive $(\mathbf{k}, \omega)$ spectrum of the PA signal introduces the familiar edge, or boundary build-up, artefacts [29–31]. This dominant stationary component in the image drowns out the fluctuating signal due to flow or particle motion. Applying a spatiotemporal singular value decomposition (SVD) filter [32] to the acquired data will remove the boundary signals. The movement of particles will cause the SVD filtered PA signal $S$ to fluctuate at a rate that is proportional to the flow speed. Thus, particle motion can be quantified based on by analyzing the decay of the normalized first-order field autocorrelation function $g_1(\tau)$, computed from the beamformed RF PA image. We consider only relatively large vessels, such that the spatial variation in $(v_x, v_z)$ occurs on length scales smaller than $(\sigma_x, \sigma_z)$, so the PSF of each measurement pixel samples a uniform velocity. We follow ref. [27] and the derivations therein:

$$g_1\,(x_0, z_0, \tau) = E\left[\frac{\langle S^*(x_0, z_0, t) S(x_0, z_0, t + \tau)\rangle_t}{\langle S^*(x_0, z_0, t) S(x_0, z_0, t)\rangle_t}\right] \tag{6.5}$$

E[...] indicates the average over random initial positions; $\langle \ldots \rangle_t$ represents an ensemble temporal average; and * denotes the complex conjugate.

Using equations (6.3) to (6.5),the normalized first order field autocorrelation function of moving particles can be written as:

$$g_1(\tau) = e^{-\left(\frac{v_x\tau}{2\sigma_x}\right)^2 - \left(\frac{v_z\tau}{2\sigma_z}\right)^2} e^{ik_0 v_z \tau} \tag{6.6}$$

The decorrelation of the signal at each location in the image is thus governed by the particle velocities in $x$ and $z$, with higher $v_x$ and $v_z$ leading to faster decorrelation. Fitting the complex autocorrelation function $g_1(\tau)$ of the PA signal from an object with flow thus allows us to extract the vector velocity $\mathbf{v} = (v_x, v_z)$ on a per pixel basis from a series of images. The retention of the phase factor $\exp(ik_0 v_z \tau)$ in (equation (6.6)) introduces directionality, as the sign of $v_z$ determines the rotation direction in the complex plane. Analogous to ultrasound velocimetry imaging, which has been called vUS, we propose to name this approach vPA, for photoacoustic velocimetry imaging. Consequently, for PA flow velocity imaging, we will calculate the $g_1(\tau)$ based on equation (6.5) and will estimate the values of $v_x, v_z$ from equation (6.6) and allocate to each pixel its velocity value. By moving the reference frame, we will be able to do time-resolved velocimetry imaging.

### 6.2.2. Experimental setup

In a water tank, a tube made of low-density polyethylene (LDPE) with a inner diameter of 750 µm was filled with an Indian ink solution, diluted 1:50 v/v in water. Flow ranging from 1.9 mm/s - 19 mm/s was induced using a controllable syringe pump (PERFUSOR secura FT).

A PLDI of wavelength $\lambda_1 = 808$ nm with a pulse duration of $T_p = 34$ ns (QD-Q1R10-ILO, Quantel Laser, France) and 1.18 mJ pulse energy, capable of a maximum PRF of 6 kHz, was coupled to a 2 mm core diameter step-index optical fiber. The fiber delivered the pulsed excitation light to the imaging setup.

PA signal acquisition, as well as US pulse echo imaging (1 plane wave per frame, $0°$), was performed with a commercial research ultrasound imaging system (Vantage 256, Verasonics Inc. Kirkland, WA, USA) and a linear array ultrasonic probe (L22-14vX, Verasonics Inc. Kirkland, WA, USA). The transducer had 128 elements with a pitch of 0.1 mm and a center frequency of 19 MHz with a bandwidth of 11.5 MHz (60%, -6 dB). It has an elevation focus at z=6 mm, and an US imaging resolution of $\sigma_x = 180$ µm (lateral) and $\sigma_z = 135$ µm (axial). See Figure 6.1a for a schematic.

The probe was positioned in front of the tube such that the black Indian ink flowed along the lateral direction of the ultrasound imaging plane. The distance between the probe and the tube was between 10 and 17 mm. We examined two geometries, one in which the tube is oriented along the $x$ direction, and one with a 15° angle with the $x$-axis. The optical fiber was positioned over the tube, perpendicular with respect to the imaging plane.

### 6.2.3. Photoacoustic flow velocimetry imaging *in vivo*

We used the chicken embryo model to test our quantitative method *in vivo*. All animal experiments were conducted in accordance with the Netherlands Experiments

on Animals Act and in accordance with the European Council (2010/63/EU) on the protection of animal use for scientific purposes. Fertilized chicken eggs were incubated in a 37°C incubator at 60–65% humidity for 6 days. Immediately prior to imaging, the egg content was removed form the shell by creating an opening over the air sack using tweezers as described in detail by Meijlink et al [33]. The content was placed in a plastic holder ($85 \times 85 \times 24$ mm VWR, the Netherlands) customized with an acoustical window on one side (Figure 6.1b). A heater was used to maintain the temperature at 37°C throughout the experiment. The optical fiber was positioned to irradiate the vasculature of the chorioallantoic membrane (CAM). The ultrasound transducer was positioned such that the vascular plexus in the CAM was in the image plane. Ultrasound and photoacoustic signals were recorded for one second at a PRF of 2.5 kHz.

### 6.2.4. Spatiotemporal resolution

In equation (6.2), we have assumed that the PA sources can be modeled as point particles. In the experiments presented in this study, we have used India ink, in which small suspended carbon particles of a size 0.1–1 μm [34] are the absorbers. Avian RBCs, which generated the signal in our chicken embryo experiments, are ellipses with a long diameter of approximately 12 μm [35], which, although large compared to mammal erythrocytes, is still about an order of magnitude smaller than the ultrasound wavelengths we detect.



The usual assumption of stress confinement in PA generation, which justifies equation (6.2) through the separation of the deposited heat $Q(x,T) = q(x)\delta(T)$ and $P_0(x) = \Gamma q(x)$, merits closer inspection. With $T_p = 34$ ns, the stress confinement criterion is satisfied for sources larger than 50 μm, such as the phantom channel and some of the allantois vessels investigated in this study. The fluctuating PA signal is generated from collections of randomly positioned small particles inside the vessel. In this case, with thermal but not stress confinement, we need to convolve the instantaneous $P_0$ with the temporal characteristic of the laser pulse [36]. The laser pulse is nearly Gaussian, so the generated PA spectrum also has a Gaussian envelope with an upper band limit at approximately $1/(2T_p)$. Thus; the frequency components that are present in the PA signal are limited to approximately 17 MHz, reducing the effective signal bandwidth.

Ordinarily the resolution of raw PA images should be better than that of US images acquired with the same bandwidth, as the band limitation applies only in receive and the frequency spectrum of the source is assumed to be broad. That latter assumption is not true in our experiments, which impacts the spatial resolution in the image, and, equivalently, increases the correlation length in $z$. Instead of the $\sigma_z^{US} = 135$ μm for the transducer, we measured the PSF width in the PA images and found $\sigma_z^{PA} = 145$ μm and $\sigma_x^{PA} = 300$ μm which we used in the analysis of the signal decorrelation.

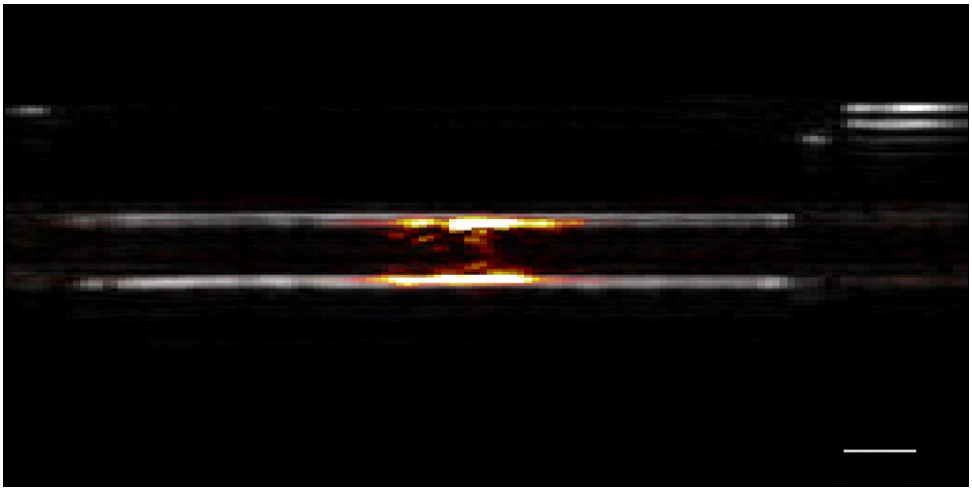

Figure 6.2: the beam-formed ultrasound (gray scale) and photoacoustic (red) image of the blank ink flowing through the tube, the scale bar is 1 mm.



### 6.2.5. Image acquisition and processing scheme

To accurately sample the fluctuation of the PA speckle dynamics of fast flows, a high-PRF light sources are a critical component. To optimize the data acquisition for the purpose of photoacoustic velocimetry imaging (vPA), we chose to limit US imaging to a single plane wave transmission. After the transmit and receive events of the US image, the ultrasound system was switched to a second receive profile defined for PA acquisition and generated an output trigger signal for the PLDI. There is a fixed 170 ns delay between the laser input trigger and laser firing. With this approach, we were able to acquire the US/PA signals at 2.5 kHz PRF for imaging depth of 20 mm. In addition, the total data acquisition time for each US/PA frames was selected to be 1 second (corresponding to 2500 frames).

We applied SVD filtering to the acquired PA and US data, and removed components with the five highest singular values from the signal in the phantom data to remove stationary components (including the boundary buildup). When imaging the chick embryo, cardiac motion can affect the temporal characteristics of the US/PA signals in an acquisition, and thus the decay of $g_1(\tau)$. Therefore, a proper background and bulk motion rejection of the acquired signals is required. To remove stationary signals and bulk motion from the *in vivo* data, we used a combination of SVD and high pass filtering [37]. The components with the 30 highest singular values were removed form the signal, followed by a tenth order Butterworth high pass filtering with a cutoff frequency of 5 Hz.

vPA images were computed using the algorithm described in section 6.2.1. In the *in vivo* experiments, we also computed flow velocities based on the acquired US images. The analysis of ref. [27] was applied, which describes the two-way acoustic delay in $g_1(\tau)$:

$$g_1^{US}(\tau) = e^{-\left(\frac{v_x\tau}{2\sigma_x}\right)^2 - \left(\frac{v_z\tau}{2\sigma_z^{US}}\right)^2} e^{2ik_0 v_z \tau} . \tag{6.7}$$

## 6.3. Results

### 6.3.1. Photoacoustic flow velocimetry imaging of the phantom study

Figure 6.2 shows the beam-formed ultrasound (gray scale) and photoacoustic (red) image of the diluted India blank ink flowing through the tube. Individual ink particles could not be resolved due to the high particle density; the expected "boundary buildup" is clearly visible, which is removed by SVD filtering before processing for velocimetry.

We acquired US/PA data sets for the pre-set velocities induced by the syringe pump and calculated the normalized first order autocorrelation function of $g_1(\tau)$ based on Equation (6.6). Figure 6.3a depicts the calculated speckle dynamics up to 250 ms time lag for different preset velocities. It also shows that the correlation drops quicker for the faster flows. By using Equations (6.5),(6.6) we can estimate the flow velocity of each pixel. Figure 6.3c and 6.3d show the photoacoustic velocimetry image of the preset flow speed with 12.7 mm/s and 19.0 mm/s where the tube has no angle with respect to the probe and is compared with the same preset flow speed for the tube (Figure 6.3f and 6.3e). Figure 6.3b is the colormap used to visualize the results where zero velocities are fully transparent represented at the middle and of the color wheel and it becomes more opaque as the flow speed increases. Based on equation (6.6), the $V_z$ component for the ascending flow is negative making the angle between the $V_x$ and $V_z$ to be negative.

Figure 6.3g shows the calculated $g_1(\tau)$ based on the flow phantom experiment with preset velocity of 12.7 mm/s and the fitted curve in the complex plane based on Equation 6.6. Figure 6.3h and 6.3i show the high correlation between the preset velocities and the vPA calculated velocities for transverse flows ($\theta = 0°$) and angled flows ($\theta = 15°$). The red lines are linear fits to the mean velocities, showing good agreement with errors $< 10\%$. The error bars in the figures are the standard deviations of the calculated vPA over different pixels.

### 6.3.2. Photoacoustic flow velocimetry imaging *in vivo*

We used a six day-old chicken embryo for the *in vivo* experiment to image the vasculature of the CAM. Figure 6.4a shows the beam-formed ultrasound image of the CAM without filtering. The microvasculature network of the CAM is not clear in this image. After applying SVD filtering, the microvasculature network can be easily distinguished and the stationary clutter was rejected without losing the small vessels. Similarly, bulk motion associated with the cardiac cycle was successfully removed in this manner. We applied this method to all acquired frames and then used the proposed method to estimate the velocity.

Figure 6.4c and Figure 6.4d show the ultrasound velocimetry and photoacoustic velocimetry images of the CAM with the same colormap of the Figure 6.3b overlaid

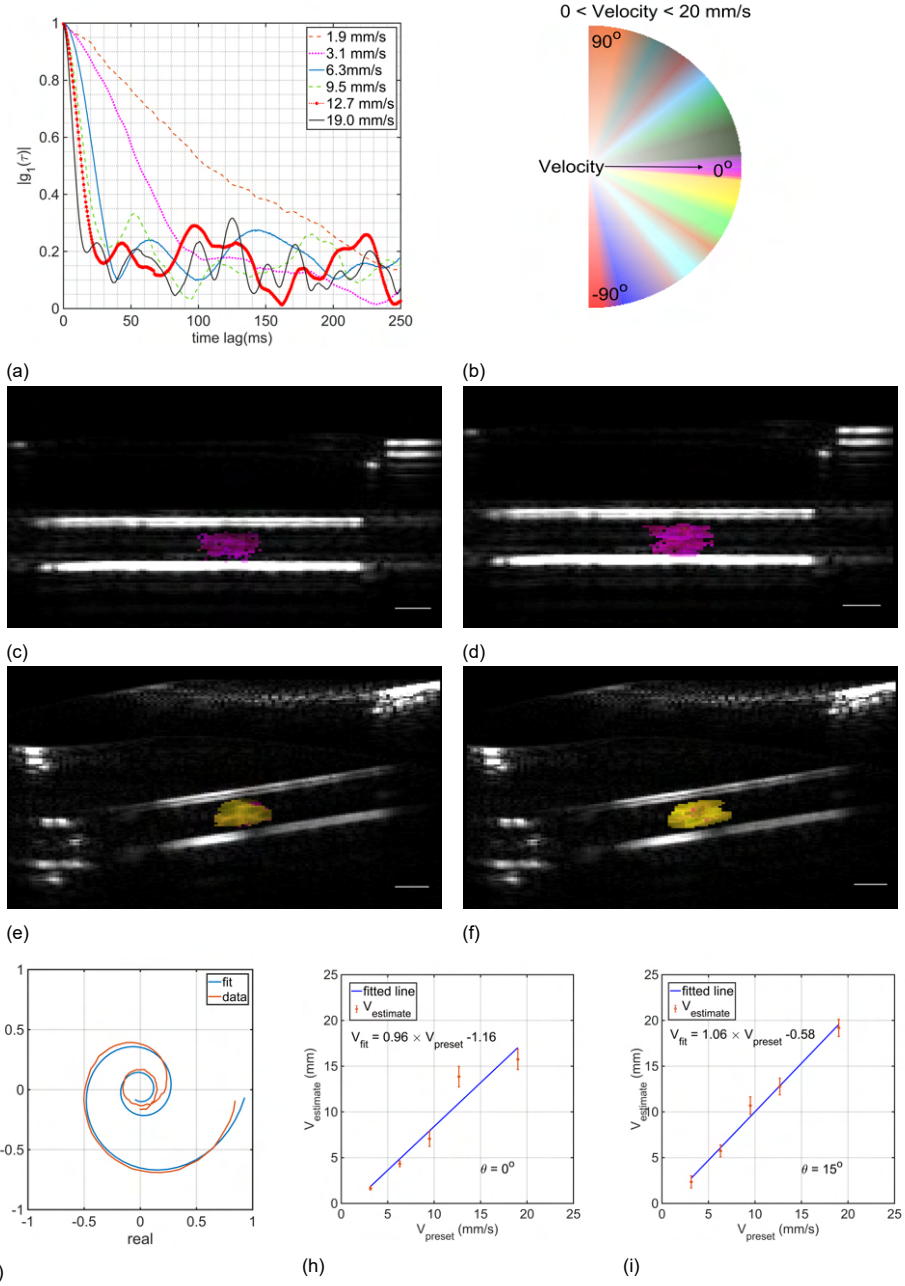


Figure 6.3: **(a)** calculated $g_1(\tau)$ of the phantom study with pre-set velocities of V = 1.9, 3.1, 6.3, 9.5, 12.7, and 19.0 mm/s, **(b)** is the colormap used for presenting the data vPA and vUS, **(c,d)** the photoacoustic velocimetry (vPA) image of the pre-set flow speed with 12.7 and 19.0 mm/s, **(e,f)** depict the vPA of the same pre-set flow speed while the tube has an angle of 15 degree with respect to the probe. The scale bar is 1 mm. **(g)** the calculated $g_1(\tau)$ from the experiment and the corresponding fitting curve. The accuracy of the fitting algorithm for $\theta = 0°$ **(h)**, and $\theta = 15°$ **(i)**.

on the ultrasound image of the corresponding frame, respectively. The vUS shows that blood flow in the allantois vessels has a maximum flow speed of 16 mm/s. At side branches, the velocity decreases as the vessels get narrower. Furthermore, vPA was compared with vUS in the region where the PA signals were recorded, and resulted in the same maximum flow velocity. Figure 6.4e shows the averaged estimated velocity over the pixels in that region. We identified a periodic variation in the flow speed, visible in both the vPA and vUS data. These short bursts of increased blood flow velocity at 150 ms and 700 ms are consistent with arterial flow peaks following cardiac systole.

## 6.4. Discussion and Conclusion

This study demonstrates that the velocity of a random distribution of micron-scale absorbers can be accurately estimated from the PA speckle dynamics in a series of high frame rate images, quantified using the normalized first order field autocorrelation function. In the phantom study, it has been shown that directional velocimetry imaging up to 20 mm/s can be measured with the proposed system and method. The upper limit of velocimetry imaging flow estimation is a function of the PRF of the PLDI and acquisition system.

The particles in the flow phantom were small and had no ultrasound contrast, yet vPA accurately measured the flow speed. Pixel variation in the measured velocities in the phantom may reflect the (parabolic) flow profile with high central velocity and lower values at the borders. Verification of this hypothesis requires the analysis to be robust in the presence of velocity gradients within the pixel, a situation our algorithm does not handle.

We successfully applied vPA to imaging of flow speed in the CAM of a 6-day old chicken embryo. As avian RBCs have good ultrasound contrast due to their size and nucleation [38, 39], vUS measurements validated the measurements. We could visualize the flow in the network. Time resolved vPA and vUS revealed pulsatile flow in the arterial layer of the CAM. Future experiments will be designed to extract blood oxygenation simultaneously using multi-wavelength illumination.

The analysis in its current form still has some details that may be optimized: the approximation of the PSF in the $x$ direction may not be valid in the present geometry, and a sinc function may in fact produce more accurate fits of the complex $g_1(\tau)$. Furthermore, as in many PA experiments, sensitivity is a limitation. The short-time decorrelation ($\tau = 1/2500 = 0.4$ ms) shows an abrupt drop to $|g_1| \approx 0.9$, which can be attributed to uncorrelated noise in the data. Inclusion of such a noise term may improve the quantitative performance of the algorithm. Improved sensitivity would also enable a larger field of view in the PA images, as the fiber-coupled PLDI pulse energy was too low to generate a signal from a large area, precluding the investigation of more complex anatomic flow models. Similarly, small vessels were not visible in PA imaging. Moreover, it is possible to extract vector information and bring the vector flow imaging to the vPA. This method can distinguish the flow directionality in $z$ but not in $x$ due to the square term of $v_x$ in the equation (6.5).

In conclusion, we introduced vPA: quantitative imaging of directional flow using high frame rate PA imaging combined with an analysis of the complex field autocor-

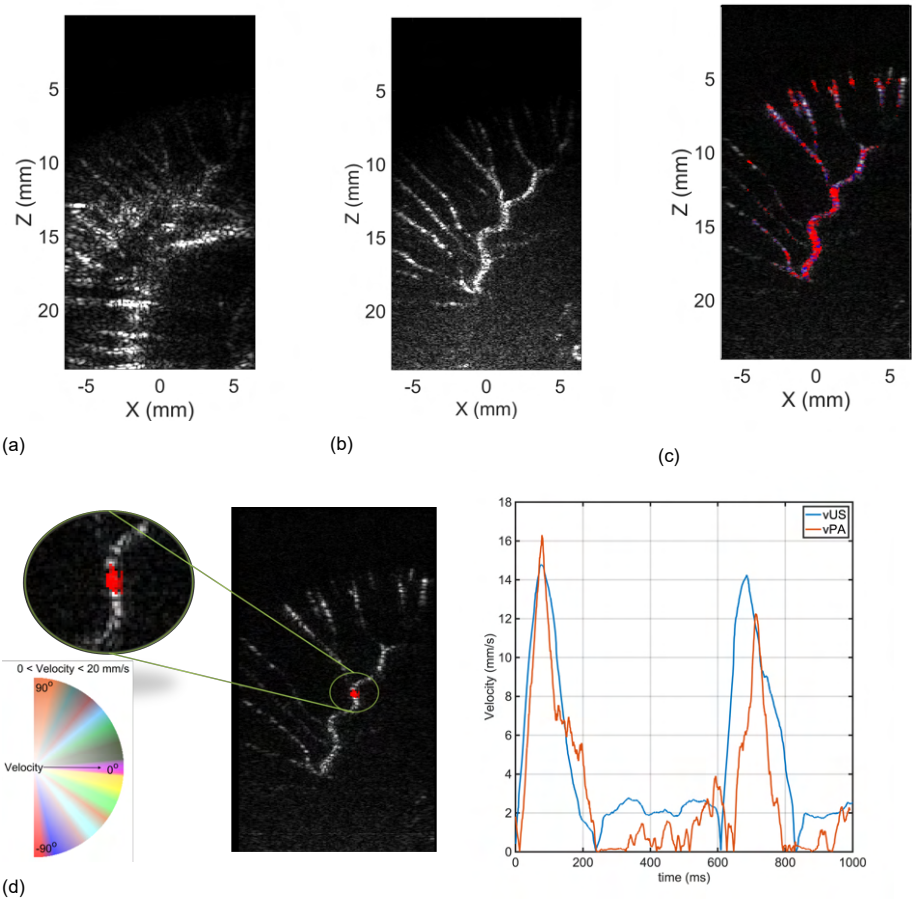


Figure 6.4: **(a)** shows the acquired ultrasound image from the chorioallantoic membrane of the chicken embryo, **(b)** depicts the spatiotemporally SVD filtered ultrasound image, showing the microvasculature; **(c)** Velocimetry imaging of the CAM using ultrasound, and **d** photoacoustic imaging (The vPA and vUS colormap is based on figure 6.3b). **(e)** Comparison of the vPA and vUS in the region where PA signals were recorded, showing pulsatile flow.

relation function. Speed estimation was shown to be numerically accurate on flow speeds up to 20 mm/s. *In vivo* imaging of flow in the CAM of a chicken embryo revealed pulsatile flow in an artery, in agreement with vUS.

## 6.5. Acknowledgment

This work is part of the Vici grant 16131 which is financed by the Dutch Research Council (NWO).

# References

[1] R. Pakdaman Zangabad, S. Iskander-Rizk, P. van der Meulen, B. Meijlink, K. Kooiman, T. Wang, A. F. W. van der Steen, and G. van Soest, *Photoacoustic flow velocity imaging based on complex field decorrelation,* Photoacoustics , 100256 (2021).

[2] T. Wang, T. Pfeiffer, J. Daemen, F. Mastik, W. Wieser, A. F. W. van der Steen, R. Huber, and G. van Soest, *Simultaneous morphological and flow imaging enabled by megahertz intravascular doppler optical coherence tomography,* IEEE Transactions on Medical Imaging **39**, 1535 (2019).

[3] N. Uribe-Patarroyo, M. Villiger, and B. E. Bouma, *Quantitative technique for robust and noise-tolerant speed measurements based on speckle decorrelation in optical coherence tomography,* Optics express **22**, 24411 (2014).

[4] A. H. Kashani, C.-L. Chen, J. K. Gahm, F. Zheng, G. M. Richter, P. J. Rosenfeld, Y. Shi, and R. K. Wang, *Optical coherence tomography angiography: A comprehensive review of current methods and clinical applications,* Progress in retinal and eye research **60**, 66 (2017).

[5] C.-L. Chen and R. K. Wang, *Optical coherence tomography based angiography,* Biomedical optics express **8**, 1056 (2017).

[6] T. E. De Carlo, A. Romano, N. K. Waheed, and J. S. Duker, *A review of optical coherence tomography angiography (octa),* International journal of retina and vitreous **1**, 5 (2015).

[7] L. P. de Isla, J. Zamorano, C. Fernandez-Golfin, S. Ciocarelli, C. Corros, T. Sanchez, J. Ferreirós, P. Marcos-Alberca, C. Almeria, J. L. Rodrigo, *et al.*, *3d color-doppler echocardiography and chronic aortic regurgitation: a novel approach for severity assessment,* International journal of cardiology **166**, 640 (2013).

[8] T. Deffieux, C. Demene, M. Pernot, and M. Tanter, *Functional ultrasound neuroimaging: a review of the preclinical and clinical state of the art,* Current opinion in neurobiology **50**, 128 (2018).

[9] A. Dizeux, M. Gesnik, H. Ahnine, K. Blaize, F. Arcizet, S. Picaud, J.-A. Sahel, T. Deffieux, P. Pouget, and M. Tanter, *Functional ultrasound imaging of the brain reveals propagation of task-related brain activity in behaving primates,* Nature communications **10**, 1 (2019).

[10] R. Rau, P. Kruizinga, F. Mastik, M. Belau, N. de Jong, J. G. Bosch, W. Scheffer, and G. Maret, *3d functional ultrasound imaging of pigeons,* NeuroImage **183**, 469 (2018).

[11] S. Soloukey, A. J.P.E. Vincent, D. D. Satoer, F. Mastik, M. Smits, C. M. F. Dirven, C. Strydis, J. G. Bosch, A. F. W. van der Steen, C. I. de Zeeuw, S. K. E. Koekkoek, and P. Kruizinga, *Functional ultrasound (fus) during awake*

*brain surgery: The clinical potential of intra-operative functional and vascular brain mapping,* Frontiers in neuroscience **13**, 1384 (2020).

[12] Y. He, J. Shi, K. I. Maslov, R. Cao, and L. V. Wang, *Wave of single-impulse-stimulated fast initial dip in single vessels of mouse brains imaged by high-speed functional photoacoustic microscopy,* Journal of Biomedical Optics **25**, 066501 (2020).

[13] H. Fang, K. Maslov, and L. V. Wang, *Photoacoustic doppler effect from flowing small light-absorbing particles,* Physical Review Letters **99**, 184501 (2007).

[14] J. Brunker and P. Beard, *Pulsed photoacoustic doppler flowmetry using time-domain cross-correlation: accuracy, resolution and scalability,* The Journal of the Acoustical Society of America **132**, 1780 (2012).

[15] W. F. Walker and G. E. Trahey, *A fundamental limit on delay estimation using partially correlated speckle signals,* IEEE Transactions on Ultrasonics, Ferroelectrics, and Frequency Control **42**, 301 (1995).

[16] J. Yao, K. I. Maslov, and L. V. Wang, *In vivo photoacoustic tomography of total blood flow and potential imaging of cancer angiogenesis and hypermetabolism,* Technology in cancer research & treatment **11**, 301 (2012).

[17] J. Liang, Y. Zhou, K. I. Maslov, and L. V. Wang, *Cross-correlation-based transverse flow measurements using optical resolution photoacoustic microscopy with a digital micromirror device,* Journal of biomedical optics **18**, 096004 (2013).

[18] J. Yao, L. Wang, J.-M. Yang, K. I. Maslov, T. T. Wong, L. Li, C.-H. Huang, J. Zou, and L. V. Wang, *High-speed label-free functional photoacoustic microscopy of mouse brain in action,* Nature methods **12**, 407 (2015).

[19] M. Sarimollaoglu, D. A. Nedosekin, Y. Simanovsky, E. I. Galanzha, and V. P. Zharov, *In vivo photoacoustic time-of-flight velocity measurement of single cells and nanoparticles,* Optics letters **36**, 4086 (2011).

[20] S.-L. Chen, Z. Xie, P. L. Carson, X. Wang, and L. J. Guo, *In vivo flow speed measurement of capillaries by photoacoustic correlation spectroscopy,* Optics letters **36**, 4017 (2011).

[21] J. Yao, K. I. Maslov, Y. Shi, L. A. Taber, and L. V. Wang, *In vivo photoacoustic imaging of transverse blood flow by using doppler broadening of bandwidth,* Optics letters **35**, 1419 (2010).

[22] C.-W. Wei, S.-W. Huang, C.-R. C. Wang, and P.-C. Li, *Photoacoustic flow measurements based on wash-in analysis of gold nanorods,* ieee transactions on ultrasonics, ferroelectrics, and frequency control **54**, 1131 (2007).

[23] C. Liu, Y. Liang, and L. Wang, *Single-shot photoacoustic microscopy of hemoglobin concentration, oxygen saturation, and blood flow in sub-microseconds,* Photoacoustics **17**, 100156 (2020).

[24] L. Wang, C. Zhang, and L. V. Wang, *Grueneisen relaxation photoacoustic microscopy,* Physical review letters **113**, 174301 (2014).

[25] W. Liu, B. Lan, L. Hu, R. Chen, Q. Zhou, and J. Yao, *Photoacoustic thermal flowmetry with a single light source,* Journal of biomedical optics **22**, 096001 (2017).

[26] J. Tang, D. D. Postnov, K. Kilic, S. E. Erdener, B. Lee, J. T. Giblin, T. L. Szabo, and D. A. Boas, *Functional ultrasound speckle decorrelation-based velocimetry of the brain,* Advanced Science **7**, 2001044 (2020), https://onlinelibrary.wiley.com/doi/pdf/10.1002/advs.202001044 .

[27] J. Tang, S. E. Erdener, S. Sunil, and D. A. Boas, *Normalized field autocorrelation function-based optical coherence tomography three-dimensional angiography,* Journal of biomedical optics **24**, 036005 (2019).

[28] M. Xu and L. V. Wang, *Photoacoustic imaging in biomedicine,* Review of scientific instruments **77**, 041101 (2006).

[29] S. Manohar, A. Kharine, J. G. van Hespen, W. Steenbergen, and T. G. van Leeuwen, *Photoacoustic imaging of blood vessels with a double-ring sensor featuring a narrow angular aperture,* Journal of biomedical optics **9**, 1327 (2004).

[30] Z. Guo, L. Li, and L. V. Wang, *On the speckle-free nature of photoacoustic tomography,* Medical physics **36**, 4084 (2009).

[31] P. Kruizinga, F. Mastik, D. Koeze, N. de Jong, A. F. W. van der Steen, and G. van Soest, *Ultrasound-guided photoacoustic image reconstruction: image completion and boundary suppression,* Journal Of Biomedical Optics **18**, 096017 (2013).

[32] C. Demené, T. Deffieux, M. Pernot, B.-F. Osmanski, V. Biran, J.-L. Gennisson, L.-A. Sieu, A. Bergel, S. Franqui, J.-M. Correas, *et al.*, *Spatiotemporal clutter filtering of ultrafast ultrasound data highly increases doppler and fultrasound sensitivity,* IEEE transactions on medical imaging **34**, 2271 (2015).

[33] B. Meijlink, I. Skachkov, A. F. W. van der Steen, N. de Jong, and K. Kooiman, *The preparation of chicken ex ovo embryos and chorioallantoic membrane vessels as in vivo model for contrast-enhanced ultrasound imaging and microbubble-mediated drug delivery studies,* JoVE , e62076 (2021).

[34] S. J. Madsen, M. S. Patterson, and B. C. Wilson, *The use of india ink as an optical absorber in tissue-simulating phantoms,* Physics in Medicine and Biology **37**, 985 (1992).

[35] T. R. Gregory, *Bird cell sizes,* http://www.genomesize.com/cellsize/birds.htm (2020), accessed March 25, 2020.

[36] B. Cox and P. Beard, *Fast calculation of pulsed photoacoustic fields in fluids using k-space methods,* JOURNAL OF THE ACOUSTICAL SOCIETY OF AMERICA **117**, 3616 (2005).

[37] C. Demené, T. Deffieux, M. Pernot, B.-F. Osmanski, V. Biran, J.-L. Gennisson, L.-A. Sieu, A. Bergel, S. Franqui, J.-M. Correas, *et al.*, *Spatiotemporal clutter filtering of ultrafast ultrasound data highly increases doppler and fultrasound sensitivity,* IEEE transactions on medical imaging **34**, 2271 (2015).

[38] T. C. McQuinn, M. Bratoeva, A. DeAlmeida, M. Remond, R. P. Thompson, and D. Sedmera, *High-frequency ultrasonographic imaging of avian cardiovascular development,* Developmental dynamics: an official publication of the American Association of Anatomists **236**, 3503 (2007).

[39] F. S. Foster, J. Hossack, and S. L. Adamson, *Micro-ultrasound for preclinical imaging,* Interface focus **1**, 576 (2011).

# 7

# Discussion and Conclusion

## 7.1. Overview

This thesis investigates the development of novel transducers and techniques for ultrasound and photoacoustic vascular imaging. The goal in developing new transducer technologies is to increase the fractional bandwidth and transducer sensitivity to provide a better image quality. A novel 96-element Capacitive Micromachined Ultrasonic Transducer (CMUT) based array is designed for Intravascular Ultrasound (IVUS) imaging and is studied for the minimally invasive interventions. Coded excitation imaging is developed for IVUS application and the effect of utilizing the sophisticated signals in combination with broadband CMUT array on the SNR enhancement is investigated. A new probe design based on dual frequency approach is proposed for photoacoustic imaging of the carotid artery where a kerfless PVDF array is used to provide high receive sensitivity over the entire photoacoustic signal band. This thesis proposes a novel quantitative approach for photoacoustic blood flow velocity imaging by estimating the transverse and lateral velocities from the normalized first order field autocorrelation function of moving absorbers.

## 7.2. CMUT based IVUS imaging

In ultrasound array designing, cross-talk of transducer elements can be significant which could narrow the bandwidth and thus affecting the quality of the ultrasound image.

In side-looking intravascular ultrasound imaging, an array of transducers which is wrapped around a catheter tip in a cylindrical configuration is used. In chapter 2 the radiation impedance of un-collapse CMUT arrays operating at 20 MHz center frequency was analyzed. The array was positioned on either a planar rigid baffle or on a cylinder and the element cross-talk was computed using the finite element analysis software package COMSOL Multiphysics.

It is demonstrated that the radiation reactance peaks correspond with dips in the experimentally measured frequency response. The magnitude of these collective resonances in the sensor can be considerable at some frequencies, resulting in different acoustic loading on the CMUT cells which degrade the array performance, since the dips in the frequency spectrum can narrow the transducer bandwidth. The radiation impedance analysis is a powerful tool in studying the array cross-talk.

Chapter 3 presents the world first fabricated CMUT array with 96 elements for side-looking IVUS imaging. It investigates three different topics that are combined to realise the real-time imaging system:

1. Characterization of CMUT array for determining the optimal operating setting
2. Designing coded signal based on the characterization results and IVUS imaging requirements
3. Real-time RF signal acquisition, mismatched filtering, and GPU based beamforming

Based on the characterization results, the flat CMUT array has 130% fractional bandwidth at a center frequency of 19.5 MHz when it is biased at 30 V, where the collapse voltage is 17.5 V and provides 36.8 kPa/V transmit sensitivity. For the rolled-up array; however, only the transmit sensitivity drops to 7.8 kPa/V. The results also indicate that the CMUT array exhibits considerable change in its acoustical behaviour if it is tuned to work in the collapse regime. The broadband frequency response of the CMUT array paves the way for obtaining high quality IVUS images.



Knowing the CMUT sample characteristics, a linear frequency modulation (LFM) or chirp signal with transmit duration time of 300 ns is designed to meet the requirement of <0.5 mm deaf-time for IVUS imaging which also covers the frequency response of the CMUT array. An appropriate mismatch filter based on the received echo signal was designed to compress the received modulated signal and resolve the resolution. Using this technique, 70 μm axial resolution with 8dB gain in SNR is achieved. The axial resolution is slightly degraded in comparison with the single pulse (60 μm ) which is due to the windowing/apodization for lowering the side-lobes associated with decoding the signal.

The pulse compression block may be inserted either after, or before, the beamforming block in the receive chain, as shown in Figure 7.1. The high-complexity receive block diagram was implemented in the imaging chain described in this chapter.

It is obvious that the solution in Figure 7.1a has a lower computational complexity than the configuration in Figure 7.1b. However, the low-complexity configuration which employs a single decoding block instead of n parallel pulse compressors, involves some distorting effects resulting from the dynamic focusing beamforming. The associated error is depth dependent and decreases with increasing depth. These effects are investigated in [1–3], where possible solutions to limit such distortions are also suggested at the cost of more calculation to compensate. The

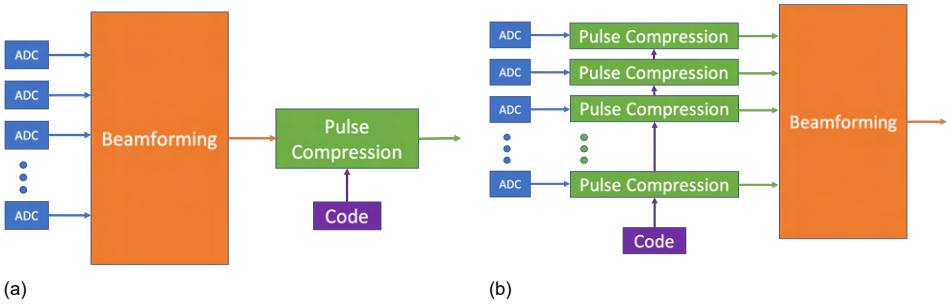


Figure 7.1: **(a)** low complexity receive block diagram (post-compression), **(b)** High-complexity receive block diagram (pre-compression).

suggested low complexity configuration may work for a linear-frequency modulation (LFM) excitation as such a code can be processed without any depth-dependent filter compensation; however, for the binary codes, the post-compression approach might fail to achieve the maximum attainable resolution. Coded excitation offers the possibility to not only control the gain in SNR and compensate for imaging system bandwidth, but also compensation for ultrasound attenuation by utilizing the matched filter in the receive chain of the ultrasound systems.

The ambiguity function of a waveform represents exactly the output of the matched filter when the applied coded signal is used as the filter input. This exact representation makes the ambiguity function a popular tool for designing and analyzing coded waveforms. This approach provides the insight of the resolution capability in both delay and Doppler domains for a given waveform. Based on this analysis, one can then determine whether a waveform is suitable for a particular application. In Appendix A, a brief summary of signal analysis using the ambiguity function is provided.

Analyzing the coded excitation using the ambiguity function provides

In conventional dynamic focusing, the image is created line-by-line using a fixed transmit focus and a dynamic delay-and-sum receive focus which is then scan-converted to create virtual lines, to be interpolated in between the actual lines. This interpolation does not increase the information content of the image and just smooths out the image for human perception. A pixel based beam-forming algorithm to achieve an optimal lateral resolution was adopted to improves spatial resolution by lowering the interpolation artifacts. A system with 20 frame per second real-time and pixel-based beam-formed phased-array IVUS images was developed and the feasibility of intravascular ultrasound chirp imaging of human coronary atherosclerosis using the CMUT array is demonstrated.

### 7.2.1. Limitations

The imaging scheme that transmits on all elements and detects on consecutive triplets can potentially be improved. Selective excitation of transmission elements could improve the lateral resolution in the images, but this is currently not supported

by the electronics. Furthermore, due to the limitation in the electronics, the maximum output pressure generated with the rolled-up CMUT array at 30 V DC biasing is around 80 kPa while normally the other commercialized catheters, both single element and phased array, can generate 500 kPa at least. Further development in the ASIC and the associated electronics is required to pave the way for introducing the first CMUT IVUS catheter.

For waveforms with quadratic-phase modulation where the carrier frequency is stepped linearly, like LFM or chirp, it is demonstrated that echos from chirp signals can be processed without any depth-dependent filter compensation to retain the quality of the decoded signals [4–6]. Consequently, it makes the processing less complicated. Phase-based binary codes like Golay and Barker codes have limited utility in ultrasound imaging, as the abrupt change in the phase of the coded signals produces higher harmonics which are beyond the transducer bandwidth. Since any ultrasound transducer acts as a band-pass filter, frequencies above the upper limit of the transducer frequency response are poorly transmitted, leading to imperfect encoding which rise up the side lope levels. On the other hand, it is known that the Barker codes produce the minimum side lobe level in comparison with other coded signals. Considering the CMUT array bandwidth, the usability of these binary codes in CMUT based ultrasound imaging can be investigated.

We presented a novel concept for IVUS that exploits broad bandwidth offered by the CMUTs. We characterized the array performance for coded excitation imaging which may be useful for achieving greater penetration depth in IVUS while maintaining image resolution. CMUTs are manufactured using micromachining techniques which are evolved from the well-established integrated circuit fabrication process and possess unique potential in high yield mass production of CMUT-based IVUS catheters. Consequently, this technique offers an opportunity to lower the production costs.



## 7.3. Probe Designing

Photoacoustic signals can have very large bandwidth and large dynamic range. Transducers with high bandwidth can significantly improve the sensitivity of the photoacoustic imaging [7]. A simple approach in array designing is presented in chapter 4. The off-resonance transducer doesn't require to have complex ASIC to compensate for the phase change around their resonance frequency; consequently, a simple impedance matching circuit with an amplifier satisfies the SNR requirement. Moreover, a less complex, kerfless array is shown to have acceptable crosstalk level (-30 dB) between the elements making the off-resonance kerfless PVDF array a broadband, high sensitivity receiver which can significantly improve the detection of PA signals.

The proposed array is used in designing a dual frequency photoacoustic probe presented in chapter 5. It is shown that by considering the kerfless PVDF array as a second matching layer of the PZT-5H ultrasound stack, the fractional bandwidth of the array increases by $\cong 40\%$.

In order to increase the transmit sensitivity of the dual frequency probe, some optimizations need to be performed. In transmit mode, the conductive glue, the aluminium foil which acts as a ground for the kerfless PVDF array above, and the PVDF array with appropriate window material for making it water-tight load the PZT-5H. Consequently, the $\lambda/2$ design approach for choosing the PZT-5H thickness (thickness mode vibration) is not valid. Due to the mechanical loading of the all layers, the designed resonance frequency is lower than the intended one. Thus, an optimization is required to find the right PZT-5H thickness which happens between the $\lambda/3$ and $\lambda/2$.

Considering the receive part, all the layers beneath the PVDF act as backing layers. The purpose of the backing layer is to provide mechanical stability and also to absorb the pressure waves generated by the acoustic stacks and plays an important role in the resonance frequency and bandwidth of the transducer. In order to obtain a Gaussian shaped pressure pulse with a broader bandwidth, the acoustic impedance of the backing layer can be designed to be the same as the matching layer [8]. The acoustic impedance of the backing layer is inversely proportional with the resonance frequency. Thus, an increase in the acoustic impedance yields frequency down shift of the acoustic stack. In the presented design, the equivalent acoustic impedance of the all layers is much higher than the PVDF and water which eventuates in frequency down shift of the received photoacoustic signal. This might be in favour of the targeted application since most of the photoacoustic signal energy is at lower frequencies. However, in order to extend the design for intravascular photoacoustic imaging [9, 10], the backing effect might degrade the PA receive part. Therefore, a co-optimization of the transmit and receive part is necessary to be able to use the benefits of the broadband PVDF layer and the proposed design offer.

One of the approaches in realizing the probe is to build it on a PCB. Based on the design parameters summarized in Table 5.2 and by considering the pitch size and the elevation width, a 5 cm ×5 cm PCB has been designed to build the acoustical stacks upon. The PCB track width and kerf are 100 μm making 200 μm pitch size. A PZT slab with 1 cm ×1 cm would fit on the alignment marks. Figure 7.2a shows the schematic of the PCB and Figure 7.2b is the manufactured PCB and its traces. Since the PCB surface is not smooth and flat, for the probe realization, a conductive epoxy was applied on the PZT area, and the PZT slab was placed and then was cut through using a dicing saw. Manufacturing the proposed dual frequency array was difficult. Using the dicing saw, the epoxy probably didn't cut through properly resulting in the traces to be connected to each other and making short cuts. Increasing the depth of cutting seemed to be helpful; however, it resulted in cutting the traces that are not in parallel to the saw. A precise controlling of the dicing saw was required to realize the probe.

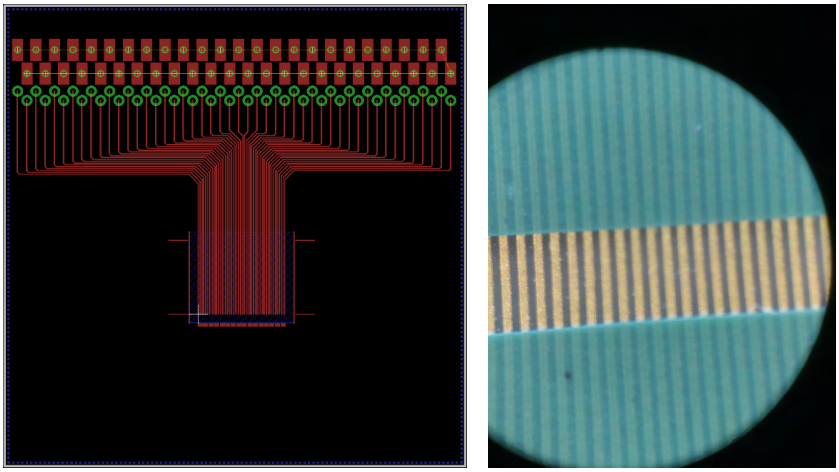

(a) (b)

Figure 7.2: **(a)** Schematic view of the designed PCB for the dual frequency probe, **(b)** a view on the manufactured PCB traces.

## 7.4. Photoacoustic Flow Velocimetry Imaging

Chapter 6 introduces a novel photoacoustic flowmetry method based on complex field decorrelation. Using an ink tube as a phantom and the chorioallantoic membrane (CAM) of a chicken embryo as imaging targets, we validated the proposed method *in vitro* and *in vivo*.

Extracting the blood oxygenation level is one of the advantages of PA imaging. The choice of the laser wavelength was made to address this need. We are planning to incorporate a second pulsed diode laser with 940 nm wavelength and perform the multispectral excitation for demonstrating the concept in the near future. The PA signal is relatively weak in comparison with the US signal. The coupling efficiency of the laser to the fiber is 50 % at the moment. By redesigning the optical components used to confine the beam and better alignment, the coupling efficiency can be increased and more power can be delivered to samples.

If the laser pulse is too long for satisfying the stress confinement but is short enough for thermal confinement, the generated pressure due to the longer pulse can be approximated by the temporal convolution of the deposited heat which is modeled as a delta function and the laser pulse shape [11]. The Fourier transform of the convolution is the Fourier transform of the Gaussian shape laser pulse which has the bandwidth equal to twice of the laser pulse width. For a Gaussian pulse, the relation between the $\tau$ and FWHM width (34 ns) is: $T_{FWHM} = \sqrt{2ln(2)} \times \tau$ Thus, $\tau$ =28.8 ns and the upper frequency limit can be approximated by $1/(2 \times \tau) \cong$ 17 MHz. In order to increase the PA signal sensitivity, using a probe with center frequency around 12 MHz might help to cover the PA frequency contents; however, lowering the center frequency decreases the ultrasound image resolution. Consequently, imaging the CAM of a 6-day old chicken embryo and the blood velocities inside the vessels

might not feasible with this laser as an excitation source. Utilizing the dual frequency probe which is proposed in chapter 5 with tuning the PA receive stack to cover the required bandwidth or using a broadband CMUT probe will enhance the sensitivity of the PA signal. Moreover, utilizing laser sources with narrower pulse width such that the laser pulse width would be longer than half the inverse of the top of the transducer band help to satisfy the stress confinement and consequently increase the PA signals frequency components.

We compared the flow measured by PA and US, showing the pulsatile flow. In systolic event where heart pumps out the blood, the number of RBCs (US scatterers/PA sources) passing through arteries increases. Consequently, it gives a rise in the intensity of the SVD filtered data. After removing the clutter using the SVD filtering from the ultrasound data of the chicken embryo which was acquired for one second, we saw two velocity peaks in the flow during the 1 s acquisition time, which we identified as heart beats. We didn't separately measure the heartbeat.

The vPA can distinguish the ascending and descending flow directionality but not in lateral direction due to the square term of $v_x$ in $g_1(\tau) = e^{-\left(\frac{v_x\tau}{2\sigma_x}\right)^2-\left(\frac{v_z\tau}{2\sigma_z}\right)^2} e^{ik_0 v_z \tau}$ (equation (6.6)). Utilizing other methods such as differential phase [12, 13] which is based on the acquired RF raw data successfully extracts the flow vector parameters.

One of the big challenges associated with quantitative methods for flow estimation, is the motion artefacts which necessitate motion compensation. The presence of motion induced by tissue, or moving probe, and out of plane motion impairs or decreases the accuracy of vPA. Utilizing 2D probes for 3D ultrasound and photoacoustic imaging can be helpful for motion correction [14]. However, the acquisitions are computationally more demanding and have a lower spatiotemporal resolution.

The maximum detectable flow speed is dictated by the PRF of the imaging system, and the minimum flow speed depends on the system SNR. In conclusion, the vPA flow speed estimation is accurate on flow speeds up to 20 mm/s.

# References

[1] R. Y. Chiao and X. Hao, *Coded excitation for diagnostic ultrasound: A system developer's perspective,* IEEE transactions on ultrasonics, ferroelectrics, and frequency control **52**, 160 (2005).

[2] R. Bjerngaard and J. A. Jensen, *Should compression of coded waveforms be done before or after focusing?* in *Medical Imaging 2002: Ultrasonic Imaging and Signal Processing*, Vol. 4687 (International Society for Optics and Photonics, 2002) pp. 47–58.

[3] A. Polpetta and P. Banelli, *Design and performance of huffman sequences in medical ultrasound coded excitation,* IEEE transactions on ultrasonics, ferroelectrics, and frequency control **59**, 630 (2012).

[4] T. Misaridis, *Ultrasound imaging using coded signals* (Ørsted DTU, Electronics & Signal Processing, 2001).

[5] T. Misaridis and J. A. Jensen, *Use of modulated excitation signals in medical ultrasound. part i: Basic concepts and expected benefits,* IEEE transactions on ultrasonics, ferroelectrics, and frequency control **52**, 177 (2005).

[6] T. Misaridis and J. A. Jensen, *Use of modulated excitation signals in medical ultrasound. part ii: design and performance for medical imaging applications,* IEEE Transactions on Ultrasonics, Ferroelectrics, and Frequency Control **52**, 192 (2005).

[7] V. Daeichin, M. Wu, N. De Jong, A. F. W. van der Steen, and G. van Soest, *Frequency analysis of the photoacoustic signal generated by coronary atherosclerotic plaque,* Ultrasound in medicine & biology **42**, 2017 (2016).

[8] C. S. Desilets, J. D. Fraser, and G. S. Kino, *The design of efficient broadband piezoelectric transducers,* IEEE Transactions on sonics and ultrasonics **25**, 115 (1978).

[9] K. Jansen, A. F. W. van Der Steen, H. M. M. van Beusekom, W. J. Oosterhuis, and G. van Soest, *Intravascular photoacoustic imaging of human coronary atherosclerosis,* Optics letters **36**, 597 (2011).

[10] J. Hui, Y. Cao, Y. Zhang, A. Kole, P. Wang, G. Yu, G. Eakins, M. Sturek, W. Chen, and J.-X. Cheng, *Real-time intravascular photoacoustic-ultrasound imaging of lipid-laden plaque in human coronary artery at 16 frames per second,* Scientific reports **7**, 1 (2017).

[11] B. Cox and P. Beard, *Fast calculation of pulsed photoacoustic fields in fluids using k-space methods,* JOURNAL OF THE ACOUSTICAL SOCIETY OF AMERICA **117**, 3616 (2005).

[12] P. Kruizinga, F. Mastik, J. G. Bosch, N. de Jong, A. F. W. van der Steen, and G. van Soest, *Measuring submicrometer displacement vectors using high-frame-rate ultrasound imaging,* IEEE transactions on ultrasonics, ferroelectrics, and frequency control **62**, 1733 (2015).

[13] S. Iskander-Rizk, R. Pakdaman Zangabad, P. Kruizinga, A. F. W. van der Steen, and G. van Soest, *Differential phase analysis for high frame rate photoacoustic vector flow imaging,* imaging **1**, 2 (2021).

[14] Q. Huang and Z. Zeng, *A review on real-time 3d ultrasound imaging technology,* BioMed research international **2017** (2017), 10.1155/2017/6027029.

# A

# Appendix-Signal analysis using the ambiguity function

A

## A.1. Signal analysis using the ambiguity function

A modulated waveform can be expressed with complex notation as:

$$s(t) = a(t)\, e^{j\Phi(t)}$$
$$\Phi(t) = 2\pi f_0 t + \psi(t) \tag{A.1}$$

where $a(t)$ and the $\Phi(t)$ are the modulated amplitude and phase function, respectively. $f_0$ is the baseband transmit frequency with initial phase $\psi(t)$.

This signal will be applied to ultrasound transducer to generate the pressure field. Thus, the output pressure at the transducer surface ($p(t)$) is the convolution of the waveform ($s(t)$) with the transducer temporal impulse response ($h_t(t)$).

$$p(t) = s(t) * h_t(t) \tag{A.2}$$

The ultrasound pressure will travel and echoes back from reflectors and scatterers. For simplicity, let's assume a single scatterer whose round-trip distance from the transducer is $\vec{r}$. The received signal $r(t)$ is the attenuated and time-shifted version of the convolution between the transmitted pressure signal p(t) and the spatial impulse responses of the transducer, $h_s(t,\vec{r})$).

$$r(t) = p(t-\tau_0) * h_s(t,\vec{r}) + \mu(t)$$
$$= s(t-\tau_0) * h_t(t) * h_s(t,\vec{r}) * h_{att}(t,\vec{r}) + \mu(t) \tag{A.3}$$

where $\tau_0 = |\vec{r}|\,/c$ is the round-trip delay when $c$ is the ultrasound velocity in the tissue, $*$ is the convolution operator, $h_{att}(t,\vec{r})$ is the frequency dependant attenuation and $\mu(t)$ represents the system noise.

$h_{att}(t,\vec{r})$ is the inverse Fourier transform of $H_{att}(f,\vec{r})$, whose dependence on the frequency $f$ is typically expressed by [1, 2]:

$$H_{att}(f,\vec{(r)}) = e^{-\alpha|\vec{r}|} e^{-\beta(f-f_0)|\vec{r}|} e^{-j2\pi f(\tau_b+\tau_m(\beta/\pi^2)|\vec{r}|)} e^{j2(f/m)\beta|\vec{r}|ln(2\pi f)} \tag{A.4}$$

where $\tau_b = 1/c$ is the bulk propagation delay per unit length, $\tau_m$ is the minimum phase delay factor, and $\alpha$ and $\beta$ are the coefficients associated with the frequency-independent and frequency-dependent attenuation, respectively. it is suggested that the effect of a frequency-dependent attenuation can be approximated by a frequency down-shift of the transmitted signal [2–7], as expressed by:

$$r(t) \approx e^{-\alpha|\vec{r}|} s(t-\tau_0) e^{j2\pi[-f_d(t-\tau_0)]} + \mu(t) \tag{A.5}$$

where, for a transmitted pulse with relative bandwidth $B_r$, the frequency shift $f_d$ induced by the frequency-dependent attenuation is usually approximated by [3]:

$$f_d = \beta B_r^2 f_0^2 |\vec{r}| \tag{A.6}$$

The received pressure signals will be converted to electric signals by the transducer. Consequently, the convolution of the r(t) with the transducer impulse response will be the received electric signals. If the transducer is broadband like

CMUT, its time impulse response can be approximated by a Gaussian shape and its autocorrelation function is also a Gaussian and can be modeled as an apodization k:

$$\begin{aligned} v(t) &\approx r(t) * h_t(t) \\ &\approx k(t)e^{-\alpha|\vec{r}|}s(t-\tau_0)e^{j2\pi[-f_d(t-\tau_0)]} + \mu(t) \end{aligned} \tag{A.7}$$

Match filtering is a tool for decoding the signal and has an impulse response equal to the input waveform with reversed time axis.

$$d(t) = v(t) * s(\tau_d - t)^* \tag{A.8}$$

Substituting the returned signal given in Equation A.7 and the filter impulse response into Equation A.8, we get the receiver output:

$$\begin{aligned} d(t) &\approx \int_{-\infty}^{\infty} (e^{-\alpha|\vec{r}|}s(t-\tau_0)s(\tau+t)e^{j2\pi[-f_d(t-\tau_0)]} + \mu(t)s(\tau+t))dt \\ &\approx e^{-\alpha|\vec{r}|}\chi(\tau, f_d) + R_{\mu s}(t) \end{aligned} \tag{A.9}$$

where $\chi(\tau, f_d)$ is defined as *ambiguity function*:

$$\chi(\tau, f_d) = \int_{-\infty}^{\infty} s(t).s(t-\tau)^* e^{-j2\pi f_d t} dt \tag{A.10}$$

and $R_{\mu s}$ is the colored noise.

Moreover, for moving targets, there is an additional Doppler shift. For instance, in imaging the blood flow velocities, the moving particles inside the blood with the velocity $v_b$ of induces an additional frequency shift which depends on the ultrasound velocity $v_u$ , and on the angle $\theta$ between the direction of the flow and the ultrasound beam:

$$f_d = 2f_0 \frac{v_b}{v_u} \cos(\theta) \tag{A.11}$$

If the delay $(\tau)$ is translated so that the maximum occurs at $\tau = 0$ and the frequency is translated such that the matching occurs at $f_d = 0$, meaning that there would be no Doppler and frequency down shift, the ambiguity function becomes the matched filter response. The value of the ambiguity function at point $(\tau; f_d)$ away from the origin shows the response of mismatched filter. Moreover, any weighting of the match filter which results in widening of the ultrasound beam is also called mismatched.

Figure A.1 shows the 2D contour plot of the 300 ns LFM signal's ambiguity function which is calculated based on LFM (Equation 3.1) and Equation A.10. It has a time-bandwidth product of $B \cdot T = 7$. The zero-Doppler cut in the ambiguity function will provide the auto-correlation of the input signal. Figure A.2 shows the zero-Doppler cut from the ambiguity function which is compared with the envelope of the

A

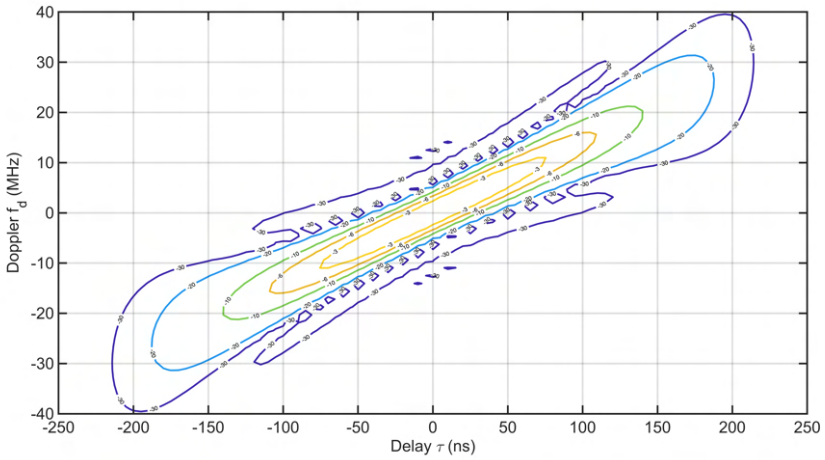


Figure A.1: 2D contour plot of the ambiguity function of a linear FM signal

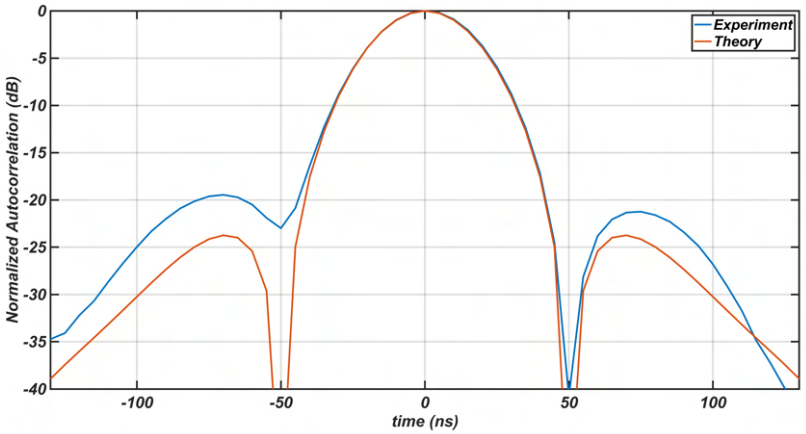


Figure A.2: 2D contour plot of the ambiguity function of a linear FM signal

mismatched filter output (Figure 3.6b bottom graph). It shows that he first null happens at approximately 50 ns meaning that the resolution of the ultrasound system with the designed LFM will be around 75 μm. In the presence of frequency dependent attenuation, LFM signals have the most robust performance in terms of SNR improvement [3] and the effect of frequency downshift is translated to time delay.

Figure A.3 shows that the frequency attenuation leading to a 2 MHz frequency downshift still provides the first null at 50 ns of the peak, meaning that the resolution is preserved.

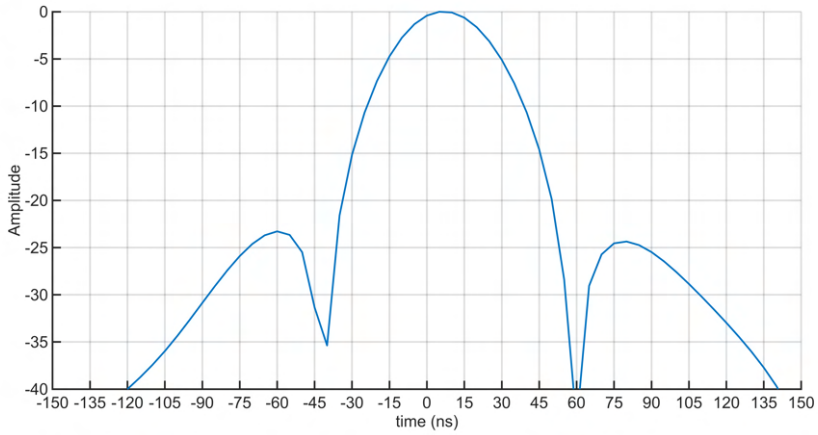


Figure A.3: Doppler cut at 2 MHz of the LFM ambiguity function

A

# References

[1] J. A. Jensen, D. Gandhi, and O. WD Jr, *Ultrasound fields in an attenuating medium,* in *1993 Proceedings IEEE Ultrasonics Symposium* (IEEE, 1993) pp. 943–946.

[2] K. Gurumurthy and R. M. Arthur, *A dispersive model for the propagation of ultrasound in soft tissue,* Ultrasonic Imaging **4**, 355 (1982).

[3] T. Misaridis and J. A. Jensen, *Use of modulated excitation signals in medical ultrasound. part i: Basic concepts and expected benefits,* IEEE transactions on ultrasonics, ferroelectrics, and frequency control **52**, 177 (2005).

[4] T. Misaridis and J. A. Jensen, *Use of modulated excitation signals in medical ultrasound. part ii: design and performance for medical imaging applications,* IEEE Transactions on Ultrasonics, Ferroelectrics, and Frequency Control **52**, 192 (2005).

[5] P. Narayana, J. Ophir, and N. Maklad, *The attenuation of ultrasound in biological fluids,* The Journal of the Acoustical Society of America **76**, 1 (1984).

[6] J. A. Jensen, *Estimation of blood velocities using ultrasound: a signal processing approach* (Cambridge University Press, 1996).

[7] T. X. Misaridis, M. H. Pedersen, and J. A. Jensen, *Clinical use and evaluation of coded excitation in b-mode images,* in *2000 IEEE Ultrasonics Symposium. Proceedings. An International Symposium (Cat. No. 00CH37121)*, Vol. 2 (IEEE, 2000) pp. 1689–1693.

# Curriculum Vitæ

## Reza Pakdaman Zangabad

Reza Pakdaman Zangabad received his B.Sc. degree in Electrical and Computer Engineering/Electronics from the University of Tabriz, Iran in 2010 and his M.Sc. degree in Electronics Engineering from Sabanci University, Istanbul, Turkey in 2014 where he performed research on CMUT based ultrasound imaging systems and heat energy harvesting using thermoelectric and thermophotovoltaic cells in collaboration with Lockheed Martin. He joined the Biomedical Engineering group at Erasmus MC university medical center Rotterdam, The Netherlands in 2015 as a Ph.D. candidate and collaborated with Philips Research to realize the first-ever cylindrical CMUT phased array for IVUS imaging. His research activities include CMUT based ultrasound systems, transducer and probe developments, Photoacoustics, and ultrasound/PA system development for different imaging applications.

He is currently working as a scientific researcher at Georgia Institute of Technology, where he is continuing and expanding his research on system engineering for transcranial focused ultrasound using CMUT arrays.

# List of Publications

## Peer reviewed papers

1. **Reza Pakdaman Zangabad**, Johan G. Bosch, Frits Mastik, Robert H. S. H. Beurskens, Vincent A. Henneken, Johannes W. Weekamp, Antonius F. W. van der Steen, Gijs van Soest, *Real-Time Coded Excitation Imaging Using a CMUT-based Side Looking Array for Intravascular Ultrasound*, EEE Transactions on Ultrasonics, Ferroelectrics, and Frequency Control (**2021**).
2. **Reza Pakdaman Zangabad**, Sophinese Iskander-Rizk, Pim van der Meulen, Bram Meijlink, Klazina Kooiman, Tianshi Wang, Antonius F. W. van der Steen, Gijs van Soest, *Photoacoustic flow velocity imaging based on complex field decorrelation*, Photoacoustics: 100256 (**2021**).

## Conference proceedings

1. Sophinese Iskander-Rizk, **Reza Pakdaman Zangabad**, Pieter Kruizinga, Antonius F. W. van der Steen, Gijs van Soest, *Differential phase analysis for high frame rate photoacoustic vector flow imaging*, SPIE BIOS, Photon plus ultrasound: Imaging and Sensing, 11642, (**2021**).
2. **Reza Pakdaman Zangabad**, Hendrik J. Vos, Nico de Jong, Antonius F. W. van der Steen, Gijs van Soest, *Design of a Dual Frequency Probe for Photoacoustic Imaging of the Carotid Artery*, 2020 IEEE International Ultrasonics Symposium (IUS), IEEE, (**2020**).
3. **Reza Pakdaman Zangabad**, Geert Springeling, Emile Noothout, Robert H. S. H. Beurskens, Nico de Jong, Antonius F. W. van der Steen, Gijs van Soest, Verya Daeichin, *A Kerfless PVDF Array for Photoacoustic Imaging*, 2018 IEEE International Ultrasonics Symposium (IUS), IEEE, (**2018**).
4. **Reza Pakdaman Zangabad**, Ayhan Bozkurt, Göksenin Yaralıoğlu, Johan G. Bosch, Gijs van Soest, Antonius F. W. van der Steen, *Mutual radiation impedance of circular CMUTs on a cylinder*, 2016 IEEE International Ultrasonics Symposium (IUS), IEEE, (**2016**).

# PhD Portfolio

| Courses | Place | year | ECTs |
|---|---|---|---|
| Advanced ultrasound imaging (Summer School) | Danish Technical University, Copenhagen, Denmark | 2015 | 2.5 |
| COEUR Cardiovascular imaging and diagnostics | Erasmus MC, Rotterdam, the Netherlands | 2015 | 1.5 |
| English biomedical writing and communication | Erasmus MC, Rotterdam, the Netherlands | 2016 | 4 |
| Motion Estimation Algorithms in Ultrasound Imaging: Principles and hands-on development | 2018 IEEE IUS, Kobe, Japan | 2018 | 0.2 |
| Biomedical Photoacoustics: from bench to bedside | 2018 IEEE IUS, Kobe, Japan | 2018 | 0.2 |
| COEUR Congenital cardiology in children and adults | Erasmus MC, Rotterdam, the Netherlands | 2018 | 0.5 |
| COEUR solving the mysteries of atrial fibrillation: from basic science to clinical practice | Erasmus MC, Rotterdam, the Netherlands | 2018 | 0.5 |
| Scientific integrity (Virtual, via Zoom) | Erasmus MC, Rotterdam, the Netherlands | 2020 | 0.3 |
| **Workshops and Seminars** | | | |
| COEUR PhD Day | Erasmus MC, Rotterdam, the Netherlands | 2015 | 0.6 |
| Micromachined Ultrasound transducer | Dresden, Germany | 2015 | 0.6 |
| Micromachined ultrasound transducer | Rome, Italy | 2016 | 0.6 |
| INCITE Workshop | Rotterdam, the Netherlands | 2016 | 0.9 |
| INCITE Workshop | Levi, Finland | 2017 | 0.9 |
| INCITE Workshop | Lyon, France | 2018 | 0.9 |
| Micromachined ultrasound transducer (oral) | Ajaccio, France | 2018 | 1.2 |
| iMIT meeting | Delft, the Netherlands | 2018 | 0.3 |
| COEUR PhD Day | Erasmus MC, Rotterdam, the Netherlands | 2019 | 0.3 |
| NVMU Autumn meeting (oral) | Delft, the Netherlands | 2019 | 0.55 |
| **Symposium and congress** | | | |
| Optics in cardiology | Rotterdam, the Netherlands | 2015 | 0.6 |
| Artimino Conference (oral) | Helsinborg, Sweden | 2015 | 3.1 |
| IEEE International Ultrasound Symposium (poster) | Taipe, Taiwan | 2015 | 1.9 |

| | | | |
|---|---|---|---|
| International conference on Ultrasonic Biomedical Microscanning | Kralendijk, Bonaire, The Netherlands | 2016 | 3.1 |
| Ultrasound contrast agents symposium | Rotterdam, the Netherlands | 2016 | 0.6 |
| Optics in cardiology | Rotterdam, the Netherlands | 2017 | 0.6 |
| IEEE International Ultrasound Symposium (poster) | Tours, France | 2017 | 1.9 |
| Ultrasound contrast agents symposium | Rotterdam, the Netherlands | 2017 | 0.6 |
| IEEE International Ultrasound Symposium (poster) | Kobe, Japan | 2018 | 1.9 |
| Medical Imaging Symposium for PhD students | Rotterdam, the Netherlands | 2018 | 0.3 |
| Ultrasound contrast agents symposium | Rotterdam, the Netherlands | 2019 | 0.6 |
| IEEE International Ultrasound Symposium (oral) | Glasgow, Scotland | 2019 | 3.1 |
| Ultrasound contrast agents symposium | Rotterdam, the Netherlands | 2020 | 0.6 |
| IEEE International Ultrasound Symposium (Poster, Virtual, via Zoom) | Las Vegas, United States | 2020 | 3.1 |
| | | **Total** | **38.55** |

# Acknowledgements

This book, which you are currently holding in your hands, is not the work of a single person. It is the result of many people's combined efforts and teamwork.

First and foremost, I want to express my gratitude to my family for encouraging me to pursue higher education and follow my goals. Thank you for your efforts and for respecting my choices, Mom and Dad. I can't imagine how difficult these years were for you. I owe everything to you. Getting this Ph.D. costed me a lot, and I had to miss Grandma and Grandpa's funeral. **Saba**, my lovely sister, I missed you a lot. It was extremely difficult for me to leave you; however, I am grateful that you accepted my decision. I admire you for being a bookworm. I am waiting for you to get your B.Sc. degree and to join me. I also would like to thank **Zahra**, for sparing your time with me, and for all the good memories we have. **Nadereh**, if only you were among us to celebrate these days.

I would like to express my gratitude to **Ton** and **Gijs**, my promotors. **Ton**, thank you for offering me the PhD position in the BME group. It was great to work in such an inspiring environment with so much knowledge and great colleagues. I learnt a lot from the way you look at problems, graphs, data, pinpointing hidden details, and also your management style. I still remember the interview day with me and you asked me if I could play any instrument which was a great incentive and made me to think about how to develop myself and now, I can play a guitar.

**Gijs**, thank you for our discussions throughout these years. I appreciate the freedom and space you provided me during my PhD, which helped me to become an independent researcher. Despite the very complex INCITE project environment which made me to maneuver between the desire to publish and confidentiality, I am happy that I made a right decision and extended my research in photoacoustic field. I also admire your broad knowledge on variety of subjects. Our discussion on the ambiguity function and possibilities of utilizing it to analyze the coded excitations in lasers were so exciting to me! You've also helped me in shaping my propositions to the point where I actually meant showing how well you know me and my personalities, and I am grateful to have you as an advisor.

**Hans**, thanks a lot for your time in supervising me when Gijs was on his sabbatical. I was developing the CMUT IVUS system and nearly every day, I was receiving your feedback on what to consider and avoid in implementing the codes. I would not have been able to deliver the system three months ahead of the schedule without your assistance. I also appreciate the IVUS beamforming trick you shared with me, which resulted in significant lateral resolution improvement. I also learnt a lot on how to properly shape the conclusion and discussion of the IEEE IUS proceeding which I applied to the rest of my manuscript. Thank you again for representing me at the INCITE consortium meeting in Budapest so that I could plan my wedding.

**Frits**, thanks a lot for your time in helping me to develop the CMUT IVUS system. It was so great to have the possibility to use your expertise regarding the IVUS system engineering with an expert that has worked with this technology from its early developments. Our technical and scientific discussions on different topics in late evening at the wet lab (the cave!) were so valuable and unique. I am really lucky to have you around.

**Robert**, you are an amazing person, engineer, and a great listener. I appreciate taking the time for listening to my concerns and providing advises. Finishing the experiments and

the Ph.D. wouldn't have been possible without you. All the time, something went wrong before the experiment began, and you were the one who saved the effort and days or months of preparations. Thank you for assisting me to fill out the Belastingdienst forms in my first year, with the Dutch summary of my thesis, driving all the way to Eindhoven to take my system and being such a good company. I am happy that you let me to use your skills and having your right mind when you had no mind left!

**Ayhan**, you are a great advisor, fantastic coach, great leader and the most amazing person I have seen so far. You reuse the old electronics equipment which you find in the dedicated recycle box which bunch of them are lying on your desk like, a speaker and an FM receiver you made, making your own drinks, passionate about science and I wish one day I will be like you. You have the whole knowledge in ultrasound engineering chain, from analytical and FEM modeling, transducer fabrication and characterization to ASIC designing. I have tried to gain all the knowledge during my PhD but still I am missing the ASIC part. Thank you for accepting me to your group and being there for me during my difficult time and for continuing to support me financially when I was a little depressed. You showed concern for my mental health by recommending movies and books, and you gave me a month to discuss my point of view and gain a better understanding during our weekly progress meetings while you were still paying me. Finishing my M.Sc. and pursuing my academic career wouldn't have been possible without your support and I really appreciate.

**Nico**, I have been impressed by your passion for ultrasound transducers and I have enjoyed our discussion regarding different designs and technical solutions. **Rik**, Thanks a lot for explaining the physics behind ultrasound transducer designing, our discussions related to the dual-frequency array, and on the correlation of random processes, checking my poster and presentation and also for the high frequency probe you provided me.

Thanks to Philips team in Eindhoven for making the CMUT devices, **Vincent Henneken, Frank Budzelaar, Joanneke Groen**, and **Jeannet van Rens** for your time and also your support in the EMC test.

Thank you to **Gracia**, and **Rita** for arranging all the paperwork and **Sharon** for helping me with all the administrative paperwork regarding the resident permit.

**Gerard**, thanks for being so kind, dealing with my excessive request on upgrading my PCs and laptop, sharing stories about your diving adventures, and lately sharing the office.

**Charles**, I was astounded when I read your MATLAB scripts about modeling the INCITE-IVUS device and saw how you used hyperbolic functions to define the geometries. Thank you for sharing your tricks with me, and may you rest in peace.

Thank you **Tianshi** and **Pim** for being wonderful colleagues and friends. I consider **Tianshi** as my friend, and guide with an amazing personality and human qualities. You made the work environment to be fun. Thanks also for your help late evening with sharing your view on cross-correlations. **Pim**, I believe despite coming from different cultures, we have a lot of common views. Our life philosophy, sense of humor, our expectations, and the fact that we understand each other even without talking is unique. Thanks also for your help in formulating the normalized first order autocorrelation function. Our tough moments happened in the same time and we support each other to overcome the obstacles that made our friendship unique. Both of you were there with me for all the ups and downs during the last couple of years and I am really blessed to have you as my friends.

I also would like to thanks our **little Bonaire group**, **Sophinèse, Jovana**, and **Martin** with whom I had lots of fun. May it be in a conference, or a summer school, we all enjoyed our companion and sense of humor. Thanks for screaming with me for the ice cream! **Sophinèse**, you are a nice person, and a good listener. We had a lot of hassles during the Ph.D. and helped each other to find a solution for our technical/policy challenges. Lately

you were involved in the vPA experiment and helped me in the optical setup, the Verasonics codes and stayed till late evening to help with my challenges. Thanks also for remembering everyone's birthday and taking the lead in organizing parties. I really admire your attitude and I really enjoyed our talks. **Jovana**, your hard-working attitude set the right tone and thanks for the good vibes in the office and nice chats in the **"cave"**. **Martin**, thanks for sharing your CMUT characterization experiment with me and also bringing Czechish special gift all the way to Bonaire! The conferences and our gathering were so much fun with you and I admire this attitude. I will miss you guys, and your companion throughout my life and I am looking forward to have a reunion in Bonaire.

**Deep**, thanks for your help in finding an accommodation when I joint the department and also for your help to establish the IVUS beamformer script. I got to know you during the breaks and hanging out outside. I won't forget the summer school in Copenhagen which you helped me with my MATLAB knowledge and ultrasound beamforming. Our trip from Helsingør to Helsingborg was so fun, when we realized the problem, we didn't even discuss, we knew what we wanted and just took the ferry back again to solve the problem. I also admire your attitude in the conferences, I had so much fun with you specially in Taiwan. I can write almost a book about our adventure and I am looking forward to meet you again.

**Min**, thanks for taking care of restaurant arrangement in Taiwan, **Mirjem**, **Nuria**, thanks for helping me with Dutch forms and for the good vibes in the office. **Antonio**, you are such a nice person and I really appreciate when you gave water to my plant during the first lock down. You saved it and I am sure you will keep it sound and fresh. **Shegnan**, **Aaron**, **Antonio**, **Luci**, and **Geraldi**, the coffee mafia, I enjoyed our early morning talks while we were waiting for the coffee to be ready. **Verya**, thanks for your help in my first year and also for supporting the kerfless PVDF array. A special thanks to **Pieter** for his support with fast beamforming scripts. **Mohammad (Mo)**, I will not forget our trip in Rotterdam and Amsterdam and your discussion with Deep in Copenhagen! **Alex**, thanks for giving positive energy. **Jason**, I have enjoyed our talks in conferences, **Jorinde** and **Gonzalo**, I wish you success in finishing your Ph.D., **Sander, Fox, Sowmia, Vivek**, and **Jonas**, Welcome to the group!

During my stay in BME, I had a chance to join Bubble's group. **Klazina**, thanks for helping me with the vPA manuscript, accepting me to your group, your time in calling me late afternoon during the first lock down and checking my mood, and giving suggestions for the dinners. I learnt a lot being in your group and you taught me couple of lessons which I will apply in my career. **Bram**, thanks for your effort with the chicken embryo which sometimes you had to stay late to help me out and also with the sweets you brought to office. **Joop** and **Hongchen**, thanks in assisting me with the Brandaris recordings. We did the experiment together and stayed couple of times till midnight and I hope the outcome will be published soon. **Ines**, thanks for your support for the Brandaris and also your good vibes in the office. **Kirby**, thanks for listening to me and relieving me from the stress during my formidable and daunting Ph.D. duties. I wish you good luck in your career. **Mariel**, thanks for your support during our experiments and also for your time in listening to me when I complained. I wish you all the best. **Gert-Jan, Jiyeon, Mark**, thank you for being a nice office-mates. You added joy and light to the office. Good luck at your next career! **Simone**, I got to know you during the breaks where we shared our concerns in finishing up the Ph.D. journey. You are such a good listener and you demonstrated it when I complained on different issues. It was nice to have your point of view on different subjects which showed how critical thinker you are. During the first lock down when I stuck at home alone, you helped me a lot by calling and making virtual breaks. Thanks for being there for me and I wish you success with finishing your Ph.D. and your next career.

I also would like to thanks my past and current colleagues from Biomechanics group, **Ali,**

**Su, Merih, Kim, Astrid, Ayla, Annette, Eric, Imane, Eline, Rachel, Rouyu**, thank you all for the fun times at events! **Rouyu**, special thanks for finding me the accommodation to stay during my first 6 months and also arranging games and dinners. Later on, when you were moving, you arranged your fantastic studio for me which has lots of windows an amazing view. I loved the place so much that I stayed there till now. **Ali**, thank you for listening to me and giving your advice and support. I was really blessed when you shared your opinion about my personality during the stress reduction workshop. Eric, you are such a nice guy and thanks for listening to my stories. I really enjoyed the table tennis sessions!

**Mehdi** and **Zahra**, thanks for arranging the BBQs and dinners. I wish you best of luck in finishing your Ph.D. and also with your new career. **Reza Amin**, thanks for being patient and listening to my concerns during the breaks. Talking with you as a senior was relieving my stress. **Saikat Chatterjee**, You are a special guy. I really admire your keen eye and your Farsi speaking. I am looking forward to meet you again.

I would like to thanks my colleagues in TU Delft, **Nandini**, **Martin Verweij**,**Boudewine**, **Meysam**, **Alberico**, **Moein**, **Fabian**. It was fun to be with you at different occasions, conferences and to talk on different topics.

During my educational career in Tabriz, and Istanbul, I made lots of great friends. I would like to thanks **Masoud Amirkabiri**, you initiated all the fun in Sabanci university: arranged gathering, volleyball team, and trained us in the gym. I am lucky that our life path crossed and we made a really good moments, and memories which I will be proud of telling those stories when I get old. Of course, those nice, and precious moments wouldn't have been possible without **Mehdi Salehi**, **Fardin**, **Ali Tufani**, **Ali Asgharpour**, **Omid Farhanieh**, **Rupak**, **Nader Mahmoudi**, **Negar Majidi**, **Mohammad Sobhani**, **Pegah Nomanfar**, and **Hamed Tadayyoni**, being around. I also want to thanks **Vahid Tavakol** for all the late-night talks, the movie sessions, and our trips. Vahid, our company was great.

A special thanks to **Serdar** and **Halil Adali** for your support during my stay in Istanbul. **Halil Amca**, you are such a nice person with a good heart. I can't imagine what would have happened if you hadn't stood by my side. You merely traveled from Antalya to Ankara to take care of the paperwork. You have opened the doors for me and allowed me to continue my academic career, and I am grateful for your efforts.

I am delighted to be among special people in Tabriz with whom we spent fantastic times and made a fantastic friendship which after a decade, we are in contact despite each one of us being in different continents. I would like to thanks **ASAD** group and its member. **Hooshang**, bro, you are such a nice person. I really appreciate your time and effort in taking care of my diploma validation, during the corona lock down, you went to the airport to pick up my documents, then legalized them and sent it back by a passenger in the airport. **Ayoob**, you are my bro! Thanks for your help in Tehran and Tabriz, I always admire your philosophy and your knowledge. **Garsha**, we had lots of fun, in Ankara, Istanbul and Antalya. I wish there would be a time for reunion. **Mohammad Khodaei**, and **Mohammad Kaveh**, **Tadeh Tarverdians, Alireza Pirooznia, Mehdi Khantan, Farid Atashbahar, Masoud Zargarsaleh, Yusuf Hesam (R.I.P), Sina**, and **Kazem**. **Hooshang**, **Kazem**, and **Alireza** your poems and notes were exceptional. I'm proud to be a part of such a group; we had our first decade reunion as planned, and I'm excited to see you again in person.

# Sponsoring


LUMIBIRD
MORE THAN LASERS


Funded by
Hartstichting


medical
delta
we add